APERTURE CORRELATION MICROSCOPY

LIONEL FAFCHAMPS

Department of Physics

Faculty of Natural Sciences

Imperial College London

December 2014

Thesis submitted in fulfilment of the requirements for the degree of Doctor of Philosophy of Imperial College London

'The copyright of this thesis rests with the author and is made available under a Creative Commons Attribution Non-Commericial No Derivitives licence. Researchers are free to copy, distribute or transmit the thesis on the condition that they attribute it, that they do not use it for commercial purposes and that they do not alter, transform or build upon it. For any reuse or redistribution, researchers must make clear to others the license terms of this work.' (Imperial College London PhD regulations 2012)

Lionel Fafchamps: *Aperture Correlation Microscopy*, , © December 2014

DECLARATION

All work contained within this document is my own, except where appropriately referenced.

London, December 2014

Lionel Fafchamps

For my family.

Never give up. Never surrender.

— Galaxy Quest

ABSTRACT

Microscopy as applied to the biological sciences has benefited tremendously in the last 50 years from the invention of optically sectioning microscopes. Many techniques for microscopy developed recently offer super-resolved imaging, but often at the cost of light efficiency, signal, acquisition speed or significant amounts of money. This thesis investigates further development of aperture correlation microscopy: a cheap, light-efficient, wide-field, optically sectioning, video-rate imaging technique until now incapable of super-resolution.

An aperture correlation microscope was constructed, using a geometry consisting of 2 separate cameras permitting a larger field size than previous spinning disk aperture correlation systems. This microscope, operating at 16Hz (limited by the cameras) was then tested by imaging different samples and found to match reasonably well to the theory, while producing very clear images of biological samples.

In order to power this aperture correlation microscope, an image registration algorithm must first register the frames from both cameras. We present a high-speed image registration algorithm suitable for fixed deformations, where a calibration pattern can first be imaged, by leveraging the graphics processing unit. In testing, this registration algorithm is capable of framerates of over 200Hz on modest hardware.

A reflection correlation microscope was also constructed and characterised, operating at an illumination wavelength of 405nm, representing an advance into the UV for this technique. Synchronisation of camera acquisition and disk rotation allow for fast acquisition from a single camera. Measurements of its axial resolution match closely to the theory for 4 different illumination pattern pitches. Z-Stacks of transistor and Photovoltaic cell samples were taken in order to demonstrate this system's viability for imaging semiconductor devices.

Finally, a novel type of aperture correlation microscope capable of super-resolution is designed and characterised, leveraging coherent illumination. It is demonstrated how tailoring the spatial frequencies present in the aperture mask can result in enhancement of high frequency information up to twice the diffraction limit. Transfer functions are measured, and found to match reasonably well with theory. Lateral resolution improvement of 1.5 times over conventional microscopy is seen here, paving the way for a new, highly efficient super-resolving microscope.

PUBLICATIONS

Some ideas and figures have appeared previously in the following publications (not peer-review):

L. J. Fafchamps, M. A. A. Neil, and R. Juskaitis. GPU-based Image Registration in Aperture Correlation Microscopy, and Reflection Mode Correlation Microscopy. *Proc. SPIE* 8589, 2013

Some ideas and figures have appeared previously at the following conferences:

L. J. Fafchamps, M. A. A. Neil. GPU-based Image Registration in Aperture Correlation Microscopy. *Scientific Meeting of Photonics4Life, 6/12/2011*

L. J. Fafchamps, M. A. A. Neil, and R. Juskaitis. GPU-based Image Registration in Aperture Correlation Microscopy, and Reflection Mode Correlation Microscopy. *Photonics West*, 2012

L. J. Fafchamps, M. A. A. Neil. and R. Juskaitis. Image processing for spinning-disk, widefield optical sectioning microscopy. *Photon12*, 2012

I want to thank you for taking time out of your day
to come and witness my hanging

— George W. Bush

ACKNOWLEDGMENTS

I would firstly like to thank my supervisor, Prof. Mark Neil, for his guidance and support over the years, and for giving me the opportunity to work in such an exciting field. My gratitude also goes to Dr. Rimas Juskaitis, whose supervision while I was at Aurox and throughout the project has been invaluable.

Thanks go out to all the support staff in the group: Martin and Simon in the workshop, Judith and Marcia for their administrative support.

I would also like to thank my colleagues in the Photonics group for their friendship and enlightening conversation.

Finally, I must acknowledge the financial contribution to the project from both the EPSRC and Aurox ltd, without whom this would not have been possible.

CONTENTS

1 INTRODUCTION AND THESIS OUTLINE 1

1.1 Introduction 1

1.2 Thesis Outline 4

2 OPTICAL SECTIONING MICROSCOPY 7

2.1 Introduction to Sectioning Microscopy Theory 7

2.1.1 Fluorescence Microscopy 7

2.1.2 Conventional Image Formation 9

2.1.3 Point Scanning Confocal Microscopy 13

2.2 Scanning Microscopy Techniques 16

2.2.1 Extensions to Confocal Microscopy 16

2.2.2 Multiphoton and Nonlinear Illumination 18

2.3 Wide-field Acquisition 22

2.3.1 Light Sheet Microscopy 22

2.3.2 Structured Illumination 24

2.3.3 Aperture Correlation/PAM Microscopy 26

2.3.4 Super-resolution with Structured Illumination 27

2.3.5 SIM with point-like illumination 29

2.4 Unlimited Super-resolution 32

2.4.1 Non-linear SIM 32

2.4.2 Stimulated Emission Depletion 34

2.4.3 Molecular Localisation 36

2.5 Conclusion 37

3 APERTURE CORRELATION MICROSCOPY 39

3.1 Introduction 39

3.2 Theory 41

3.2.1 Resolution 42

3.3 Experiment 46
3.3.1 Experimental Setup 46
3.3.2 Imaging Arms 49
3.3.3 Cameras and noise 51
3.3.4 Samples 52
3.3.5 Calibration and Image Registration 53
3.4 Results and Discussion 54
3.4.1 Microspheres 54
3.4.2 Thin Sheets 55
3.4.3 Samples 59
3.5 Conclusion 61
4 REAL TIME IMAGE REGISTRATION 63
4.1 Introduction 63
4.1.1 Background 64
4.1.2 Why we need registration 66
4.1.3 Requirements 66
4.2 OpenGL 68
4.3 Implementation 69
4.3.1 Calibration 71
4.3.2 Extension of Calibration Map 72
4.3.3 Drawing 73
4.3.4 Shaders 74
4.3.5 Framebuffers and 16bit operation 75
4.4 Results 76
4.5 Conclusion 77
5 REFLECTION CORRELATION MICROSCOPY 79
5.1 Introduction 79
5.2 Theory 80
5.2.1 Reflection vs Fluorescence 80
5.2.2 Axial Response 81

5.2.3 Lateral Resolution 82
5.3 Experiment 84
5.3.1 Imaging Setup 84
5.3.2 Acquisition synchronisation 88
5.4 Results and Discussion 89
5.5 Conclusion 96
6 SUPER-RESOLUTION APERTURE CORRELATION MICROSCOPY 99
6.1 Introduction 99
6.2 Theory 100
6.2.1 Mask Frequencies and Resolution 101
6.2.2 Frequency Limits in Incoherent and Coherent Imaging 102
6.2.3 Our novel approach 103
6.2.4 Line, Quad, and Hex masks 107
6.3 Mask Design 110
6.4 Modelling 112
6.4.1 Resolution 115
6.4.2 Signal 122
6.5 Experiment 124
6.5.1 Experimental Setup 124
6.5.2 New Spinning Disk 124
6.5.3 Illumination 127
6.5.4 Imaging 128
6.6 Results and Discussion 129
6.7 Future Work 133
6.8 Conclusion 134
7 CONCLUSIONS AND FUTURE WORK 135
i APPENDIX 141
A OPTICAL TRANSFER FUNCTION MODELLING 143
B COPYRIGHT PERMISSIONS 147
B.0.1 Email sent to Zeiss 147

B.0.2 Email received from PNAS 148
B.0.3 Elsevier RightsLink Confirmation 148

BIBLIOGRAPHY 151

LIST OF FIGURES

Figure 1 Jablonski diagram of fluorescence absorption and emission. 8

Figure 2 Conventional OTF with defocus. 11

Figure 3 3D Conventional OTF. 12

Figure 4 A diagram of a point scanning confocal microscope. 14

Figure 5 Comparison of the detected intensity as a fluorescent thin sheet is scanned through focus in a point scanning confocal microscope and conventional microscope. 15

Figure 6 3D Confocal OTF. 15

Figure 7 Jablonski diagram of two-photon excitation and subsequent emission in a fluorophore. 18

Figure 8 Jablonski diagram of second harmonic generation in a molecule. 2 incoming photons excite the molecule into a virtual state, which instantly relaxes while emitting SHG. 20

Figure 9 Jablonski diagram of CARS generation in a molecule. 21

Figure 10 A diagram of the SPIM setup. The light sheet is created by a cylindrical lens (CL) before entering a microscope objective (PO) which focuses the light into the sample (S) . Detection is performed by another objective (DO), fluorescence is filtered (F) and imaged onto the camera (CAM) by the tube lens (TL).[2] 22

Figure 11 Schematic diagram of the aperture correlation microscope. The aperture mask is imaged onto the sample and return fluorescence passes back through the mask, where it's split from illumination by a dichroic and imaged to a camera. 26

Figure 12 Axial maximum intensity projections of the microtubule cytoskeleton in HeLa cells, with a widefield image on the left and 3D SIM image on the right. A stereo projection of the data is underneath. Image reproduced with permission from Elsevier. [3] 29

Figure 13 Images acquired from the Zeiss Airyscan microscope.[4] 30

Figure 14 Mammalian CHO cell imaged with non-linear SIM. Subset of the data enlarged on the right is (B) TIRF microscopy (C) SIM-TIRF (D) Nonlinear SIM-TIRF. [5] 32

Figure 15 An image of cell nuclei comparing STED microscopy to confocal.[6] 34

Figure 16 A simple layout of an aperture correlation system collecting conjugate and non-conjugate information, where the locations of the different planes are indicated. 42

Figure 17 Plots of the response to a thin fluorescent sheet through focus, as a function of defocus, for disk pitch sizes of 160 and 80 microns. The normalised intensity is relative to the illumination intensity, so that 0.5 in the maximum response value. 46

Figure 18 A scaled up version of the line pattern and configuration etched onto the spinning disk. 47

Figure 19 A schematic diagram of the imaging setup. The LED is collimated by a condensor, and then filtered at for 532nm (F2). The beamsplitter BS reflects the illumination through the disk and into the microscope objective O through the tube lens TL. Return fluorescence is imaged to CCD1 and CCD2 through a beamsplitter and long pass filter (600nm). 47

Figure 20 Optical layout of the imaging system from the disk to the camera. 49

Figure 21 Figures illustrating the performance of the prototype optics designed for our aperture correlation setup. 50

Figure 22 Image of a field of beads, post subtraction. (40x 0.75) 56

Figure 23 Transfer function of the system, with an overlay in white representing areas of low intensity in the Fourier transform of a sphere. 56

Figure 24 A sectioned image of the spin coated thin film, taken with the 40x 0.75NA objective. The dark portion of the image represents the 80µm sector of the disk, while the bright portion represents the 160µm sector. 57

Figure 25 Plots of axial responses accross both 160µm (a) and 80µm (b) disk pitches. 57

Figure 26 An x-z plot of the thin film data, where the tilt in the image stack is clearly visible. 58

Figure 27 Images of lilly anther pollen, widefield and sectioned, 60x 1.2NA 60

Figure 28 Images of lilly anther pollen, widefield and sectioned, 100x 1.35NA 60

Figure 29 Maximum intensity projections of lilly anther pollen image stacks. 61

Figure 30 3D render of a pollen grain. Tick marks are in μm. 61

Figure 31 Zoomed region of image after affine transform registration. The orange halo in the left picture arises from subpixel misalignment. 67
Figure 32 An illustration of the OpenGL shader pipeline. 70
Figure 33 A triangle deformed through an affine transform by shifting the vertices. 70
Figure 34 The calibration pattern projected onto the disk. 71
Figure 35 The full extended triangle map, covering the entire field of one camera. 73
Figure 36 Unregistered and registered calibration patterns overlaid in red/green. 76
Figure 37 Plots of intensity vs defocus for different disk pitches. 82
Figure 38 Diagram of incident light onto a step in a high NA reflection microscope. 83
Figure 39 A schematic diagram of the reflection correlation microscope. The 405nm LED is collimated by a condenser assembly before being filtered by F and polarised through a beamsplitter BS2. It is then reflected through the disk by beamsplitter BS and enters the Objective O through the quarter waveplate QWP. Reflected light from the sample is rotated in polarisation by the double pass through QWP before passing through the disk and being imaged to the CMOS camera. 84
Figure 40 Optical layout of the illumination system. LED illumination is collimated by the collector assembly CA. The illumination stop S allows control of the illumination spot size at the sample plane. 86
Figure 41 Optical layout of the Imaging system. 86
Figure 42 Strehl ratio of the imaging system, diffraction limited for the 3 design wavelengths of 390, 405 and 420. 87

Figure 43 A diagram of the setup used to synchronise camera acquisition to disk rotation. 88

Figure 44 Images acquired during the mirror test, for 2 different grid pitches. Left to right corresponds to $+z$. Black spots are from dust on the sample. 63x 1.4NA. 91

Figure 45 Maximum intensity projection of the fractal black anti-reflection coating taken on the 80µm disk sector. 50x 0.95NA 92

Figure 46 Sample images from a stack taken of a PV cell with the 80µm disk sector. 50x 0.95NA 94

Figure 47 Sample images from a stack taken of a transistor chip with the 80µm disk sector. 50x 0.95NA 95

Figure 48 Z projection of a region on the transistor sample, illustrating the ability to depth resolve coatings. 96

Figure 49 PV cell (a) and transistor chip (b) 3D reconstructions. 96

Figure 50 Frequency components in a line mask, with A, B and C being the zeroth, first and a second orders respectively. 103

Figure 51 Frequency components in the illumination plane, after squaring from amplitude to intensity. The red and blue dots represent frequencies present at $k_z \neq 0$. 105

Figure 52 Frequency components in a quad mask, with A, B and C being the zeroth, first and a second orders respectively. D arises from cross-terms between B orders. 107

Figure 53 Frequency components in a hex mask, with A, B and C being the zeroth, first and a second orders respectively. D arises from cross-terms between B orders. 108

Figure 54 A flow chart of the hologram optimisation process. 111

Figure 55 Transfer functions in u, v and k_z, v for conventional, confocal, and airy pinhole confocal arrangements. 114
Figure 56 The 2D OTF in focus for the line mask, for different values of ζ. 117
Figure 57 The 2D OTF in focus for the quad mask, for different values of ζ 118
Figure 58 The 2D OTF in focus for the hex mask, for different values of ζ 119
Figure 59 The 3D OTF in focus for the line mask, for different values of ζ 120
Figure 60 The 3D OTF in focus for the quad mask, for different values of ζ 121
Figure 61 The 3D OTF in focus for the hex mask, for different values of ζ 122
Figure 62 A plot of the detected signal (relative intensity in focus over out of focus) versus the zero order suppression term ζ. 123
Figure 63 Experimental setup of the super-resolving aperture correlation microscope. 125
Figure 64 Images of the new spinning disk prototype taken with a 20x objective. 126
Figure 65 A layout of the 6f optical relay from the disk to the microscope objective, showing the location of the pupil mask (PM). 128
Figure 66 Plots of the 6f optical relay's MTF and Strehl ratio. 128
Figure 67 Optical transfer functions of the microscope with the line mask, with (a) and without (b) masking the zeroth order in the pupil. The region of support is shown in white. 132

Figure 68 Optical transfer function of the microscope with the hex mask, with (a) and without (b) masking the zeroth order in the pupil. The region of support is shown in white. 132

Figure 69 Field of beads, conventional (a) and super-resolved (b), using the line mask with $\zeta = 1$. 133

Figure 70 The OTF plotted using both the Stokseth approximation and the exact OTF. 145

LIST OF TABLES

Table 1 AVT Stingray F145B Specifications, as compared to the Hamamatsu Orca. 51

Table 2 Sampling rates for the 3 objectives used. 87

Table 3 Axial resolution as measured by the mirror test compared with simulation. 91

1

INTRODUCTION AND THESIS OUTLINE

1.1 INTRODUCTION

In wide field microscopy, an acquired image consists of light from the focal plane of the microscope objective, but also receives contributions from out-of-focus background elements in the sample. This greatly affects the contrast available from this type of microscope, especially when using high numerical aperture objectives with very narrow depths of field, where details can be almost entirely obscured by background.

To combat this effect, several microscopy techniques have been designed over the years that are capable of optical sectioning - removing the background information and leaving only the in-focus image. These techniques have greatly increased the contrast and resolution available and have proved to be of great use in the biological sciences, where imaging of life processes has been made possible at the sub-cellular level ($\sim 100nm$). Optical sectioning also makes it possible to combine these image slices and reconstruct objects in three dimensions[7].

The first technique capable of optical sectioning was invented by Zsigmondy and Siedentopf in 1902 for the purpose of observing scattering from particles dispersed in a medium, by making use of cylindrical optics to create a light sheet for illumination (termed Ultramicroscopy)[8]. This approach was capable of measuring the size of $4nm$ nanoparticles embedded in glass, but is not capable of imaging as only scattered light is observed from the sample.

Point scanning confocal microscopy, the first imaging sectioning technique to appear, was invented and patented some 60 years ago by Marvin Minsky,

at Harvard University[9]. It consisted of illuminating an object with a focused spot of light, and picking up the return light through a detection pinhole[10], while scanning the sample over the spot to construct an image. The development of laser sources in the 1960s led to the invention of the first confocal laser scanning microscopes by Davidovits and Egger[11, 12]. Limited by slow scanning speeds and low power laser sources, as well as a lack of computational power needed to process the large amounts of data generated, it is only more recently that advances in these areas have made commercialisation of confocal microscopy possible - in the biological sciences but also in semi-conductor physics and other fields where high resolution and optically sectioned images are useful.

Different implementations of confocal microscopy have tried to address the inherently slow scan speeds of confocal point scanning microscopes in different ways: the Nipkow disk method, invented around the same time as the first confocal laser scanning microscopes, uses a disk with many pinholes, allowing points to be scanned in parallel[13]. In line scanning confocal microscopy, invented soon afterwards, the pinhole is extended in one dimension to a line, and the point illumination is replaced by line-shaped illumination, usually obtained by focussing the illumination with a cylindrical lens; this greatly increases scan speeds by removing the need to scan in two dimensions, at the cost of lower resolution in the line direction[14, 15]. These two approaches were among the first to provide real-time imaging, whereby optically sectioned images can be viewed by eye or by camera at a rate limited essentially by the illumination power available.

Other techniques such as selective plane illumination achieve sectioning by focusing light into a sheet at the object plane (as in ultramicroscopy) - allowing sectioned images to be retrieved straight from the microscope objective[16]. Multi-photon approaches such as two-photon microscopy use non linear response to combine two photons of double the wavelength necessary to excite fluorescence in the sample at the focal point of the objective[17].

While scanning confocal approaches like point scanning or Nipkow disk microscopy acquire a confocal image directly onto a camera (or by eye in the case of the Nipkow disk), relaxing this requirement and allowing for computational post-processing gives rise to a class of methods known as structured illumination. In these systems, a grid pattern is introduced into the illumination beam and the modulated pattern is projected onto the sample. This pattern is shifted several times, and the resulting images can be combined computationally to produce a sectioned image[18]. In some systems, the grid pattern and illumination beam are replaced by a LED stripe array with individually addressable units, simplifying the setup and removing the need for moving parts.[19]

A related technique, aperture correlation, uses a double sided spinning disk with an etched pattern on it to produce the structured illumination[20, 21]. Light returning from the microscope passes through the disk on its way to the camera, with the effect that light passing through the disk contains both widefield out-of-focus information as well as a modulated confocal signal. Early versions of this microscope collect light both through this etched sector and then subsequently from a blank, open sector in order to acquire a widefield image. Subtracting these two images from each-other yields a confocal image. By collecting the light reflected from the disk, it is also possible to collect the same widefield out-of-focus information - minus the modulated confocal signal (which misses the reflective parts of the disk). Structured illumination techniques benefit from a faster imaging speed than point scanning confocal microscopy. Additionally, while many scanning confocal techniques rely on the use of lasers in order to achieve high enough illumination intensities and hence signal, structured illumination and particularly aperture correlation microscopes can function well using incoherent sources such as lamps or light emitting diodes, due to their inherent light efficiency.

This thesis investigates a new, coherently illuminated aperture correlation microscope which is theoretically capable of super resolution exceeding the

capabilities of confocal microscopy, while remaining light efficient and capable of real-time imaging. Along the way, we introduce experimental systems and supporting computer software which make this final experiment possible.

1.2 THESIS OUTLINE

Chapter 2 introduces the theory of image formation in a conventional microscope, in particular its poor depth descrimination (particularly in samples with uniform areas), before examining the impact of a host of alternative techniques (such as confocal microscopy). Their operating theory and experimental diagrams are introduced, and systems are compared to each-other to determine what makes a good microscope for any particular application.

Chapter 3 introduces the 2-camera aperture correlation microscope constructed at Imperial College. The operating theory of this microscope is described, as well as the experimental setup along with a brief overview of image registration and its necessity in this type of microscope. Experimental results supporting the system's optical sectioning capability are also introduced.

The real-time image registration algorithm which was designed to run on a microscope such as that in Chapter 3 is described in Chapter 4. It is explained how dedicated graphics processing hardware in a modern computer is capable of fast image manipulation, and how this has made possible our algorithm. Finally, the accuracy and speed of the algorithm is presented as it applies to the system in Chapter 3.

In Chapter 5, we describe an Aperture Correlation Microscope constructed at Aurox ltd, the CASE sponsor of this research project. Applying the same principles as previously, this microscope functions on reflective samples, useful in fields such as semiconductor fabrication and assay. UV illumination is used to maximise the resolution of the system, while synchronising the

camera acquisition to the disk rotation results in fast imaging. Differences between the operating theory of this microscope and the fluorescence version are highlighted, and experimental measurements of its resolution are presented.

Finally, chapter 6 introduces the new super resolving Aperture Correlation Microscope invented and constructed as part of this project. The theory of operation of this microscope, functioning with coherent illumination, is introduced. A discussion of how super resolution can be achieved in this setup by tailoring the spatial frequencies in the aperture mask is also presented, before showing some preliminary results from the system.

2

OPTICAL SECTIONING MICROSCOPY

2.1 INTRODUCTION TO SECTIONING MICROSCOPY THEORY

2.1.1 *Fluorescence Microscopy*

Fluorescence is a process whereby a molecule absorbs a photon at a particular wavelength, becoming excited into an energetic state, then spontaneously re-emitting another photon as it relaxes back to its ground state. A Jablonski diagram (figure 1) is a way of visualising the electronic transitions in a molecule, where the two energy levels $S_1$and S_0 are illustrated by thick black lines. Each of these is split through degeneracy into several different vibrational modes which are populated depending on the thermal energy of the system.

Assuming the system starts from the lowest energy state of S_0, an incident photon excites the system into one of the vibrational levels of S_1. The system then rapidly decays into the bottom vibration energy state of S_1 through phonon emission, on a timescale of $10^{-12}s$ [22]. Then, over a timescale of typically $10^{-9}s$, the system undergoes spontaneous emission, emitting a photon with a slightly longer wavelength than the incident one. The shift in wavelength between excitation and fluorescence is known as the Stokes' shift [23].

Although in general molecules can be created which efficiently absorb and emit light at visible frequencies useful in optical microscopy, there are 2 main mechanisms which may serve to reduce fluorescence from a sample. The first of these is that many fluorophores have an additional state, known as a triplet

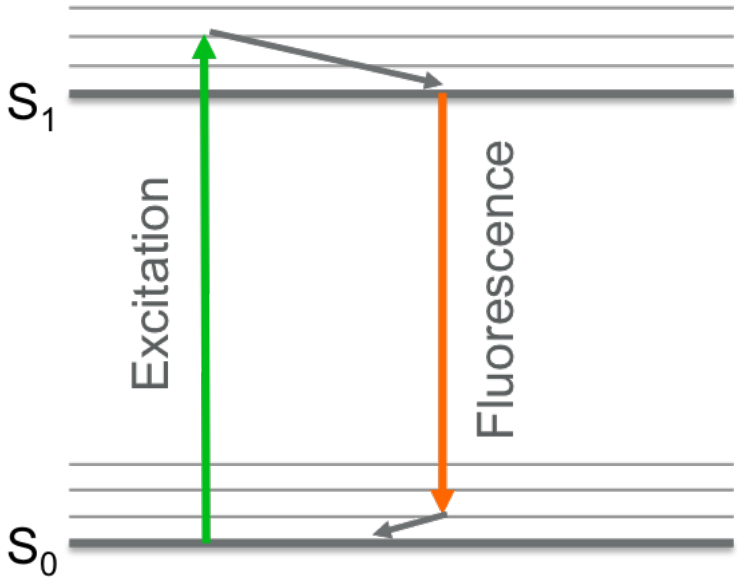


Figure 1: Jablonski diagram of fluorescence absorption and emission.

state, from which S_1 can decay into vibrationally. Although the probability of this decay occuring is often quite small ($< 1\%$), the lifetime of this state can be quite a lot longer than that of the S_1 state (up to 10 seconds), meaning that under high excitation powers one can get most of the fluorophores into this 'dark' state. The triplet state lifetime is so much longer than the S_1 state because the molecule needs to undergo spin conversion to produce unpaired electrons - this process is relatively rare.

Another effect which serves to reduce fluorescence signal is photobleaching. There are a great deal of different mechanisms by which photobleaching can occur, but in essence this encapsulates a photochemical reaction which destroys fluorophores in a sample, particularly under high illumination powers [24].

Fluorescence can be useful in biological microscopy where a sample can be stained with a fluorescent dye or marker, and illuminated at the excitation wavelength of the fluorophore. Light emitted by the sample can then be separated from illumination by a dichroic beamsplitter and imaged through an optical filter in order to isolate the emission wavelengths. The staining process can be tailored so that different regions in a sample are stained with

different colour dyes, leading to striking multicolour images and the ability to locate specific molecules or regions.

Measuring other characteristics of fluorescence such as lifetime or anisotropy can yield more information about the sample or the molecular environment of the fluorophore. Some examples of this include measuring the polarisation of fluorescence after exciting the molecule with polarised light, which can yield information about the orientation of the fluorescent protein [25, 26]. A change in the lifetime can also indicate changes in the surrounding local refractive index [27] or other changes that affect the vibrational energy levels of the fluorophore. Fluorescence lifetime imaging (FLIM) has also been used to probe the surrounding viscosity [28] as well as pH of the fluorophore [29, 30]. Combining polarisation and lifetime measurements has been used to measure the viscosity in the environment of a fluorophore [31]. FLIM's ability to sense changes in the environment of a fluorophore has a great deal of applications in biology: one example of these is the study of cell metabolism through changes in the lifetime of nicotinamide adenine dinucleotide (NADH) [32]. It is also currently being tested for use in aiding diagnostics and treatment of basal cell carcinomas (skin cancer) [33].

2.1.2 *Conventional Image Formation*

Before beginning a discussion of confocal imaging techniques, it is best to understand image formation in a conventional microscope - specifically why it cannot resolve well axially. Throughout this section normalised optical units (O.U.) (a, b, c) will be used, related to the (x, y, z) coordinates by:

$$(a, b) = \frac{2\pi n}{\lambda} \sin(\alpha)\,(x, y) \tag{1}$$

$$c = \frac{8\pi n}{\lambda} \sin^2(\alpha/2)\, z \tag{2}$$

where λ denotes the wavelength and $n \sin \alpha$ is the numerical aperture. When working in cylindrically symmetrical coordinates, we may also wish to use normalised radial coordinates:

$$r = \frac{2\pi n}{\lambda} \sqrt{x^2 + y^2} \sin(\alpha) \tag{3}$$

In order to show how conventional microscopy cannot resolve well axially, we can observe how the system responds to defocus. In order to do this, we can look at the Optical Transfer Function (OTF) $T(s, c)$ of the system, which tells us how different spatial frequency components s of the object are attenuated through the setup at different axial depths c, and is given by the Fourier transform of the intensity point spread function. In this case s corresponds to the normalised spatial frequency, given by:

$$u = \frac{\lambda}{n \sin(\alpha)} f_x \tag{4}$$

$$v = \frac{\lambda}{n \sin(\alpha)} f_y \tag{5}$$

$$s = \sqrt{u^2 + v^2} \tag{6}$$

and the point spread function in this type of microscope is given by $|e(r, c)|^2$, with $e(r, c)$ the amplitude point spread function. The full form of the OTF was first determined in 1955 by Hopkins, who determined the frequency response of a defocused optical system as a sum of Bessel functions [34]. Assuming that the OTF has cylindrical symmetry, we can use the much simpler Stokseth's approximation (for aberration-free optics in a low NA system) which gives us [35]:

$$T(s, c) = \begin{cases} g(|s|) \frac{2J_1\left[cs\left(1 - \frac{|s|}{2}\right)\right]}{cs\left(1 - \frac{|s|}{2}\right)} & if\ 0 < |s| < 2 \\ 0 & otherwise \end{cases} \tag{7}$$

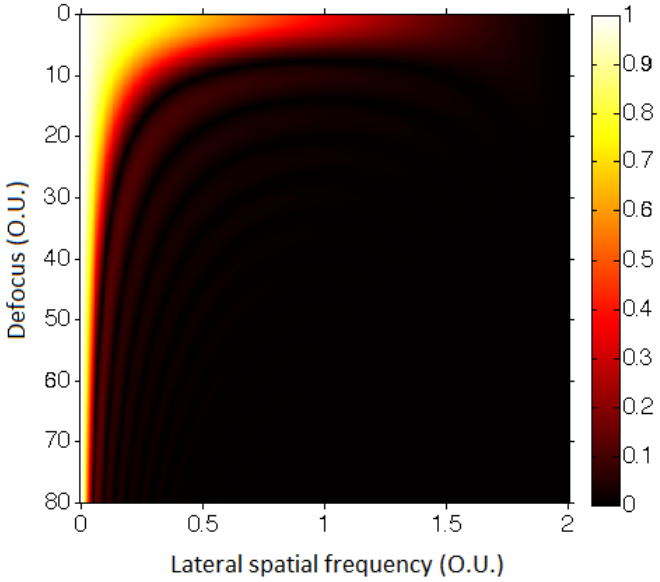


Figure 2: Conventional OTF with defocus.

$$g(s) = 1 - 0.69s + 0.0076s^2 + 0.043s^3 \tag{8}$$

where J_1 is the Bessel function of the first kind. An important result here is that the OTF is only nonzero for values of lateral spatial frequency $s < 2$, imposing a limit on the frequencies that can be imaged. A plot of the OTF (figure 2) shows that as the spatial frequency tends to 0, the OTF takes a constant value at any depth - suggesting that this microscope cannot discriminate depth in samples with 0 spatial frequency. Relating this back to what is detected, using a CCD camera for instance, we look at the detected intensity I. The intensity at the detector takes the form of an intensity generation function $f(a,b,c)$ (ie. the intensity in the object plane at the point (a,b,c) generated through fluorescence) convolved with the PSF:

$$I(a,b,c) = f(a,b,c) \otimes |e(r,c)|^2 \tag{9}$$

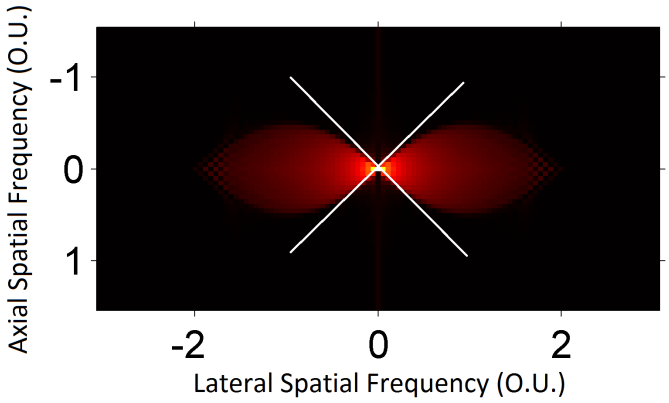


Figure 3: 3D Conventional OTF.

For a fluorescent thin sheet, we can set $f(a,b,c) = \delta(c)$ with $\delta(c)$ the Dirac delta function. Integrating the intensity in the plane of the detector gives an expression for the total detected intensity, so:

$$I_{tot}(c) = \int_0^\infty \delta(c) \otimes |e(r,c)|^2 \, r dr \tag{10}$$

This can also be re-written as:

$$I_{tot}(c) = T(0,c) \tag{11}$$

which, as previously mentioned, is constant with defocus. This shows that a conventional microscope cannot discriminate depth in a sample with 0 spatial frequency, such as a mirror or fluorescent thin sheet.

It is also possible to show this by not only Fourier transforming the lateral coordinates, but also the defocus c. This was approximated by Gu and Sheppard [36], who Fourier transformed the Stokseth approximation (equation 7) with respect to c. Figure 3 shows this function plotted in a plane parallel to the optical axis. The missing cone of frequencies around the origin suggests that these axial spatial frequencies cannot be resolved, and the maximum extent of the function as s tends to 2 shows that very high lateral spatial frequencies are also difficult to resolve in a conventional microscope. Most samples that

we might be interested in observing contain frequency information residing in this missing cone, which canot be resolved and reduces the overall contrast available from the microscope (particularly in thick samples).

Many of the techniques we cover from this point onwards have the ability to resolve information beyond what is capable in a conventional microscope: these are known as super-resolving microscopes, particularly when resolving laterally past $s = 3$. When we say that a microscopy technique's resolution surpasses conventional microscopy by a factor of n, what is meant is that the maximum detectable extent of that system's transfer function is n times higher than in conventional microscopy.

2.1.3 *Point Scanning Confocal Microscopy*

Point scanning confocal microscopy is based on illuminating the sample with a point and imaging the sample through a detection pinhole (figure 4). The detection pinhole is able to block out-of-focus light as only light generated in the focal plane and on axis will pass through it - light generated in the focal plane but off-axis is imaged to the side of the pinhole and blocked, and light generated on-axis but outside the focal plane is defocused at the aperture and thus only a fraction gets through.

In this setup, the intensity PSF is given by the product of the illumination and detection PSFs - assuming these are identical that gives $|e(r,c)|^4$ [7]. We can make this assumption because, in a fluorescence system, light is re-emitted from the sample incoherently and indepentently of the illumination. Although the wavelengths of the illumination and fluorescence light are slightly different, in practice the difference between the PSFs is typically negligible, particularly when dealing with fluorophores with a small Stokes' shift. This means that the OTF now takes the form of the convolution of the conventional microscope OTF with itself (because the PSF is the square of the

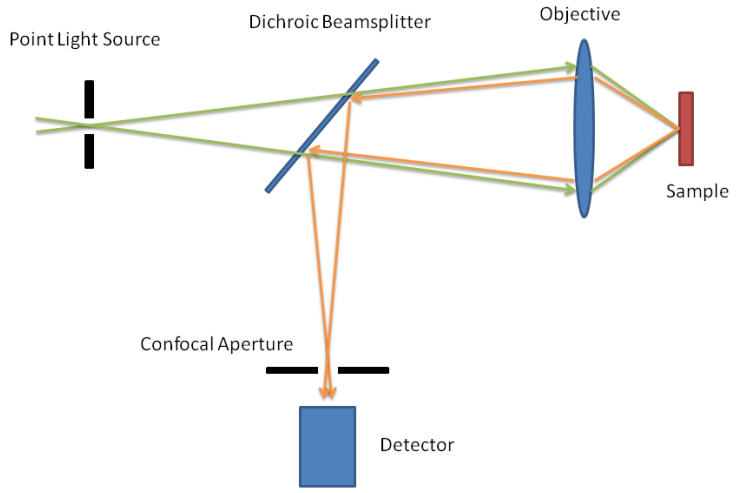


Figure 4: A diagram of a point scanning confocal microscope.

conventional case). If we take the case of a thin fluorescent sheet again, as in section 2.1.2, then [37]:

$$I_{tot}(c) = \int_0^\infty \delta(c) \otimes |e(r,c)|^4 \, r dr \tag{12}$$

$$I_{tot}(c) = \int_0^\infty T^2(s,c) \, s ds \tag{13}$$

Unlike the conventional case, in confocal microscopy the detected intensity is not constant with defocus. A plot of intensity versus defocus can be found in figure 5, which shows that integrated intensity drops as the sheet goes out of focus, indicating this microscope's ability to discriminate depth in these uniform samples.

As with the conventional case, another way of looking at this is to plot the 3D OTF for the point scanning confocal microscope. From figure 6, we can see that the cone of frequencies that was missing in the conventional 3D OTF is now filled, again suggesting optical sectioning. Additionally, the OTF also stretches further in lateral spatial frequency, from $s = 2$ in the conventional case to $s = 4$, suggesting an improvement in lateral resolution by a factor of 2 as well. In practice, the signal past $s = 3$ is quite small and one would expect

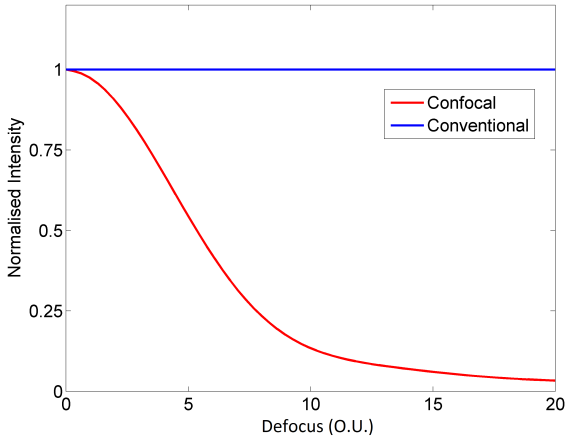


Figure 5: Comparison of the detected intensity as a fluorescent thin sheet is scanned through focus in a point scanning confocal microscope and conventional microscope.

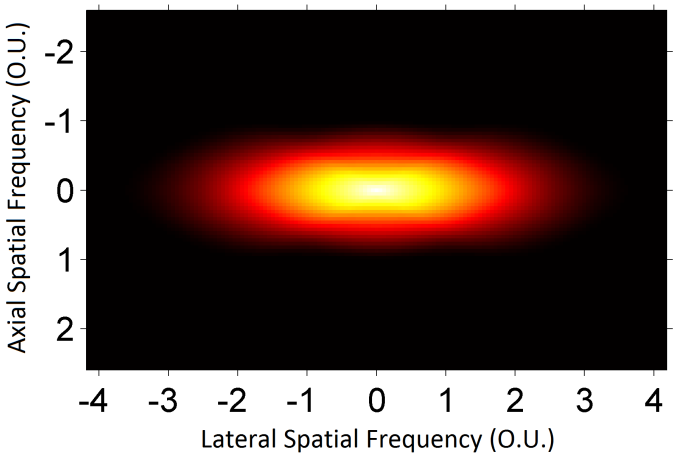


Figure 6: 3D Confocal OTF.

an improvement of $\sqrt{2}$ in lateral resolution over conventional microscopy [37].

Confocal microscopy does have significant drawbacks due to having to scan point by point - images can take a long time to create. This makes imaging live or moving samples impractical, and video-rate imaging (30Hz) is not generally possible over the whole field of the objective. Additionally, the lasers usually used in confocal setups are often bulky and expensive; the high illumination powers present also make fluorophore saturation and photo-bleaching a problem.

2.2 SCANNING MICROSCOPY TECHNIQUES

2.2.1 *Extensions to Confocal Microscopy*

2.2.1.1 *Line Scanning Confocal*

In an attempt to address some of the issues with point-scanning confocal microscopes (slow scan speeds, low signal, low light efficiency) line or slit scanning confocal microscopy was invented [38]. In this configuration, the pinhole detector is replaced with a slit, while the illumination is now provided by focusing illumination (usually a laser) onto the sample with a cyclindrical lens. Rather than having to scan along two dimensions, now only the dimension perpendicular to the slit needs to be scanned, dramatically improving acquisition speeds at the cost of sectioning ability and resolution.

Assuming detection horizontal to the direction of the slit, the resolution of the microscope is comparable to that of a point scanning confocal microscope, with an increased lateral extent of the transfer function by a factor of $\sqrt{2}$. Along the direction of the slit, however, the microscope's performance is reduced to that of a conventional system, with no lateral resolution enhancement [39, 40]. This has ramifications on the overall axial resolution of the microscope, where the intensity response to scanning a thin sheet through focus is approximately 1.6 times wider that of a point scanning setup. However, this system has a significant advantage due to the increase in signal available to the detectors: because fluorophore saturation poses a limit to signal strength in fluorescent applications, line-scanning systems can perform up to an order of magnitude better than point-scanning microscopes with regards to detected signal [41]. This increase in signal has made possible high speed (over 100Hz) imaging with confocal devices, particularly when using high speed laser scanning apparatus [42]. Attempts have also been made to compensate for the reduced sectioning capability in this microscope by detecting outside the region of the slit and using this data to subtract background, which can

improve the sectioning capability (response to scanning a thin sheet through focus) by a factor of 2.2 over conventional slit scanning microscopes [43].

2.2.1.2 *Multiple Point Scanning*

Multiple point scanning confocal microscopy is an approach which attempts to correct for the slow scan speeds in a single point setup by scanning many points in parallel. This was first achieved in 1968 by Petran [13], using a Nipkow disk - a spinning disk with multiple pinholes in it, generally arranged in an Archimedean spiral pattern. These pinholes are placed at the primary image plane so they are imaged onto the sample and also act as detection pinholes for return fluorescence.

The increased imaging speed using Nipkow disks allows real-time (video-rate) imaging of moving samples (through the use of CCD's), allowing the study of biological processes on a relatively fast time scale. Certain Nipkow disk systems also allow the user to see the image directly by eye, where an image can also be built up as the disk spins. Additionally, this technique reduces the light intensity in the sample plane, reducing fluorophore saturation and photo-bleaching rates.

Because of the illumination setup, this technique is not very light efficient - often only around 0.5-1% of available illumination power gets through the disk and to the sample [21]. This can be addressed to some extent by adding a microlens array before the Nipkow disk to focus light through the pinholes, increasing light efficiency up to 70%. Several commercial microscopes like the Yokogawa CSU100 rely on this technique [44].

Perhaps the most important limitation of this technique is due to pinhole cross-talk. Defocused light from one pinhole can enter into adjacent pinholes, reducing the sectioning power of the microscope; as such, the pinhole configuration and spacing must be carefully planned to avoid this effect [45, 46].

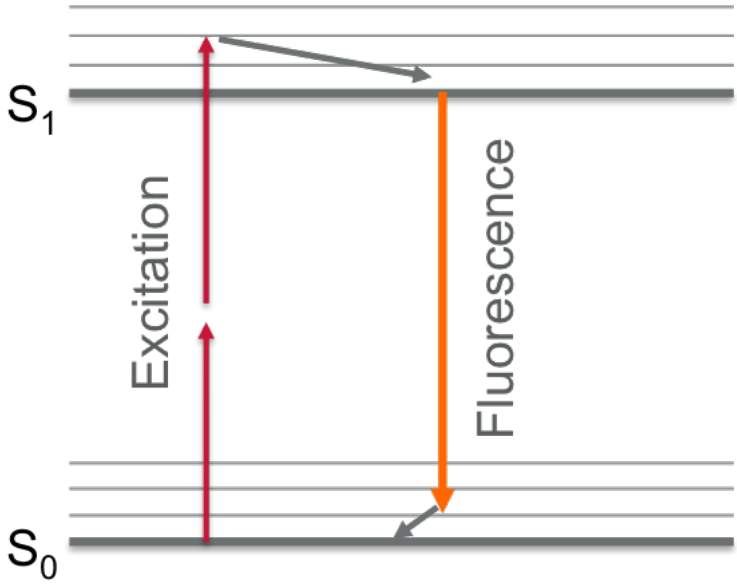


Figure 7: Jablonski diagram of two-photon excitation and subsequent emission in a fluorophore.

2.2.2 *Multiphoton and Nonlinear Illumination*

Confocal microscopy was the first technique to provide true 3D resolution with optical sectioning, and since its invention it has been established as the gold standard by which most other microscopy techniques are judged. One of the first alternative techniques to be invented was two-photon microscopy, by Denk and Webb in 1989 [47]. Although similar to confocal microscopy in that it is implemented in fluorescent microscopy systems by scanning a laser spot accross the sample, the illumination relies on nonlinear optical effects to excite fluorescence.

Nonlinear excitation relies on a high illumination intensity at the focal spot ($\sim 250\text{GW/cm}^2$), with photons of half the energy required to normally excite fluorescence in a sample. At these high power levels, the point at focus can experience a nonlinear effect allowing a fluorophore to absorb two photons of half the energy required and exciting to its upper state S_1, then spontaneously fluorescing afterwards to its ground state S_0. A Jablonski diagram of this interaction is in figure 7.

One consequence of this is that fluorescence in multiphoton microscopy is only generated at the focal point of the illumination beam, meaning that the size of the 3D probe (ie. the volume in the sample from which signal is observed) is governed solely by the illumination optics, rather than being governed by both the illumination and detection optics as in confocal microscopy [48]. Another consequence is that this technique usually prescribes the use of pulsed laser illumination, which achieves very high instantaneous power by temporally 'focusing' the beam, through mode-locking or q-switching. These techniques can achieve the necessary power densities at average output powers of just $3 - 10$mW. Descriptions of these effects are outside the bounds of this thesis, but good discussions of pulsed laser sources can found in references [49, 50]. TPEF has also been performed with simpler and more affordable continuous wave (CW) lasers at powers of $50 - 200$mW [51].

Two-photon excitation microscopy (TPEF) is most useful when imaging in highly scattering samples, such as biological tissue. In confocal microscopy, illumination light tends to scatter before reaching the focal plane, reducing signal deep into tissue. Furthermore, excitation from this scattered light can scatter back into the objective and through the confocal pinhole, causing unwanted background in images. In TPEF this is highly unlikely to happen as scattered illumination typically does not have the necessary power density to nonlinearly excite fluorescence. The excitation wavelengths for TPEF, often in the near-infrared $700 - 1200nm$, are also better suited to imaging in biological tissue, as they are less scattered and absorbed (and thus also cause less photodamage) [52, 17, 53].

2.2.2.1 *SHG, THG and CARS*

The birth of nonlinear excitation via two-photon microscopy quickly led to the development of several other nonlinear imaging approaches. While two-photon microscopy is an incoherent technique, exciting fluorescence in a molecule and waiting for spontaneous emission, other techniques such as second

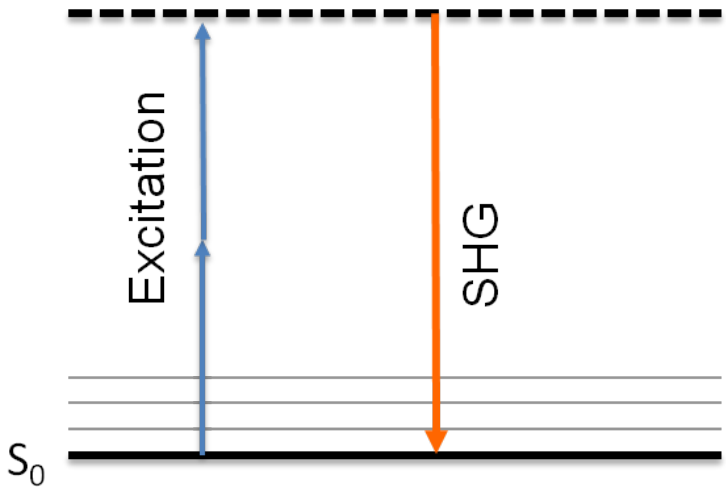


Figure 8: Jablonski diagram of second harmonic generation in a molecule. 2 incoming photons excite the molecule into a virtual state, which instantly relaxes while emitting SHG.

harmonic generation (SHG), third harmonic generation (THG), and coherent anti-Stokes Raman spectroscopy (CARS) are coherent: emission from molecules is stimulated by the incident photons. In SHG, 2 photons are effectively 'upconverted' by the molecule into one with twice the energy of the incident photons, as illustrated in a Jablonski diagram in figure 8.

This difference between TPEF and SHG manifests in several ways, namely a much higher dependence of SHG on beam focus and sample distribution, since as a coherent effect it depends on both the amplitude and phase of the illumination, rather than simply the illumination intensity. Additionally, harmonic generation and other nonlinear effects depend highly on a medium's electromagnetic susceptibilities $\chi^{(n)}$, which are themselves highly dependent on a medium's spatial symmetry [54]. SHG depends on the second order of these, which can be shown to vanish in a centrosymmetric medium.

Thankfully, noncentrosymmetric media are quite common in biological tissue, the most prevalent of these being collagen, a structural protein found throughout different types of tissues. Its fibrous geometry can lead to very large values of $\chi^{(2)}$, and hence large SHG contrast[55, 56, 57]. Other tissues which exhibit SHG are muscular proteins, or microtubules [58].

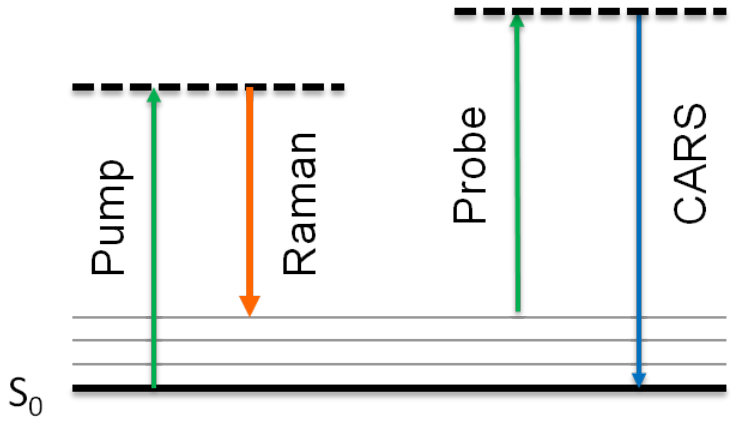


Figure 9: Jablonski diagram of CARS generation in a molecule.

THG is very similar to SHG but combines three photons into one with three times the energy. Efficient THG requires more illumination power than SHG, being dependent on the cube of the electric field - but is dependent on $\chi^{(3)}$, which does not vanish in a centrosymmetric medium. THG can be used to image small, densely packed structures, and has been used succesfully to image lipid vesicle trafficking in cells [59].

CARS is also a $\chi^{(3)}$ effect, but using 3 beams of different wavelength focused to the same point (figure 9). One of these, known as the pump beam, excites a molecule from the ground state into a virtual excited state. In the presence of the Stokes beam, whose wavelength matches the transition from this virtual state to some vibrational state of the molecule, a coupling can be created between the ground state and the vibrational state. This coupling can be probed by a third beam, which excites the molecule from this vibrational state into a another virtual state which relaxes instantaneously to the ground state by emitting a photon at the anti-Stokes wavelength. Therefore, signal is observed when the illumination wavelengths match with the vibrational state energies of the molecule. This allows for a high level of molecular specificity (as in fluorescence microscopy) whereby one can adjust the wavelengths of the pump and Stokes beams to target the vibrational states of a specific molecule [60]. Chirping one of the incident beams allows one to target several different molecules - this is known as multiplex CARS [61].

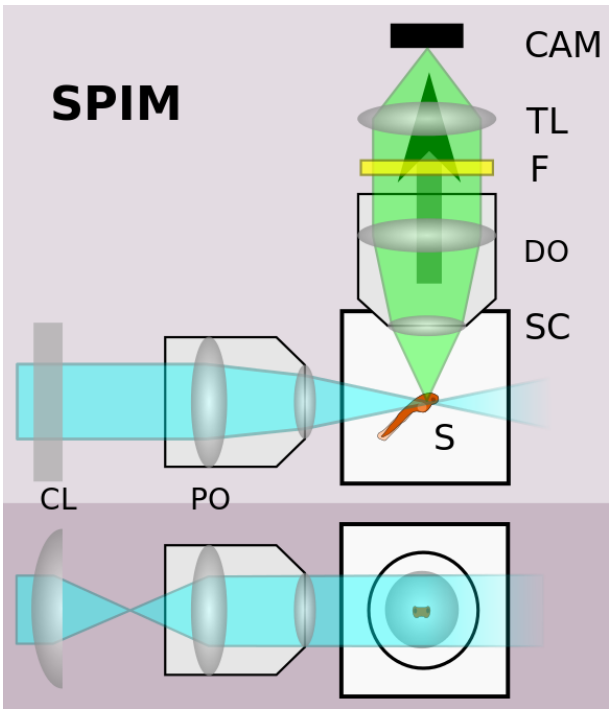


Figure 10: A diagram of the SPIM setup. The light sheet is created by a cylindrical lens (CL) before entering a microscope objective (PO) which focuses the light into the sample (S) . Detection is performed by another objective (DO), fluorescence is filtered (F) and imaged onto the camera (CAM) by the tube lens (TL).[2]

2.3 WIDE-FIELD ACQUISITION

2.3.1 *Light Sheet Microscopy*

A more conceptually simple way of providing sectioning in a microscope is to construct a setup capable of only illuminating a single plane at once, rather than illuminating the whole sample and using confocal-type methods to cut out unwanted image contributions. This allows one to recover a sectioned image from this type of setup by taking a simple widefield image; scanning the sample through the illumination allows one to capture 3 dimensional data as well. Illuminating only the plane of interest also reduces photo-damage and associated effects, particularly when imaging live samples [62, 63].

This technique has its roots in Ultramicroscopy, which optically sections by illuminating a sample with a thin sheet of light [8]. It was first adapted to

fluorescence imaging in 1993 for the purpose of imaging large samples [64], and later adapted to live imaging of smaller samples [16].

The first versions of light sheet microscopy as applied to fluorescence used a cylindrical lens to focus laser light in one dimension, allowing a light sheet to be created with which one could illuminate a sample in a single plane. Detection was then performed orthogonally to this, capturing a sectioned image directly. In Selective Plane Illumination Microscopy (SPIM), a cyclindrical lens is used before a microscope objective, meaning that much smaller light sheets can be created by leveraging the far higher numerical aperture and optical quality available from the objective. Using this technique, a light sheet only a few hundreds of nanometers or microns thick can be created, using the same detection apparatus as before but allowing for far smaller samples to be imaged [65]. Because both the illumination and detection objectives must remain static relative to each other in order to maintain focus, in this setup the entire sample is usually translated instead.

An important consideration when working with a SPIM microscope is that a balance must be achieved between the illumination NA and hence the thickness of the light sheet, and the field of view of the detection objective. For example, with a 60x 1.0NA detection objective, a $2.2 - 2.4\mu m$ light sheet can be created over the whole field of view with a 10x 0.3NA illumination objective.

Although SPIM has advantages in its relative simplicity as compared to techniques like confocal microscopy, the first versions of this microscope had significant issues which have been addressed in more recent years. The use of a single light sheet means that areas of a sample can becomed shadowed by other highly scattering or absorptive areas; using 2 counter-propagating light sheets can compensate for this [66]. Constructing a setup with detection on either sides of the counter-propagating light sheets has also been performed in recent years, allowing for faster imaging of samples [67, 68]. Another approach to improving performance with regards to thick or scattering samples is to combine this technique with two-photon excitation [69]. Yet another

approach scans a laser focus accross the sample to generate the light sheet, rather than using cylindrical optics [70].

In order to escape the restriction of refocussing by moving the entire sample, which can be problematic with large or live samples, Oblique Plane Microscopy (OPM) was invented in 2008 [71]. In this type of setup, the light sheet is produced by the same objective used to detect fluorescence, by coupling the light sheet into the objective at an angle $\sim 60^{\circ}$. A side effect of this illumination paradigm is that images are produced with significant distortion - in order to compensate for this a second objective is used to create a virtual image of the sample outside the microscope, which is then imaged by another objective at an angle to this one [72, 73]. OPM's capability for high speed volumetric imaging has recently been used to study calcium ion dynamics in cardiac myocytes in 3D [74].

2.3.2 *Structured Illumination*

Arguably, structured illumination is in fact a generalisation of confocal microscopy, since all confocal methods rely on the structure of the illumination pattern to exhibit optical sectioning. However, usually this name is reserved for techniques where the requirement for a confocal image to be generated physically on a camera without post-processing is relaxed, instead relying on combining several images to reconstruct a confocal image. The technique was first envisaged by Neil and Wilson [18], influenced by Lanni's earlier work using interference fringes [75].

2.3.2.1 *Using piezo shifted grids*

This setup consists of a grid mask placed at the primary image plane of the microscope such that the grid pattern is imaged onto the sample. This grid pattern only appears at the focal plane - outside of this the grid is blurred into a uniform illumination. This means that the in-focus information is coded

with a modulated pattern which can be picked out later in post-processing. By shifting the grid with a piezo element, several images can be taken with different grid shifts, allowing a whole-field image to be created.

Assuming an approach taking 3 separate grid shifts (phases), a confocal image from this setup can be reconstructed using a brief consideration of the frequency content of each image:

$$I_{conf} = \left[(I_1 - I_2)^2 + (I_1 - I_3)^2 + (I_2 - I_3)^2\right]^{\frac{1}{2}} \tag{14}$$

With I_1, I_2, I_3 being images with phase shifts of 0, $\frac{2\pi}{3}$, and $\frac{4\pi}{3}$ respectively [18]. By simply adding together all three phases, a conventional image can be calculated.

A variation on this idea is the Zeiss Apotome microscopy system, which uses a galvanometer to shift the grid pattern [76]. This technique requires precise moving parts, since inaccurate shifting of the grid can cause artifacts and degradation in the resulting image.

2.3.2.2 *Using Stripe LEDs*

An improvement on the piezo shifted grid technique is to use a programmable LED stripe array to generate the pattern instead [19], based on developments in the manufacture of addressable micro-displays [77, 78]. This has the advantage of not requiring any moving parts, and so does not suffer from inaccurate shifting as in the previous case. Additionally, the setup is slightly simpler, not requiring any mask in the illumination path since the light is generated in the desired pattern.

However, stripe LEDs can suffer from several defects in manufacturing which limit the performance of the setup: each individual stripe must be uniformly emitting, which is not currently the case. Additionally, in many cases one or several of the stripes in the LED's do not function, causing artifacts and resolution degradation in the image. Finally, occasionally even

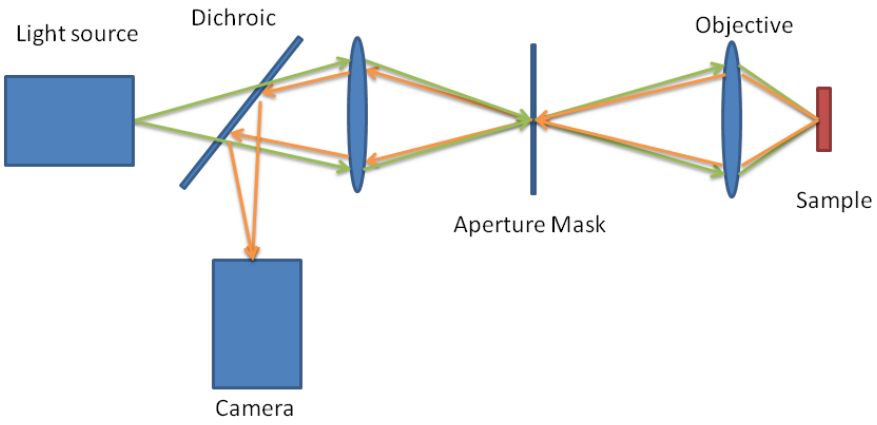


Figure 11: Schematic diagram of the aperture correlation microscope. The aperture mask is imaged onto the sample and return fluorescence passes back through the mask, where it's split from illumination by a dichroic and imaged to a camera.

harmonics are present in the stripe, further inhibiting the performance of the microscope.

2.3.3 *Aperture Correlation/PAM Microscopy*

After the development of Nipkow disk systems, several systems aimed to increase the light efficiency and remove the need for laser illumination by increasing the density of the pinholes. However, in this type of system decreasing the distance between pinholes increases the likelihood of pinhole cross-talk, whereby defocused light from one pinhole enters adjacent ones, resulting in a background offset and loss of sectioning.

Developments in camera technology and computational power in the 1990s allowed the creation of two similar techniques which were able to deal with this background offset through a post-processing subtractive step. The first of these, called aperture correlation, was first invented in 1996 by Wilson et al. [79, 21, 20] using a rotating disk similar to a Nipkow design. In fact, the experimental setup is almost identical to Nipkow disk microscopy, consisting of an aperture mask placed at the output focal plane of the microscope and

a camera focused on the mask. In this instance, an incoherent white-light source is used to illuminate the mask. At the camera, as the disk rotates a confocal image builds up in addition to widefield background. Subsequent acquisition of a widefield image is performed, and this is subtracted from the previous image, yielding a confocal image. More in-depth theory of operation is presented in chapter 3, where a discussion of mask patterns as well as a 2 camera version of this system is presented, which takes advantage of light rejected by the aperture mask coming from the sample to improve the sectioned signal.

This technique was also implemented using a digital micro-mirror device (DMD), where illumination incident on the DMD is reflected into the microscope forming a pattern. Return light is reflected from the DMD back to the camera in the same fashion as light would be transmitted to the camera in aperture correlation. Subtracting a widefield image from this yields a sectioned image, as in aperture correlation. Known as a programmable array microscope (PAM), it offers video-rate optical sectioning with no moving parts[80, 81]. A 2 camera version of this microscope similar to that introduced in chapter 3 was also created, by reflecting light missing the 'active' DMD pixels to a separate camera. This allows for 'single-shot' sectioned imaging, reducing motion artefacts and improving light efficiency and signal[82]. These types of microscopes, by incorporating the use of a Gated Optical Intensifier (GOI) have also been used to perform wide-field fluorescence lifetime imaging (FLIM) on samples [83].

2.3.4 *Super-resolution with Structured Illumination*

Building upon attempts to construct a coherent version of the structured illumination microscopes discussed earlier [84, 85], Gustafsson invented a structured illumination microscope capable of lateral super-resolution, surpassing the conventional limit by a factor of 2 such that information is resolvable up

to $s = 4$ [86]. The principle behind this functioning is similar in implementation to other SIM techniques, but more grid shifts are used as well as several different orientations of the grid. In the detected image, frequency content from outside the observable region has then been shifted by the illumination into the observable region. By making use of the different phases and orientations in different images, this frequency content can then be separated back out and recombined to its correct position (using a more complex algorithm than equation 14), forming a super-resolved image.

In order to shift high lateral frequency information into the observable region of frequency space, the grid used in this type of SIM is roughly twice the ideal grid frequency of the techniques explored earlier, approaching the cut-off of the optical transfer function. Because the maximum axial extent of the optical transfer function is at $s = 1$, using a grid frequency close to $s = 2$ means that little information from the 'missing cone' will get shifted into the observable region. This means that this type of SIM is unable to provide strong optical sectioning, making it unsuitable for thick samples or imaging into deep media. In order to address this, a version of this microscope offering 3D super-resolution was constructed, using 3 interfering laser beams rather than 2 as previously. This restricts the interference pattern at focus to a smaller region, allowing this microscope to section as well as offer lateral super-resolution. Striking images showing very high contrast have been produced on this setup showing microtubules, showcasing a lateral resolution of $120nm$ and axial resolution $309nm$ at excitation and detection wavelengths of $488nm$ and $520nm$ respectively (figure 12). Commercially this type of microscope is available as the Deltavision OMX [87]. Experiments combining TIRF illumination with super-resolved SIM have also yielded impressive results [88].

This type of SIM has certain disadvantages in that imaging into deep media is difficult, due to loss of contrast in the illumination pattern, particularly in highly scattering samples. Imaging also takes a long time, due to having

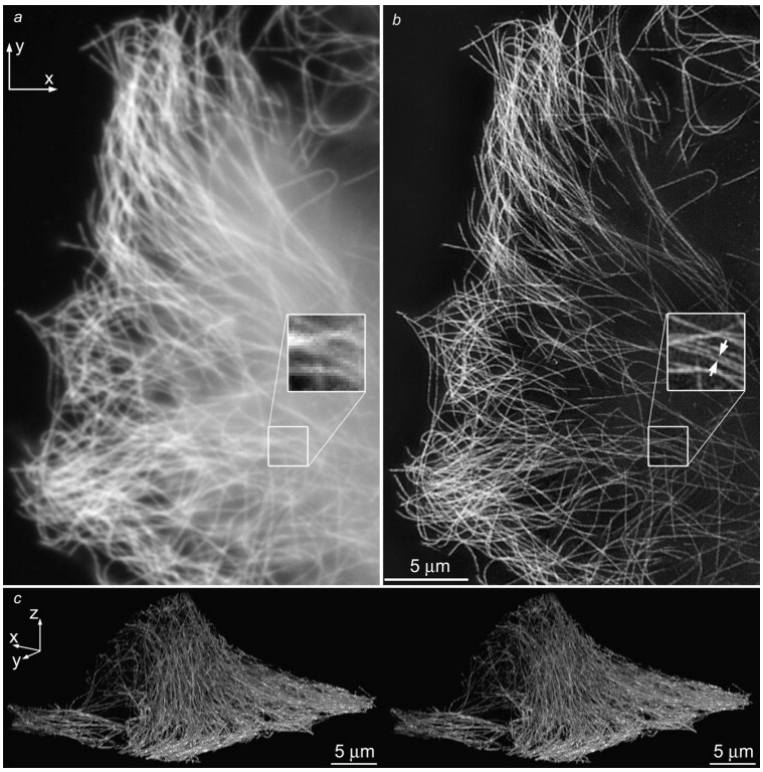
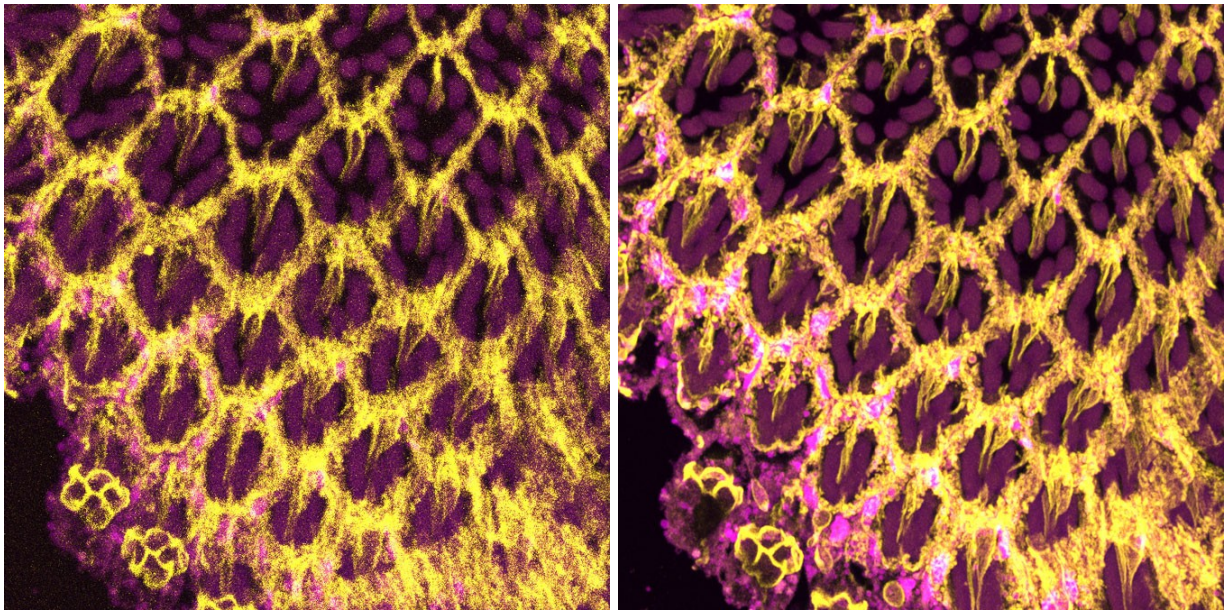


Figure 12: Axial maximum intensity projections of the microtubule cytoskeleton in HeLa cells, with a widefield image on the left and 3D SIM image on the right. A stereo projection of the data is underneath. Image reproduced with permission from Elsevier. [3]

to capture several different phases and orientations of the grid pattern per section. Like other SIM microscopes, shot noise from widefield background can also become an issue.

2.3.5 *SIM with point-like illumination*

There exist two very recent methods in SIM microscopy that leverage the ideas behind resolution enhancement and background subtraction but attempt to address the shot noise associated with the background. These are roughly analogous to confocal microscopy and Nipkow disk confocal microscopy, however making use of extended detection sources and post-processing to enhance the final resolution. The first of these to appear, named image scanning microscopy (ISM), was actually first envisaged by Sheppard in 1988 [89],



(a) Confocal (b) Airyscan

Figure 13: Images acquired from the Zeiss Airyscan microscope.[4]

but developments in camera technology and computer processing made this technique viable only recently [90, 91].

In ISM, illumination is performed with a scanning laser focus, just as in confocal microscopy. Rather than detect through a small pinhole with a PMT, a CCD is used to capture signal passing through a large confocal pinhole (to provide optical sectioning and hence reduce shot noise from defocused background at the detector), where we can treat the central pixel on the CCD as a small confocal pinhole. However, if we consider the CCD as an array of small confocal pinholes, we can treat this as an image reconstruction task. It can be shown that an acentric, shifted pinhole produces an image shifted by half the displacement of the pinhole, with roughly the same resolution as a central pinhole. For example, an off-axis CCD pixel at a distance d from the optical axis will detect an image shifted laterally by $\frac{d}{2}$. Reassigning the images created by off-axis pinholes to a central position and summing over these contributions can yield an image with up to twice the lateral resolution as conventional microscopy, although in practice a factor of 1.7 is observed. In figure 13, images taken with the Zeiss Airyscan microscope compared with a

confocal microscope can be seen. Clearly, the ability to capture more photons using this methodology results in not just higher resolution but also much higher signal.

A parallelised version of this detection technique was invented in 2012 termed multifocal structured illumination microscopy (MSIM), whereby sparse illumination patterns generated and subsequently detected on a DMD (as in PAM microscopy) allow physical rejection of out-of-focus light [92]. The experimental setup of this microscope is effectively the same as in PAM microscopy, the DMD being imaged into the focal plane of the microscope. The pitch of the DMD will hence define the illumination spot size: here, a demagnification step of 90x allows each DMD pixel to produce a diffraction limited spot in the focal plane, while return fluorescence sees each pixel as a confocal pinhole. The illumination pattern here is sparse as in Nipkow disk microscopy so as to avoid cross-talk between adjacent illumination spots and retain the ability to optically section. Several images are taken as the illumination is shifted accross the sample as in SIM microscopy, and the detected stack of images consists of several images at different shifts. In order to calculate a sectioned image from this, the detected grid of points is pinholed (each point is multiplied by a gaussian function with a standard deviation of 162nm, slightly larger than the detector pixel size) and then scaled down at each spot in the image. This is then summed over the whole field and deconvolved to enhance the higher spatial frequency content.

In 2013, a follow-up to the original paper was published, in which the computational task of reconstructing a super-resolved image is performed optically instead [93], permitting images to be acquired in real-time from this setup. In this configuration, the DMD is replaced by a micro-lens array used to generate illumination. An array of pinholes, rather than the DMD pixels, provides optical sectioning. The scaling step is performed by another matched micro-lens array which is finally descanned onto a camera for acquisition, yielding an image with a $\sqrt{2}$ improvement in lateral resolution over

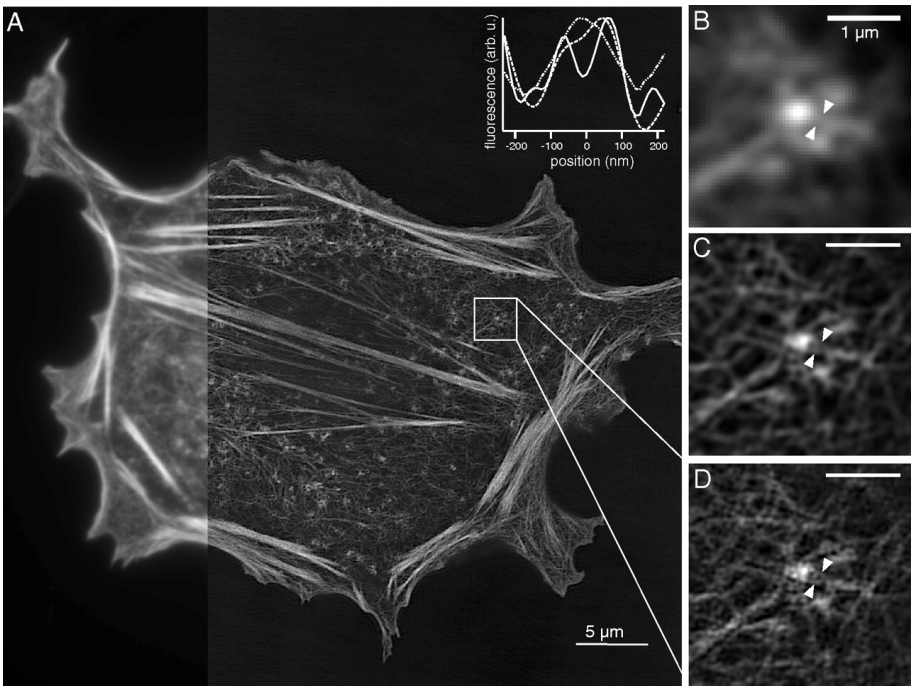


Figure 14: Mammalian CHO cell imaged with non-linear SIM. Subset of the data enlarged on the right is (B) TIRF microscopy (C) SIM-TIRF (D) Nonlinear SIM-TIRF. [5]

conventional microscopy. Performing the deconvolution step on this data computationally can finally double the resolution compared to a widefield image. The axial resolution of this system is comparable to point scanning confocal microscopy.

2.4 UNLIMITED SUPER-RESOLUTION

2.4.1 *Non-linear SIM*

First conceived of by Heintzmann in 2002 [94], non-linear SIM proposes being able to achieve theoretically unlimited resolution by exciting a non-linear response in a fluorescent sample to illumination. Because the highest spatial frequency that can be coupled into a microscope objective is $2\nu_0$, assuming illumination with this frequency appears in the fluorescence response of the sample the maximum limit remains $4\nu_0$. If we consider the case of fluorophore

saturation, however, the molecule begins to respond non-linearly to illumination and behaves as if higher orders at multiples of the incident illumination are present.

Assuming illumination at the highest resolvable frequency $2\nu_0$, this implies that fluorescence will respond as if under illumination at $4\nu_0$, $6\nu_0$ etc. The fluorescent response from these frequencies, as with standard SIM, results in a replication of information at higher spatial frequencies down to the observable range. Performing the same SIM deconvolution as earlier with several different phases and orientations, one can separate out the different contributions back to their proper regions in Fourier space, reconstructing an image with theoretically unlimited resolution. This was demonstrated experimentally by Gustafsson in 2005, who achieved a lateral resolution of $50nm$ by imaging beads [95].

In practice, of course, completely unlimited resolution is impossible due to photobleaching associated with the illumination powers used, as well as the availability of signal with which to perform the reconstruction. The extremely high powers required to excite a nonlinear response through fluorophore saturation are also highly damaging to the fluorophores themselves. To make matters worse, fluorophores also tend to emit fewer photons before bleaching when under saturated conditions. This is compounded with the fact that a great deal of orientations and phases are required to deconvolve the detected image (as it now contains contributions from several different illumination frequencies), resulting in the requirement for high signal to compensate for the shot and readout noise of so many frames. Using such high illumination powers also makes the technique unsuited to imaging biological samples, where damage would certainly occur very quickly.

In 2011, non-linear SIM was attempted again by Rego in a TIRF microscope configuration, but without using fluorophore saturation in order to achieve a non-linear response [5]. Here, reversible photoswitching of a fluorescent protein led to a non-linear response to illumination occurring at 6 orders of

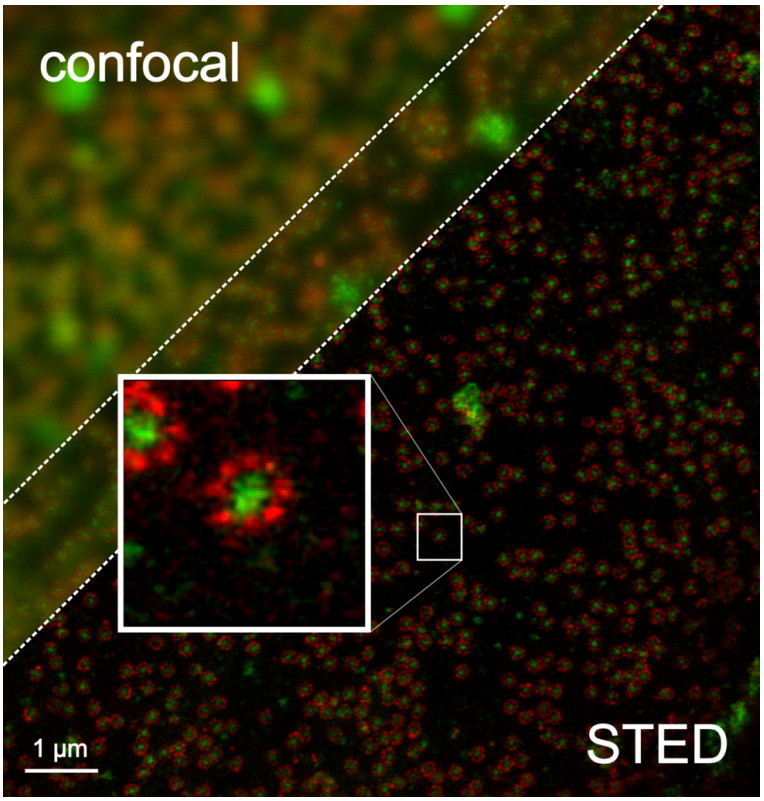


Figure 15: An image of cell nuclei comparing STED microscopy to confocal.[6]

magnitude less than in the previous case. Biological samples were imaged and a lateral resolution of 40*nm* was achieved (see figure 14), proving this technique's viability for imaging of biological tissue.

2.4.2 *Stimulated Emission Depletion*

Another non-linear technique for unlimited super-resolution, this time based on an effect called stimulated emission depletion (STED), was pioneered by Hell in 1994, before many of the other techniques presented in this chapter [96]. Stimulated emission, which we have not covered before, is a mechanism which relies on the presence of an excited molecule and light with an energy matching the downward transition of the molecule resulting in a higher probability of a transition occurring. The light resulting from these transitions,

which is in phase with the light stimulating the transition, is called stimulated emission.

In the fluorescence applications we have discussed thus far, we have assumed that the Stokes' shift between excitation light and fluorescent emission is large enough that there is no chance of illumination causing stimulated emission. If we were to shine a powerful second beam on the sample which was specifically tuned to excite stimulated emission, we might expect to completely overwhelm any fluorescent emission from the sample. In STED, this is exactly what is done, except that the beam is structured such that it turns off fluorescence from a large area except for a small area at the focal spot of the fluorescence excitation beam [97]. The beam used to deplete fluorescence is a Bessel beam, otherwise known as a 'doughnut beam' due to its shape. The excitation spot can be provided with a focused laser, and these are scanned across the sample similarly to confocal microscopy.

In this configuration, STED provides no inherent optical sectioning. But by tailoring the shape of the depletion beam in 3 dimensions using counter-propagating beams, fluorescence depletion can happen in 3 dimensions, allowing very high axial ($33nm$) as well as lateral resolution ($\lambda/23$) [98]. STED has been used to image in live mammal cells [99, 100] as well as in plant cells [101], permitting investigation into processes which would otherwise have been impossible. Parallelisation of STED was also achieved by forming a grid of 'doughnuts' using the principles behind nonlinear structured illumination, permitting much faster imaging speed [102].

STED has some significant advantages over other super-resolution techniques: most importantly, it provides super-resolution without any post-processing. Also, the fluorescence generated in STED is ideally background free, meaning that detectors can devote their full dynamic range to signal collection. A comparison of images from Confocal and STED microscopy is in figure 15.

2.4.3 *Molecular Localisation*

Further to the development of photoactivateable fluorophores which have made STED and non-linear SIM possible, another class of techniques capable of molecular localisation has appeared in more recent years. First demonstrated by Betzig [103] (and almost simultaneously by two other groups [104, 105] under the names PALM and STORM), these techniques rely on the ability of certain fluorescent molecules to remain in a dark state until activated by tailored wavelength illumination. They also rely on these dark states having a long lifetime as compared to the fluorescent state. By choosing fluorescent molecules with a high probability of transitioning into a dark state from the excited state, and weakly illuminating a stained sample with a beam tailored to push molecules from the dark state to the bright state, while simultaneously exciting fluorescence with a second beam, one can be relatively certain that the fluorescence that is observed is from single isolated molecules. After detecting sufficient photons, spots that are observed can be reasonably assumed to come from a single molecule, such that they can be localised by simply evaluating the barycentre of the spot. The resolution of this microscopy technique is therefore limited only by noise and the number of photons that can be observed.

The resolutions achieved by techniques like PALM and STORM are comparable to STED microscopy. The greatest advantage to these over techniques like STED is their simplicity: all that is required to construct a microscope such as these is illumination with the appropriate wavelengths and a sample which has been appropriately labelled with photoactivatable molecules. The drawback from these techniques is the time taken to produce an image - often several minutes or more.

2.5 CONCLUSION

In this chapter, imaging in a conventional microscope was examined, revealing how it is incapable of optical sectioning. Confocal microscopy was then introduced, the first optically sectioning microscopy technique to be implemented, relying on a pinhole to block out-of-focus fluorescence light. Following this was a review of many of the developments in microscopic imaging since then. Multiphoton techniques like TPEF were then discussed, as well as widefield illumination techniques like SPIM and SIM microscopy. Finally, unlimited super-resolution methodologies were briefly reviewed.

3

APERTURE CORRELATION MICROSCOPY

3.1 INTRODUCTION

As was discussed in Chapter 1, conventional microscopes are not capable of optical sectioning - recovering the solely in-focus plane of the microscope objective. By considering the imaging of spatial frequencies through a microscope objective, it becomes clear that the lack of attenuation of the zero spatial frequency makes this impossible. Structured illumination is presented as one way of filling this missing cone in the OTF, by encoding this information at other spatial frequencies and computing a final sectioned image.

Here we describe an Aperture Correlation Microscope which additionally makes use of a structured detection step, by illuminating and detecting through the same grid, which is implemented as a pattern etched onto a disk. This microscope was first invented in 1996 by Wilson et al. [79, 21, 20], at a time when camera performance and computational power were becoming good enough to cope with these imaging methodologies. The programmable array microscope (PAM) is analogous to this microscope, but using a digital micromirror device (DMD) to take the place of the aperture mask used in this setup. The use of a DMD offers some advantages, such as the ability to tailor the mask pattern on the fly, or experiment with patterns other than those that can be easily spun on a disk. A version of the PAM microscope constructed with 2 cameras, imaging light missing the illumination pixels in the same way as we do here, has been constructed before [82].

The experimental setup for this microscope shares a lot in common with a Nipkow disk microscope in the sense that it illuminates and detects through

a spinning disk, although we make use of structured illumination in that the requirement of recovering a sectioned image directly is relaxed. By placing the disk at an angle and imaging both light transmitted through it from the microscope and light reflected off the back to 2 cameras, we can build up 2 separate images: the transmitted one is composed of a conventional image plus additional in-focus information, while the reflected image contains a conventional image minus the in-focus information. By simply subtracting these frames from each-other, we can recover a final, sectioned image.

Since both frames can be acquired simultaneously, this technique is robust against motion artefacts, making it particularly useful in live-cell imaging. This is bolstered by the fact that, with a 50% transmissive disk, it is also highly light efficient, resulting in less photo-bleaching and damage to samples. This type of microscope has been developed by Aurox ltd, an Oxford University spin-off company, and their designs are resold commercially as the Zeiss Vivatome, although that system images both transmitted and reflected images to separate regions on the same camera, reducing the size of the field. The system is sold as an attachment to a conventional microscope, fixing itself to the output port. Here we present an aperture correlation microscope operating in fluorescence mode which uses 2 separate cameras, resulting in the largest possible field size. A version of this microscope used in brightfield is presented in chapter 5.

In this chapter, we will establish the theory of image formation in an aperture correlation microscope, before discussing the experimental setup of this microscope including optical design and equipment. Experimental results are then presented, showcasing this microscope's performance as a real-time, wide-field sectioning microscope with high light-effeciency, at a relatively low cost.

3.2 THEORY

Aperture Correlation was first introduced in 1996, near the beginning of the invention of structured illumination, as an extension to Nipkow disk microscopy. Originally proposed as a system performing a random temporal modulation of the pinholes using a spatial light modulator, this technique proved difficult to implement due to issues in averaging over the sequence, resulting in artefacts. Fairly quickly, a disk etched with lines was decided upon, due to its ability to naturally average very well by simply spinning the disk.

In this section a working theory of the performance of aperture correlation microscopy is introduced, and the performance of the microscope is modelled for the objectives used. Throughout this section we have neglected the effect of the secondary imaging system from the disk to the camera: as seen later, the imaging system is diffraction limited and designed with a pupil slightly larger than that needed to transmit all of the relevant frequencies, and so would have no effect here.

Perhaps the strongest differentiator between this and most other structured illumination techniques is that it also performs structured detection, much like confocal microscopy. In most other SIM techniques, structured illumination is used to shift high spatial frequencies into lower ones, such that they can be imaged through the microscope optics. Fairly intensive computer post-processing shifts these back out to where they would be otherwise. In aperture correlation, a spatial homodyne detection step is incorporated, whereby detection is also performed through a structured pattern. Because the illumination and detection steps are performed through the same mask, these are in phase: the detection step effectively performs the step that post-processing does in other SIM microscopes by shifting the spatial frequencies back out to where they would be normally.

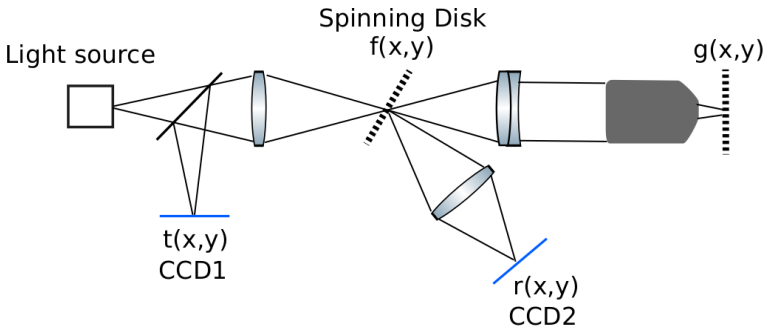


Figure 16: A simple layout of an aperture correlation system collecting conjugate and non-conjugate information, where the locations of the different planes are indicated.

3.2.1 *Resolution*

POINT SPREAD FUNCTION Here we will derive the axial response of this system by obtaining an expression for its PSF. A simplified diagram of the microscope with the different planes indicated is shown in figure 16. In a fluorescence microscope, regardless of the illumination type, detection happens incoherently. We can therefore use the collection PSF:

$$h(x,y) = \left|\mathcal{F}^{-1}\left[P(u,v)\right]\right|^2 \tag{15}$$

where $P(u,v)$ is the pupil of the objective. For an aperture mask shifted to a position (x_0, y_0) we detect a PSF on the camera (assuming perfect imaging from the disk to the camera) q defined by:

$$q(x,y;x_0,y_0) = h(x,y)g(-x_0,-y_0)f(x-x_0,y-y_0) \tag{16}$$

where $g(x,y)$ represents the illumination in the sample plane, and $f(x,y)$ is the aperture mask. In order to detect the PSF transmitted back through the mask, $t(x,y)$, as it rotates, we can integrate this quantity over x_0 and y_0, ie. shift the mask to all positions:

$$\begin{aligned} t(x,y) &= \iint h(x,y)g(-x_0,-y_0)f(x-x_0,y-y_0)dx_0dy_0 \\ &= h(x,y)\iint g(-x_0,-y_0)f(x-x_0,y-y_0)dx_0dy_0 \\ &= h(x,y)\iint g(x_0,y_0)f(x+x_0,y+y_0)dx_0dy_0 \end{aligned} \tag{17}$$

The detection PSF is thus the product of the collection PSF and the cross-correlation of the illumination pattern and the detection mask. Putting this cross-correlation in terms of a Fourier transform, we can then write that:

$$t(x,y) = h(x,y)\mathcal{F}^{-1}\left[G^*(u,v)F(u,v)\right] \tag{18}$$

with $G(u,v)$ and $F(u,v)$ being the Fourier transforms of $g(x,y)$ and $f(x,y)$ respectively. The reflected signal from the mask can be obtained with the detection mask as $1-f(x,y)$:

$$\begin{aligned} r(x,y) &= h(x,y)\mathcal{F}^{-1}\left[G^*(u,v)\mathcal{F}\left[1-f(x,y)\right]\right] \\ &= h(x,y)\mathcal{F}^{-1}\left[G^*(u,v)\left[\delta(u,v)-F(u,v)\right]\right] \\ &= h(x,y)G^*(0,0) - h(x,y)\mathcal{F}^{-1}\left[G^*(u,v)F(u,v)\right] \end{aligned} \tag{19}$$

In this instance, $G^*(0,0)$ encodes the average value of the mask, which we write as $dc\left[f(x,y)\right]$. Up until this point, we have been agnostic to the type of illumination used. In an incoherent illumination setup, we can write:

$$g(x,y) = \mathcal{F}^{-1}\left[OTF(u,v)\times\mathcal{F}\left[f(x,y)\right]\right] \tag{20}$$

$$G(u,v) = OTF(u,v)F(u,v) \tag{21}$$

so that the illumination in the sample plane is simply the mask convolved with the illumination PSF. Using this we can write an expression for the final subtracted PSF:

$$\begin{aligned} w(x,y) &= t(x,y) - r(x,y) \\ &= 2h(x,y)\mathcal{F}^{-1}\left[OTF^*(u,v)F^*(u,v)F(u,v)\right] \quad (22) \\ &\quad -h(x,y)dc\left[f(x,y)\right] \quad (23) \end{aligned}$$

or in 3 dimensions:

$$\begin{aligned} w(x,y,z) &= t(x,y,z) - r(x,y,z) \\ &= 2h(x,y,z)\mathcal{F}^{-1}\left[OTF^*(u,v,z)F^*(u,v)F(u,v)\right] \\ &\quad -h(x,y,z)dc\left[f(x,y)\right] \quad (24) \end{aligned}$$

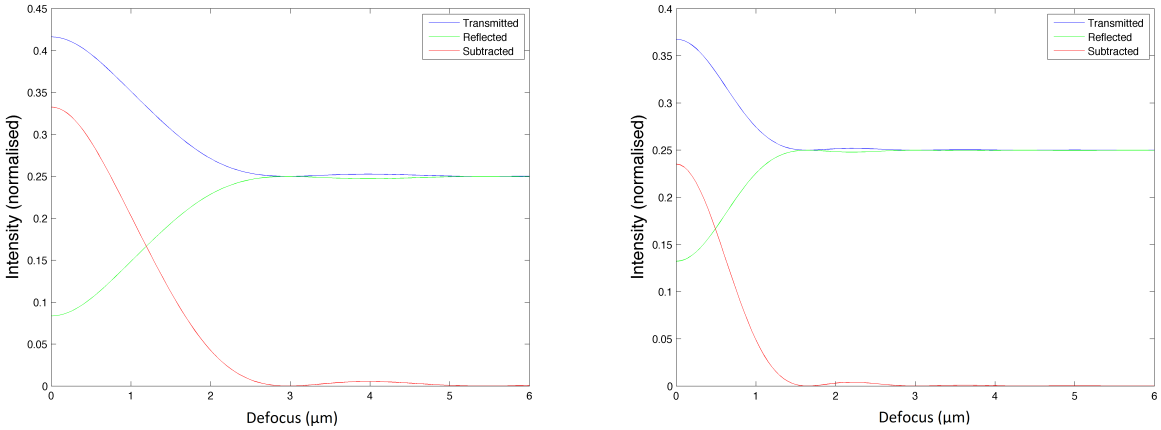
STOKSETH'S APPROXIMATION In order to then model these responses, a model for the incoherent OTF must be determined. In order to perform a full simulation, one could calculate the pupil function at every value of the defocus, and then perform an autocorrelation to find the OTF - this would be very computationally expensive. Thankfully, in his seminal 1969 paper, Stokseth derives a series expansion of the OTF, as well as an approximation which greatly simplifies the form of the expansion and renders it computationally cheap[35]. Here we generally use the approximation, as it was determined that using the exact form does not notably affect the response curves. A more in depth explanation can be found in Appendix A.

$$T(s,w) = \begin{cases} g(|s|)\,\frac{2J_1\left[ws\left(1-\frac{|s|}{2}\right)\right]}{ws\left(1-\frac{|s|}{2}\right)} & if\ 0 < |s| < 2 \\ 0 & otherwise \end{cases} \quad (25)$$

$$g(s) = 1 - 0.69s + 0.0076s^2 + 0.043s^3 \tag{26}$$

DISK FREQUENCY The disks used have 2 sectors etched into them at different radii, one with a pitch of 160µm and the other with a pitch of 80µm. Having the two sectors etched at different radii means that by mounting the disk motor on a translating mount, the sector can be changed easily by simply sliding the disk further in or out of the optical axis. These pitches are related to normalised frequency by $s = \frac{M*\lambda}{NA*p}$, with p the pitch of the disk pattern. This normalised frequency represents the fundamental frequency of the grid, ie. a sin wave with a wavelength of 80µm. For the 40x 0.75 objective used, these pitches correspond to normalised frequencies of 0.18 and 0.36 respectively.

MODELLING These responses were modelled using Matlab, as well as the total intensity response $I = I_T - I_R$. Figure 17 shows these three modelled for disk pitches of both 160 and 80µm. We can see that making the disk pitch smaller leads to a thinner axial response, but also reduces the signal from the microscope - we would expect this given the shape of the 3D OTF. In fact, the maximum axial response would be expected where the normalised disk frequency is at $s = 1$, since looking at the shape of the 3D OTF one would expect that correlating it with a function having a maximum at $k_r = 1$ would result in the largest extent in k_z for a sample with 0 lateral spatial frequency (this corresponds to a disk pitch of 30µm for the 40x 0.75 objective). In practice, the confocal signal from disks manufactured in this way is low, particularly as compared to the widefield background acquired at the camera, resulting in a noisy confocal signal due to shot noise. This would affect the gains in contrast and light efficiency this system is designed to enhance.



(a) $160\mu m$ (b) $80\mu m$

Figure 17: Plots of the response to a thin fluorescent sheet through focus, as a function of defocus, for disk pitch sizes of 160 and 80 microns. The normalised intensity is relative to the illumination intensity, so that 0.5 in the maximum response value.

LATERAL RESOLUTION The lateral resolution of the system can be determined by modelling equation 24, since this equation effectively gives us a 3 dimensional transfer function for the combined system. However, since the disk pitches used in this experiment are quite low, having been chosen for optimal signal and optical sectioning, in practice we would expect very little if any lateral resolution enhancement at all.

3.3 EXPERIMENT

3.3.1 *Experimental Setup*

The experimental setup used for spinning disk microscopy consists of the spinning disk, imaging arms and cameras, as well as an illumination and calibration system. The disk is imaged onto the sample by placing it at the focal plane of the side output port of the Olympus IX51 microscope.

The imaging arms are used to image either side of the disk onto 2 cameras, capturing the transmitted and reflected light on separate cameras. The illu-



Figure 18: A scaled up version of the line pattern and configuration etched onto the spinning disk.

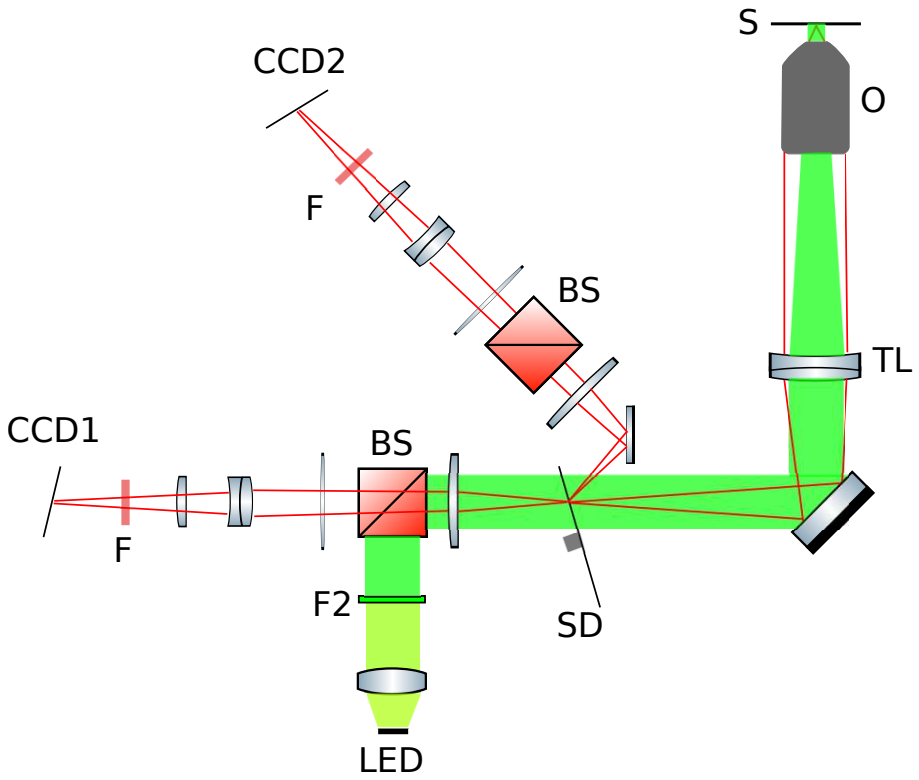


Figure 19: A schematic diagram of the imaging setup. The LED is collimated by a condensor, and then filtered at for 532nm (F2). The beamsplitter BS reflects the illumination through the disk and into the microscope objective O through the tube lens TL. Return fluorescence is imaged to CCD1 and CCD2 through a beamsplitter and long pass filter (600nm).

mination system illuminates the disk - the light source is imaged through the disk onto the back aperture of the microscope objective in order to achieve Kohler illumination. When imaging in fluorescence, appropriate emission/excitation filters are placed in the imaging arms/illumination arm respectively. In this case, green illumination filtered at 532nm is used, and long pass emission filters with a cut-off of 600nm are placed before the cameras. The dichroic has a cut-off of 550nm. The disk used is one from a Zeiss Vivatome, which has 2 disk sectors at different diameters: one with a line pitch of 80µm and the other with a pitch of 160µm. Both of these sectors have a fill factor of 0.5.

Because the objective of this experiment is to optimise the microscope for the best possible performance, each aspect of the system should be as high performance as possible - in particular the imaging arms, for which we have decided on a diffraction limited setup previously designed by Mantas Zarauskas, a former MSc student at Imperial College. These are presented along with optical layouts in subsection 3.3.2. The Cameras used are AVT Stingray F-145B firewire cameras, which were chosen for their price point and sensor (Sony ICX-285). Their noise characteristics are presented in subsection 3.3.3. They are placed at an angle equal to the disk angle to match the tilted image plane.

On the microscope side, an Olympus IX51 inverted microscope is used with several different Olympus objectives: a 40x 0.75 NA aposdk, a 60x 1.2 NA water immersion objective, and a 100x 1.35NA oil immersion objective. This allows us, with one disk, to test the effect of changing the apparent normalised spatial frequency of the pattern. In addition to this, a Prior NanoscanZ stage is used in order to acquire Z-stacks with a stack spacing of 0.1µm.

The tilt of the disk is this system is at 20° to the optical axis: this is done so that the light reflected from the back of the disk is separated from light incident onto the back of the disk before being reflected into the imaging system, while retaining the correct front focal length of the imaging system. In the microscope plane, we expect this to be demagnified by the objective's

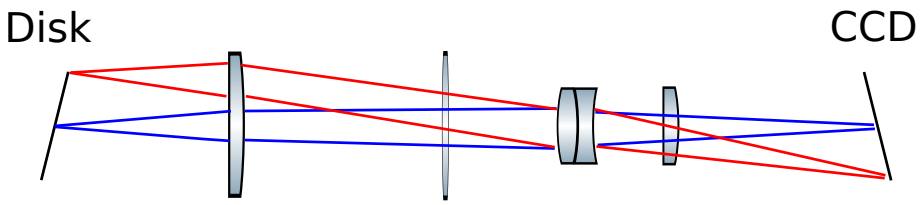


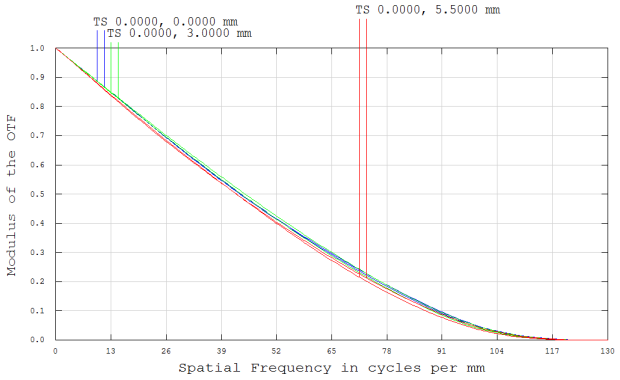
Figure 20: Optical layout of the imaging system from the disk to the camera.

magnification, such that for the 40x objective this becomes 0.01° in the sample plane.

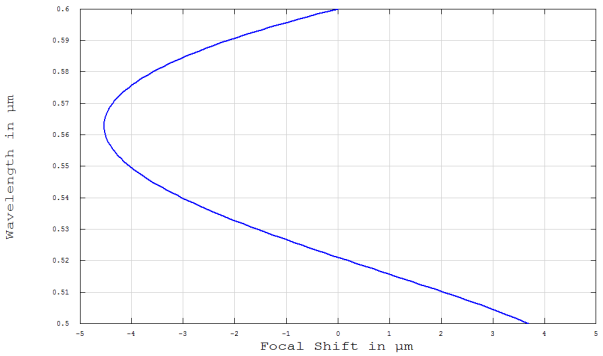
3.3.2 *Imaging Arms*

The imaging arms used to image the disk onto the cameras are identical diffraction limited setups designed in Zemax, composed of 5 elements in 4 groups[106]. A layout of the system is shown in figure 20. Elements are placed so as to avoid any surfaces close the the object or image planes, avoiding issues with scratches or dust appearing in the image. The system was designed to perform throughout a broad range of wavelengths, from 440nm to 700nm, targeting the most used fluorophores and able to cope with the Stokes' shift. The pupil of this imaging system is matched to that of the objectives used, such that no information is lost imaging through to the cameras.

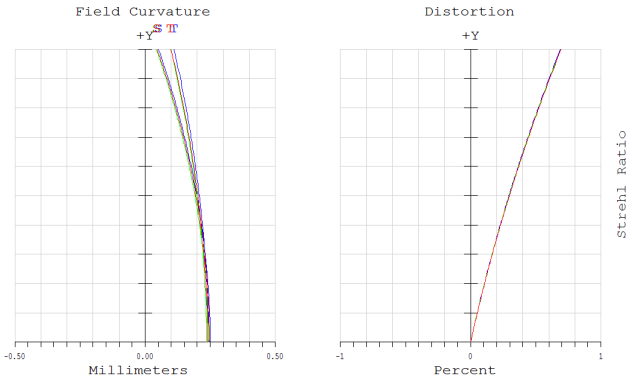
Plots illustrating the performance of the system are presented in figure 21. From a plot of the Strehl ratio against defocus, we can see that the system is diffraction limited within $\pm$180µm of the focal plane. Field curvature has been kept to a minimum here, since the CCD used for detection has a flat surface. Although distortion can be easily compensated in the image processing step, it has also been kept beneath 1%. Perhaps the most important measure of system performance is the MTF, which has been kept above 90% of the diffraction limit through the field and design wavelength range.



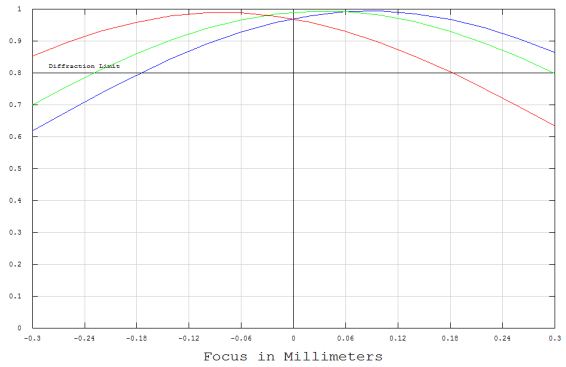
(a) MTF



(b) Chromatic focal shift



(c) Field curvature and distortion



(d) Strehl ratio vs defocus

Figure 21: Figures illustrating the performance of the prototype optics designed for our aperture correlation setup.

	Stingray F145B	Orca R2 (normal scan)
Resolution	1388x1038	1344x1024
Sensor	Sony ICX285	ER-150
Framerate (full frame)	16fps	8.5fps
A/D Bit depth	14bit	12bit/16bit
Pixel Size	6.45μm	6.45μm
Dynamic Range	66dB	70dB
SNR	43dB	-
Price	~$2800	~$14000

Table 1: AVT Stingray F145B Specifications, as compared to the Hamamatsu Orca.

3.3.3 *Cameras and noise*

Scientific CCD cameras can often be bulky, expensive devices. Cameras such as the Hammamatsu Orca are something of a standard, but carry a hefty price tag of approximately $14000. The sensor contained with the Orca itself is not dissimilar to far cheaper cameras such as the AVT Stingray series. A comparison of the Stingray and Orca characteristics is in table 1. A dynamic range of 66dB suggests that a bit depth of 12 will suffice to transfer data from the camera. The Stingray was chosen for this experiment as the price/performance ratio as compared to Orca is very good - the ICX285 sensor is a standard in fluorescence microscopy, and is very similar to the ER-150 found in the Orca. In order to transfer data at a bit depth of 12, which is supported by the camera, a 12 bit packed mode is used, which packages 3 12bit pixels into 2 16bit data types. These are then unpacked into 16bit integers during acquisition. Transferring at this bitrate allows 2 cameras to operate at their full framerate of 16fps over a single firewire bus, allowing the acquisition to take place on relatively cheap hardware.

3.3.4 *Samples*

Several different samples were imaged with this microscope, here we describe how these were prepared and imaged.

MICROSPHERES The microspheres used are Invitrogen Fluocell 1µm spheres, which excite at 540nm and emit at 560nm, well suited to our illumination and detection wavelengths. The samples were prepared by diluting a small amount of initial solution in distilled water, then placed on microscope slide and covered with a no 1.5 coverslip.

A suitable region was found on the slides (with spheres in both areas of disk pitch in the field) and z-stacks were taken with a spacing of 0.1µm between slices. These were imaged using all 3 objectives.

FLUORESCENT THIN SHEETS Thin fluorescent sheets were prepared by spin coating in order to measure the axial resolution of the system. A solution was first prepared by dissolving PMMA in Acetone until saturation (10%wt), then diluting this solution in Toluene at low concentrations ($5 - 10\%$). Toluene/PMMA was chosen after a literature search revealed this to be one of the best choices for creating thin films - Acetone was necessary as PMMA does not readily dissolve in Toluene due to its non-polar nature. Rhodamine B was then added to the solution until saturation [107, 108].

Coverslips (no 1.5) were prepared by sonicating in Ethanol for several minutes and then air drying. The coverslips were then placed into the spin coater and flooded with solution, then spun at 3000rpm for 60 seconds in order to achieve minimum thickness. According to the literature, after air drying, this procedure should result in films $\sim$ 100nm in thickness, well below the expected axial resolution of the microscope. These were then mounted onto a microscope slide and z-stacks were taken with a spacing of 0.1µm between slices. These were imaged using all 3 objectives.

CAROLINA SAMPLES Samples of Lilly Anther pollen prepared by Carolina Biological Supply Company (part no. 304586 [109]) were imaged in this experiment to examine how images of biological samples would appear. The mounting medium for these samples is Caroplastic - a polymer resin with a refractive index of 1.5593. Although this is quite far from the design refractive index of the 40x 0.75NA and 60x 1.2NA objectives used, the sample plane is near to the coverslip ($\leq$ 10µm), such that spherical aberration arising from the refractive index mismatch was not observed to be significant. Spherical aberration presents itself most commonly as a loss of signal in confocal arrangements, since the illumination PSF is spread out such that less power is present at the focal plane being sectioned. A refractive index mismatch also means that the z axis in the resulting images will be compressed, since the axial magnification of the system is proportional to the inverse of the sample refractive index. Z-stacks were taken of these with a spacing of 0.1µm between slices with the 60x and 100x objectives.

3.3.5 *Calibration and Image Registration*

In order to run this experiment, software was written in order to acquire frames from both cameras, align (register) them and then subtract them. The software is built around the Qt toolkit in C++ [110], and is designed to be easy to port to different platforms.

The library used to communicate with the camera is the dc1394 API version 2, a cross-platform API designed for interacting with firewire cameras compliant with the DCAM specification. It also contains some extra functions specific to AVT cameras and allowing control of more advanced camera features such as internal shading compensation. Communication with the Prior NanoscanZ stage is achieved via serial port communication, and is used to automatically acquire z-stack images. The software uses OpenGL in order to draw the images to the screen - the program has been designed to minim-

ise CPU usage by offloading as many tasks to the graphics processing unit (GPU) as possible, which is far better suited to the parallel nature of image processing, as well as being cheap and widely available.

Acquiring a sectioned image from this setup is not as simple as acquiring images from the cameras and subtracting one from the other - one must first be sure the images are captured as simultaneously as possible, that they are as aligned as possible, and that they are normalised to the same intensity profile (to compensate for intensity differences between the images, and within the images, such as vignetting). In practice, the most challenging aspect of this is aligning the images - this step is known as image registration, and is often encountered in biological imaging. Most registration algorithms are designed to work on time series data, where the sample moves over time in an unpredictable way. It is necessary in our setup due to slight differences in alignment and optics between each of the cameras' imaging arms, which are fixed with respect to the acquisition time. The registration algorithm uses the OpenGL library in order to perform as much computation as possible on the GPU, allowing the system to image the whole field in real time, limited only by the framerate of the cameras.

A complete description of the registration algorithm, along with implementation details, can be found in chapter 4.

3.4 RESULTS AND DISCUSSION

3.4.1 *Microspheres*

Images of a 1µm beads were acquired in order to investigate the transfer function of the system. These beads are unfortunately larger than the diffraction limit of the objective (they were the smallest beads available at the time of the experiment), so an investigation into the full lateral extent of the transfer function was made difficult, given that the image will contain a convolution

of the extended microsphere shape with the PSF of the system. That said, we are able to investigate the optical sectioning of the microscope, including observing whether we have filled the 'missing cone' of a conventional microscopy system.

Figure 22 shows a whole field captured with this microscope with a 40x 0.75 NA objective, in focus and sectioned, with the 160µm sector of the disk. A stack was taken of this field, and a single bead was selected to investigate the OTF of the system by performing a 3D Fourier transform on the stack. Because the image is a convolution of the system PSF with a sphere, the result of this operation is the OTF multiplied by the Fourier transform of a sphere, which resembles a sinc function and effectively limits the extent of the function.

Figure 23 shows the result of this operation. Overlaying a Fourier transform of a sphere, given by $\frac{3}{k_r^3}(\sin k_r - k_r \cos k_r)$, shows how the areas of low intensity in this function have masked the transfer function. This function is scaled to fit the data by recognising the $6.45\mu m$ pitch of the detector and $0.1\mu m$ pitch of the z stepping, which determines the frequency coordinates of the FFT of the image. Recognising that the bead used here is half the size of the bead given by the equation (the sphere having a unit radius or diameter of 2), k_r is scaled by a factor of $\frac{2}{6.45} * 512$ laterally and $\frac{2}{0.1} * 500$ axially (512 and 500 being the stack size in x and y, and z respectively). We can see how the first zero in this function clearly overlaps with a minimum in the transfer function of the system. Most importantly, the central region is large enough to show how the 'missing cone' of a conventional microscope has now been filled, illustrating that we have achieved optical sectioning with this microscope.

3.4.2 *Thin Sheets*

Figure 24 shows an in focus sectioned image of one of the thin film samples described in section 3.3.4 taken with the 40x 0.75NA objective. It is clear that

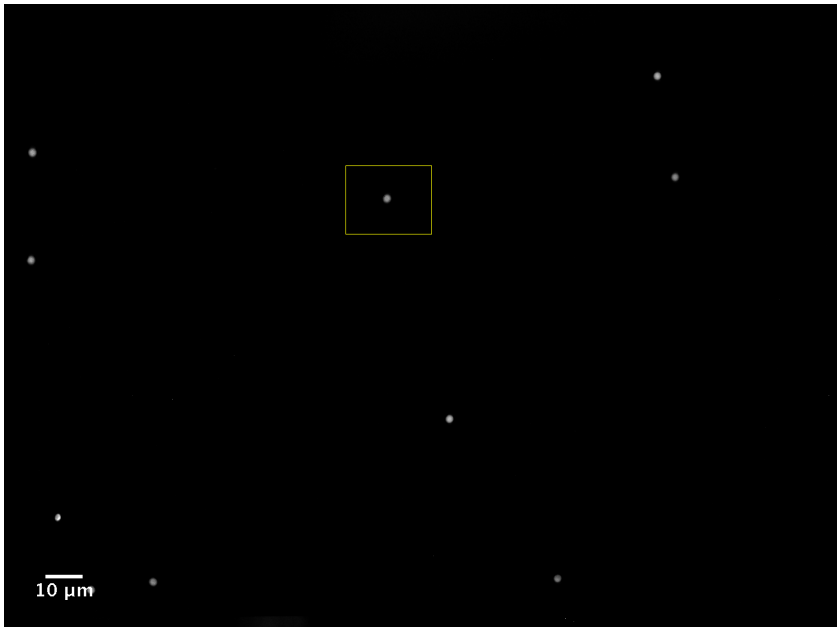


Figure 22: Image of a field of beads, post subtraction. (40x 0.75)

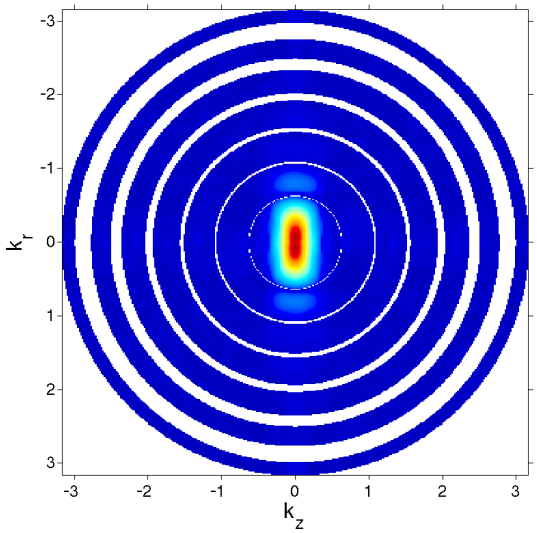


Figure 23: Transfer function of the system, with an overlay in white representing areas of low intensity in the Fourier transform of a sphere.

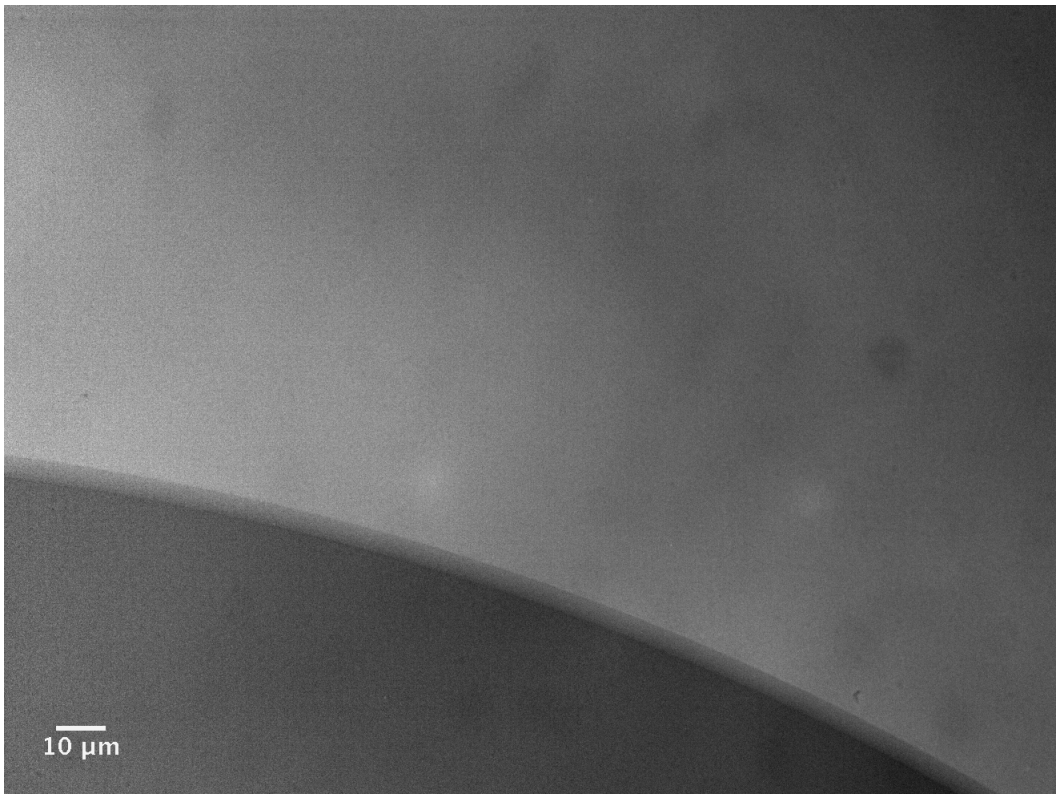
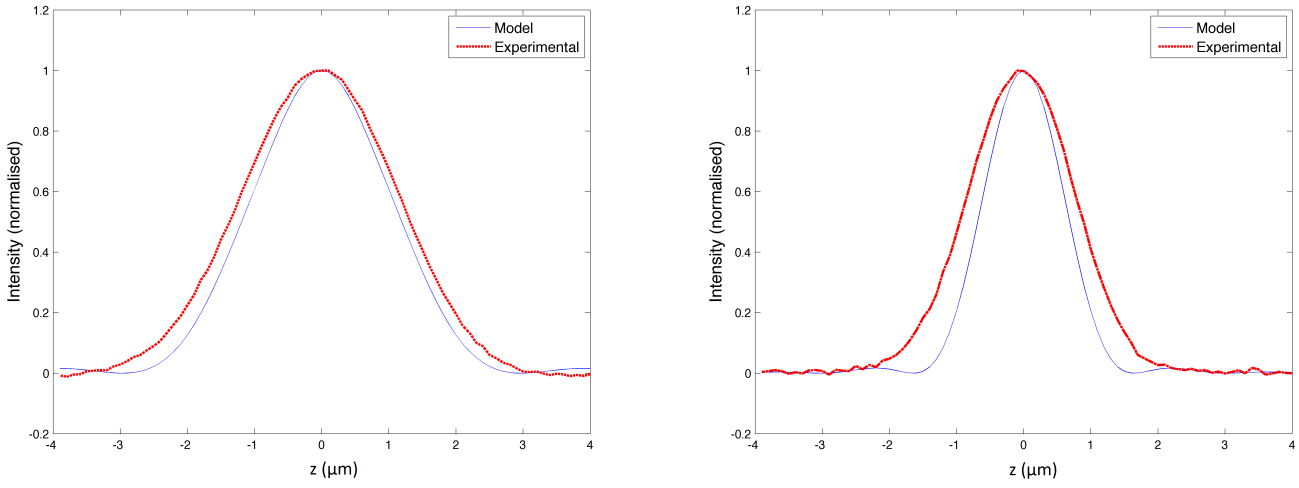


Figure 24: A sectioned image of the spin coated thin film, taken with the 40x 0.75NA objective. The dark portion of the image represents the 80µm sector of the disk, while the bright portion represents the 160µm sector.



(a) (b)

Figure 25: Plots of axial responses accross both 160µm (a) and 80µm (b) disk pitches.

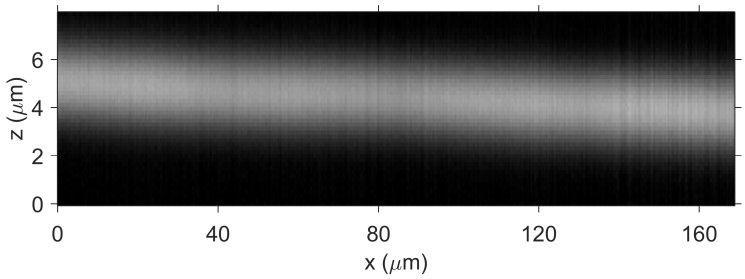


Figure 26: An x-z plot of the thin film data, where the tilt in the image stack is clearly visible.

the signal from the coarser, 160µm section of the disk is greater than the 80µm section, as we would expect from the models described previously. It also appears as though there is a tilt present in the image which becomes clear as one scans through focus; In order to test whether the apparent tilt in the image is the result of the disk tilt or not, an x-z projection was made orthogonal to the tilt direction (figure 26). From this data, the tilt in the sample plane is measured to be $0.6 \pm 0.05°$. The disk tilt of 20°, when demagnified by the objective's axial magnification (related to the lateral magnification by M^2, or 1600), becomes a tilt of 0.01° in the sample plane. We can thus infer that the observed tilt in the data arises from a small sample tilt of $\sim 0.6°$.

In order to compare the axial responses to the idealised, perfectly thin sheet models in section 3.2.1, a small region orthogonal to the tilt is selected and the z profile of this region is plotted. Plotting the profile over a region is performed in order to average out noise, which otherwise would be significant. The result of this is shown in figure 25, where experimental results are shown along with models. In the case of the 160µm pitch grid, the measurements match quite closely with the model, measuring a FWHM of 2.4µm compared a modelled result of 2.2µm. In the 80µm pitch section, we observe a FWHM of 2µm compared to a modelled result of 1.6µm.

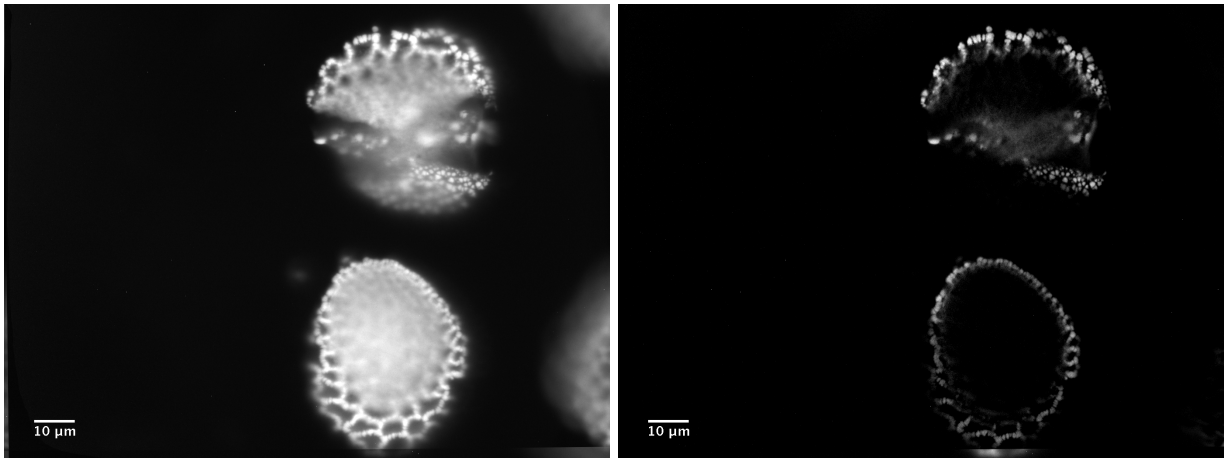
With the target sheet thickness of 100nm, we might expect the measured response to be very approximately 100nm wider than the ideal, perfectly thin sheet which the model is based on, since the measured response will be the convolution of the sheet with the system response. One explanation for

the larger discrepancy between the model and the experiment, particularly in the case of the finer disk sector, is that the thin sheet is slightly thicker (measuring 300nm thick) than intended where the measurement was taken. In several samples striations can be observed at lower magnifications, which could imply an uneven surface of film, or uneven distribution of fluorophores within the film.

3.4.3 *Samples*

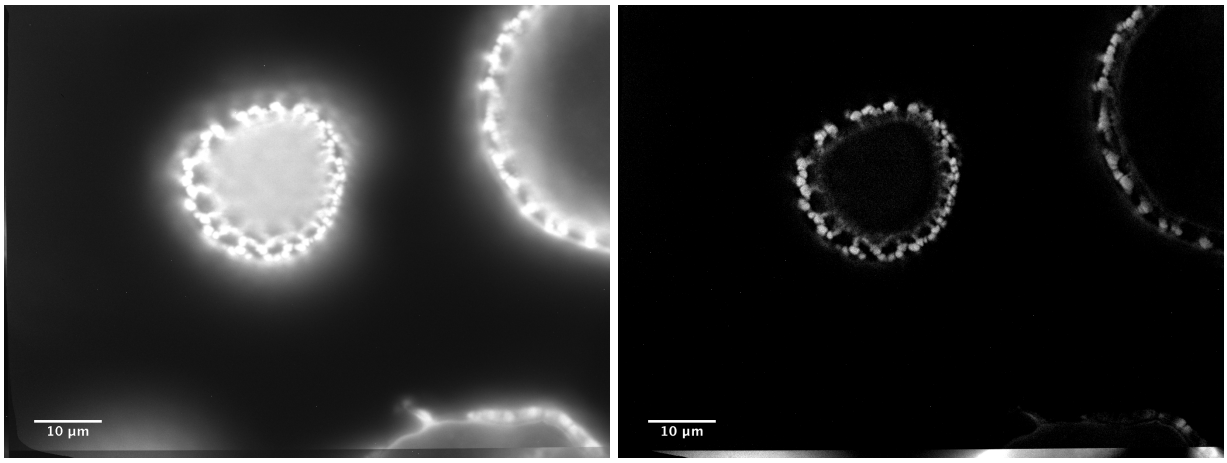
Images of Lilly Anther pollen were acquired at different magnifications in order to illustrate real-world application of the microscope when observing biological samples. Figures 27 and 28 illustrate the difference between widefield images and images from this setup, at intermediate depths into the sample $\sim$ 4µm. The widefield images are obtained by summing images from both the transmitted and the reflected image paths. It is clear that these images exhibit optical sectioning as previously, where out of focus background is clearly removed. The resulting dramatic increase in contrast also makes smaller features apparent in the sample.

By acquiring several images at increasing depth using a piezo stage, z-stacks of these samples were also acquired with a stack spacing of 0.1µm, from which maximum intensity projections were created (Figure 29) as well as a 3D render (Figure 30). The maximum intensity projection chooses a pixel in the final image based on the brightest pixel found at that point in the entire stack. In this way, it creates a projection of the volume along the z direction. These types of images are useful when considering samples or regions of interest which have little 3D overlap and so can be cleanly projected in this way. The images show that these pollen grains have a great deal of fine structure, which makes them ideal for showcasing this microscope's performance. By colour coding the images for depth, we can see that the grains have a spherical shape: this is more evident in the 3D render.



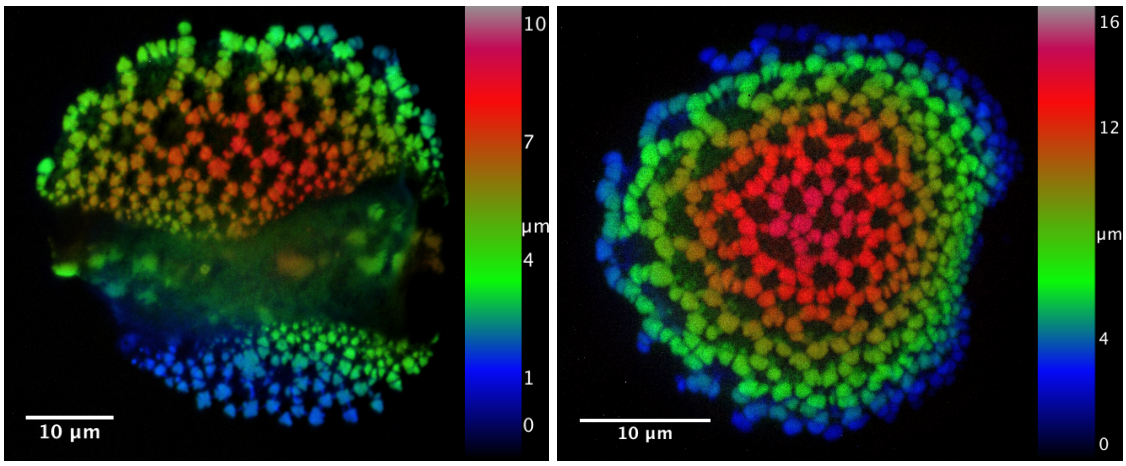
(a) Widefield (b) Sectioned

Figure 27: Images of lilly anther pollen, widefield and sectioned, 60x 1.2NA



(a) Widefield (b) Sectioned

Figure 28: Images of lilly anther pollen, widefield and sectioned, 100x 1.35NA



(a) 60x 1.2NA (b) 100x 1.35NA

Figure 29: Maximum intensity projections of lilly anther pollen image stacks.

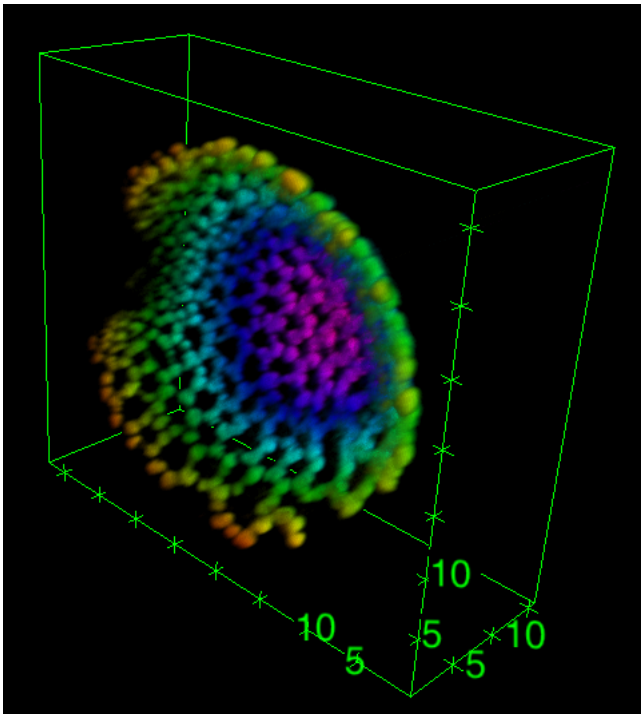


Figure 30: 3D render of a pollen grain. Tick marks are in μm.

3.5 CONCLUSION

To conclude, we have introduced a 2 camera aperture correlation microscope operating with incoherent illumination. The theory of aperture correlation

was established in a first instance, explaining how spatial homodyne detection allows this microscope to section purely by subtracting simultaneous frames from separate cameras. Our experimental setup was then introduced, and equipment choices were justified, as well as this experiment's reliance on a post-processing step to register the images from the cameras before subtraction. Experimental results from the microscope were then presented: images of microspheres are used to calculate a transfer function to find that it fills the 'missing cone' of a conventional microscope. Thin fluorescent sheets were imaged to evaluate the axial response and found to match reasonably well but not perfectly to the theory, most likely due to imperfect thin sheets. Finally, images of biological samples were presented to showcase this technique's ability for widefield sectioning microscopy.

4

REAL TIME IMAGE REGISTRATION

4.1 INTRODUCTION

This chapter describes the image registration algorithm used by the system previously introduced in Chapter 3, also used by the system in Chapter 6. Registration refers to the act of transforming or deforming an image such that its pixels or features line up as precisely as possible to pixels or features in another image; this can be useful not just in medical or biological imaging where features can be aligned across time-series data, but also in astrophotography or military applications. It is also used in photography, where several exposures of one scene can be aligned and processed together in order to produce one image with a higher signal to noise ratio or dynamic range. Existing registration algorithms usually post-process data after acquisition of a whole dataset, implementing feature recognition algorithms to detect points around which to transform the image.

In our setup, a registration algorithm was needed which would be able to perform real-time registration of simultaneous images from 2 cameras at at least 16 frames per second. Existing registration algorithms were unable to provide this kind of throughput, and so a new registration algorithm is described here, designed to leverage the graphics processing unit to assist in high speed registration. Based on our literature search, there have been no other attempts at a GPU-based tiled affine transform, as is done here.

4.1.1 *Background*

As previously stated, image registration is a large field with very useful (and even crucial) applications accross a broad range of subject matters. Here, we will concern ourselves most with introducing registration methodologies most useful in the biological sciences. Some examples of medical applications are magnetic resonance imaging (MRI), positron emission tomography (PET) and computed tomography (CT); all of these methodologies rely on image registration in order to account for patient movement during acquisition, or sometimes in order to perform interpatient comparisons [111].

At its core, registration is the process of calculating a mapping between two images: these mappings can take a wide range of different forms depending on the application and the constraints of the problem. There are 2 main classes of registration, rigid and non-rigid. Rigid mappings are defined as preserving all distances, the straightness of lines, and angles between lines. This restricts this class to rotations and translations - which are conveniently easy to calculate. Non-rigid transformations extend this to shearing and scaling, as well as arbitrary transformations.

One particularly common non-rigid transformation is the affine transformation. This transformation preserves the straightness of lines, but not angles or distances - effectively incorporating rotations, translations, shearing and scaling. These transformations are very commonly used as a pre-registration step before using other, more precise non-parametric algorithms, and also on their own depending on what kind of deformation is expected between the source and target images; particularly so because affine transformations are computationally cheap [112]. Tiled affine transforms (as described in this chapter) have also been used in order to approximate a global perspective transformation [113].

In order to calculate a mapping, there are several different existing algorithms. One that has gained a lot of traction in recent years is intensity

minimisation, whereby the images to be registered are subtracted from each other in order to acquire a metric from which optimisation can be run on the parameters of the desired transformation. Another is through the identification of features that both images share in common - these can be used to quickly calculate global transformations from just a few reference points, by solving for affine or other transformation matrices. By comparing both images' FFTs, simple transformations can also be very quickly calculated [114].

Because the main driving forces in the image registration community are MRI, PET and CT scans (and particularly registering them to each-other), many algorithms exist to quickly calculate rigid mappings between subsequent frames, each with a different mapping as the subject moves throughout acquisition. When registering scans taken from different perspectives, the perspective transform can be used to change the apparent scan angle.

The transformations discussed all deal with creating a mapping between two sets of images, targeting one to match another. These transformations can be performed either forwards or backwards; when applying a forward transform great care must be taken to avoid holes or artefacts appearing in the resulting image, due to the discrete nature of the data. Usually, the backwards transformation is performed instead, selecting a target pixel and looking up its value in the source image using the reverse of the estimated mapping function. This brings to light the issue of interpolation, as looking up floating point coordinates in an integer coordinate system requires some kind of lookup method.

The simplest way of performing this is via nearest neighbor interpolation. This simply sets the target pixel value to the nearest pixel to where the reverse mapping function points to. However, this is extremely prone to artifacts, particularly if the image is deformed significantly by the mapping function. Instead, interpolation is usually done by convolving the image with an interpolation kernel. Bilinear interpolation is the simplest of these, where the target pixel value is set to a weighted average of the nearest 2x2 pixel values

to the desired coordinate. Bicubic interpolation, the next step up, takes the nearest 4x4 pixels to calculate a weighted average. Other examples of interpolation kernels include B-splines, truncated sinc functions, and Gaussians [115]. Some researchers have even investigated higher order polynomials, but conclude that the small increase in accuracy is not worth the greatly increased computation required [116]. Generally speaking, bilinear interpolation offers the best compromise between speed and accuracy [117, 118].

4.1.2 *Why we need registration*

In the systems from chapters 3 and 6, sectioned images are retrieved by subtracting frames from 2 separate cameras, imaging separate sides of a spinning disk through different imaging arms. Although the imaging optics are identical in each arm, it is almost impossible to align them to exactly the same region on the disk (at the pixel level) and to ensure that they perfom identically with regards to aberrations, particularly distortion which creates large differences between the images. Although in a well aligned setup, differences between the cameras rarely exceed a few pixels (~ 10), this can seriously affect the final images the system is capable of producing, particularly in the case of chapter 6 where we expect an increased lateral resolution.

Our system does benefit from being able to project a calibration image onto the disk, allowing us to identify how the images are deformed from one another and facilitating the creation of a transform between them - particularly since this transform is fixed, and can be reapplied to each successive frame during acquisition.

4.1.3 *Requirements*

In order to recreate a suitable image via subtraction, there are certain requirements which must be met by any registration algorithm. Most importantly, it

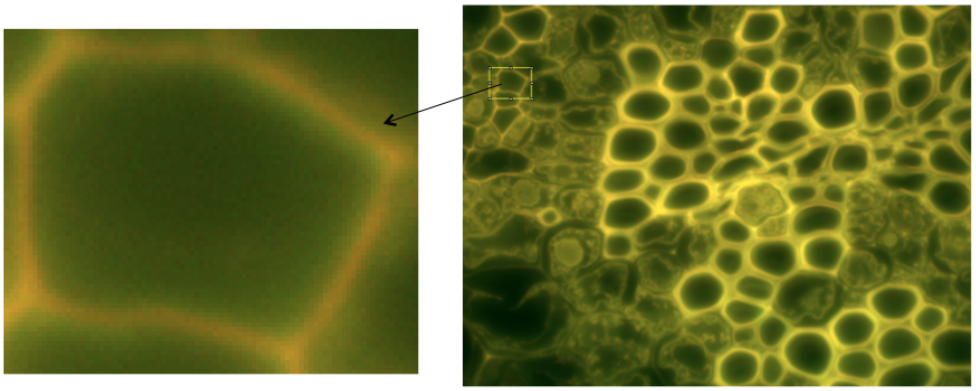


Figure 31: Zoomed region of image after affine transform registration. The orange halo in the left picture arises from subpixel misalignment.

must be capable of subpixel accuracy, as figure 31 shows. Without this, small objects often present with artefacts in the form of oversubtracted or undersubtracted halos.

As a first attempt, a global affine transform was implemented to deform one image to match the other. An affine transform is a geometrical transformation which is equivalent to transforming one triangle into another - it encapsulates rotation, stretching, and shearing. However, since the differences between the imaging arms are rarely uniform, this was generally unable to register the whole field but rather just a small subset.

The first functional algorithm designed used the calibration pattern projected onto the disk, matching points to each other in the resulting images. From these pairings, it could detect a translation for every calibration point, and then interpolate between those points for pixels between them. This brought to light an issue with the edges of the images: between the calibration points translations can be interpolated but outside these near the edge of the image translations could only be extrapolated. This was solved by using the nearest calibration points to the edges and extrapolating from differences between them. The major limiting factor of this algorithm, despite its high accuracy, was that it was very slow. Although it could handle 8 frames per second, the cameras used throughout this project ran at 16. Since one of the main ad-

vantages of wide-field microscopy is acquisition speed, we concluded a faster algorithm was necessary.

In order to design a high speed algorithm, we turn to processing the images on the graphics processing unit (GPU) contained within most modern computers.

4.2 OPENGL

The GPU is a special purpose processing unit designed for performing 2D and 3D rendering of images, particularly for computer games but also for computer assisted design and video processing. Its presence in computers has become more or less ubiquitous since operating systems have begun using graphical acceleration in their user interfaces. The GPU is a highly parallel processing unit - modern cards are often formed of dozens of cores, generally grouped in clusters which share certain caching features. Libraries such as CUDA and OpenCL allow it to be used for general purpose computing, where its highly parallel nature lends itself well to certain types of algorithm.

When used for drawing, the GPU is usually programmed using either Direct3D or OpenGL - the former being only available on the windows platform, while the latter is cross-platform. In most other respects, and particularly for our purposes, they are functionally identical: differences only become apparent when performing 3D rendering at a high level. For our purposes only 2D rendering is necessary, and working on an Apple Mac system OpenGL was chosen. At the time of writing, this project compiles against the latest version (4.4) of OpenGL. The minimum specification required is version 3.0.

The workflow when using a 3D rendering library is to first define a coordinate system: this determines the scaling and field of view that will ultimately be seen by the user. Working in 2D, a default coordinate system was chosen such that the edges of the screen correspond to x and y positions of +1 and -1. One can then draw polygons in this coordinate system, either colouring

them maually or relying on a texture, which is stretched or repeated accross the surface of the polygon according to where the vertices of the polygon correspond to coordinates within the texture. For example, drawing the full field of a camera would entail defining a rectangular polygon, then assigning each vertex of that polygon to a different corner of the texture. Drawing a triangular subset of the image would entail drawing a triangle, then assigning some 3 texture coordinates to each vertex of the triangle.

These features have been present since the first appearance of GPU's on the market. More advanced features such as vertex and pixel shaders have made an appearance in more recent years, allowing user-defined further processing to be done to vertex coordinates and pixel colouring after the drawing process has been defined. A vertex shader might be useful where one wanted to apply a time-varying effect to vertex coordinates, allowing shapes to morph in complex fashions without undue load on the CPU. The pixel shader can be used where one wants a time varying colour effect or wants a pixel coloured using a combination of different textures or colours.

Figure 32 shows the inputs and outputs of the vertex and pixel shaders. A vertex shader takes as input the vertex position and texture coordinates, and outputs those coordinates interpreted per-vertex, as well as a final vertex position. These coordinates are then fed into the pixel shader, interpolated accross the vertices of the current polygon, along with textures used to sample from. These output the final pixel colour as determined from calculation or image sampling.

4.3 IMPLEMENTATION

The registration process works in two steps: In the first stage, a transform is effectively calculated by identifying the differences between the images as encoded in a calibration pattern projected onto the disk and subsequently imaged onto the cameras. These points are then connected into a grid of tri-

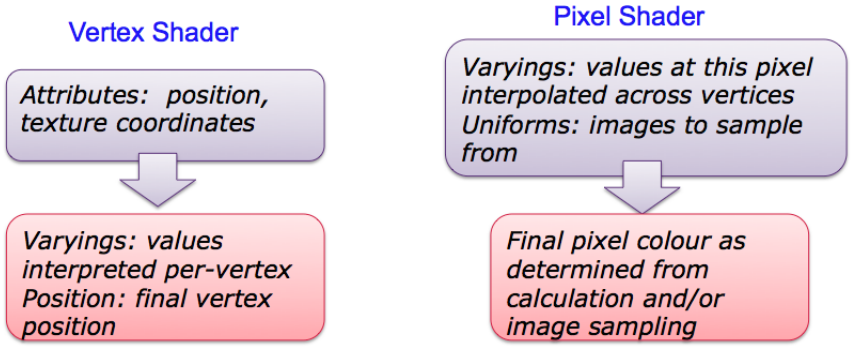
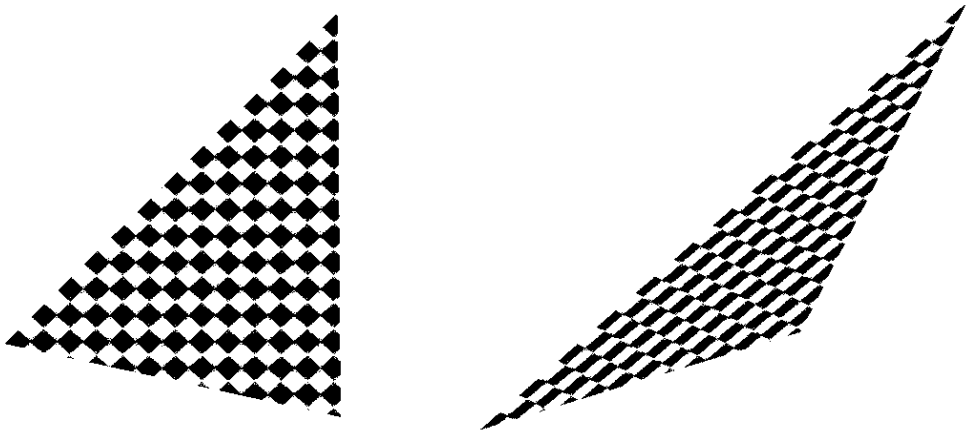


Figure 32: An illustration of the OpenGL shader pipeline.



(a) (b)

Figure 33: A triangle deformed through an affine transform by shifting the vertices.

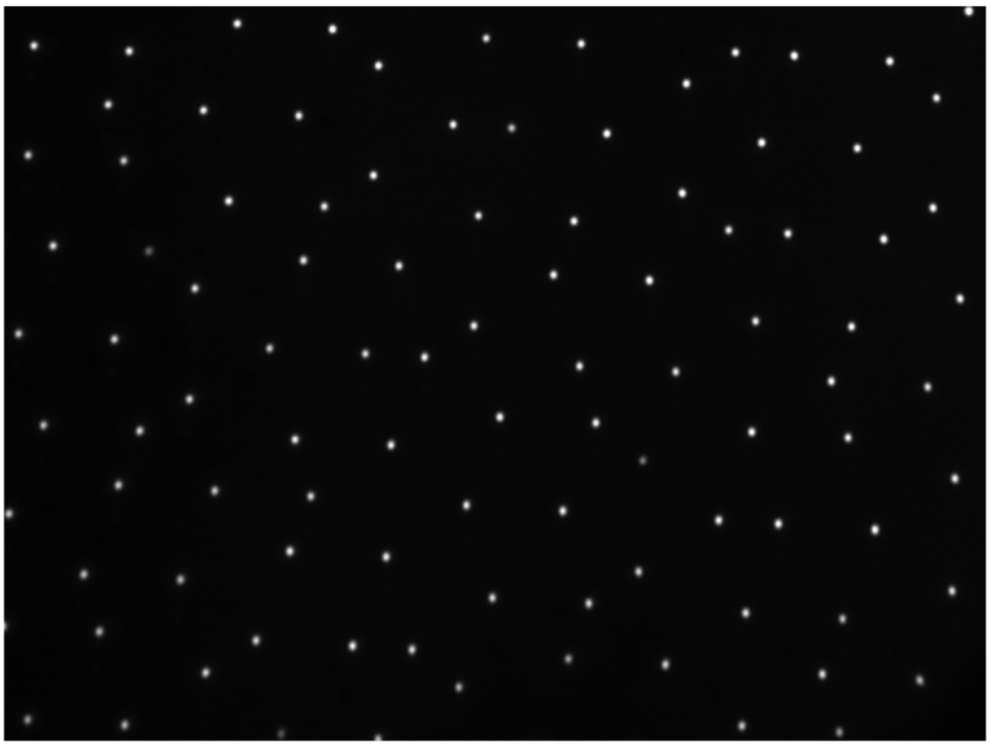


Figure 34: The calibration pattern projected onto the disk.

angles, which later forms the OpenGL primitives onto which the images are drawn. This is a one time process that can be performed upon startup before commencing an imaging session. In order to actually perform the registration, all that needs to be done is draw both images onto one set of triangles (generally the one generated from the transmitted disk image), passing the image coordinates along with the triangle vertices to OpenGL. Here we describe each of these steps in more detail.

4.3.1 *Calibration*

The first step in the registration process is calibration, whereby the grid of points projected on the disk is imaged onto both cameras. The grid of points consists of a Penrose tiling pattern (figure 34) , originally used due its non-repeatability, ensuring that a even severe misalignments can be recognised and corrected. In practice, this isn't actually necessary for our experimental

setup as differences in alignment typically don't exceed more than 10 to 20 pixels. The pattern is formed by 2 triangles of different dimensions, which tesselate to fill a large area. It is produced by projecting a mask, on which the pattern has been etched, onto the spinning disk.

Upon acquisition, the algorithm first identifies all of the points in both images by recognising areas of high intensity, and then calculating the barycentre of each point. Points in one image are then matched to points in the other by nearest-neighbor - bad matches can be discarded by limiting this matching process to a certain pixel distance depending on the magnification of the pattern. Points which fail to match can then be removed from both images.

Using this data, the algorithm can then recreate the grid of triangles which defines the Penrose pattern. This takes advantage of the fact that in the pattern, there are only 3 different line lengths present, and so by identifying these lengths between the points, a list of lines present in the image can be formed that only conform to the triangles we expect to see (ie. without crossing lines or missing lines). Reconstructing the triangles is then a simple process of identifying lines that share a vertex.

4.3.2 *Extension of Calibration Map*

Where a triangle cannot be formed - for instance, at the edge of the image where a vertex of the appropriate triangle is missing - the image cannot be drawn. Since one of the biggest advantages of this system is the large field of view, a system capable of extending the triangles past the field was designed. One potential way of fixing this would be to extrapolate the location of missing points and use these coordinates to draw the triangles, but in practice this is difficult because the Penrose pattern used in the calibration image does not repeat itself, making it difficult to find the origin of the pattern and thus simulate new points.

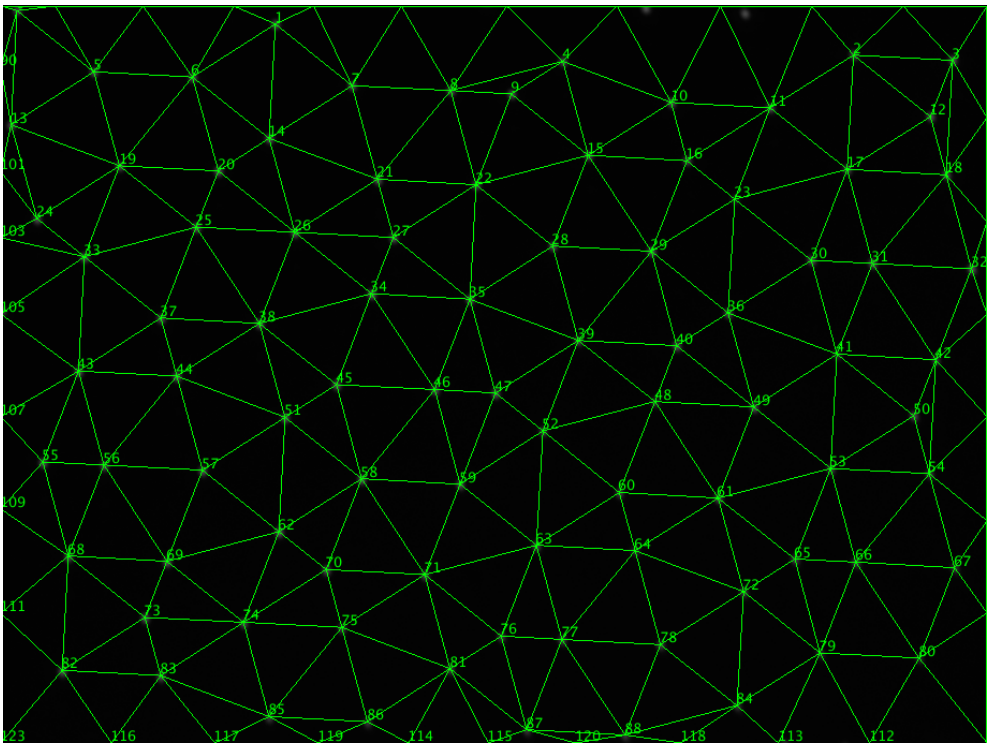


Figure 35: The full extended triangle map, covering the entire field of one camera.

The method to extend the triangle map used here functions by creating a new set of vertices along the borders of the fields, connecting these to the identified vertices and to each other. In the reflected image, these points are then moved by extrapolating from the affine transform experienced by the nearest triangle that was previously identified. Figure 35 illustrates a full triangle map covering the whole field.

4.3.3 *Drawing*

Once a map of triangles has been constructed for each image, all that remains to be done is to draw the images as textures onto the same triangle map, relying on OpenGL's built-in texturing engine to deform and bilinearly interpolate the textures between triangle vertices. In this fashion, the algorithm performs a tiled affine transform, one for each triangle in the map.

Rather than loop over all the triangles at every drawing event, which would happen at least as fast as the camera framerate of 16fps, a display list is created on the GPU post-calibration. This is a stored procedure which saves the drawing procedure (ie. the texture coordinates of every triangle vertex) on the GPU, allowing the operation to be recalled quickly and at vastly reduced cost to the CPU.

4.3.4 *Shaders*

The steps above illustrate how we can register both images by drawing one image onto the triangle map of the other image - in general the reflected image path is aligned to the transmitted one. Since the ultimate aim of the registration process is to produce frames we can subtract from each-other, the naive way to do this would be to draw both frames independently, save them to a location of memory, subtract them, and draw the final result. Thankfully, we can use OpenGL Shaders to perform all of these steps at once, as well as perform any flat-field corrections of the camera frames beforehand.

As described in section 4.2, the OpenGL pixel shader allows the user to specify how pixels are coloured onscreen. These shaders are programmed in GLSL, a C-like language; input values are passed to the shader prior to the drawing process and the output is simply the final pixel colour.

Here, the pixel shader is used to combine both images (at this stage in the process they are referred to as textures) via subtraction during the drawing process. It is also possible to pre-multiply the frame by a set amount (pre-gain) as well as to specify a final post-multiplier (gain). Gain values are typically in the region of 10-15, to account for the relatively small signal. An example of a subtraction shader is presented in algorithm 4.1.

Flat-field correction can be performed by taking dark (no illumination) and bright images (using a fluorescent sea slide) through the microscope, using these to calculate a pre-subtraction frame (which can account for bright pixels

Algorithm 4.1 A simple subtraction shader taking as input 2 textures and 2 parameters, and subtracting one texture from the other while applying gain.

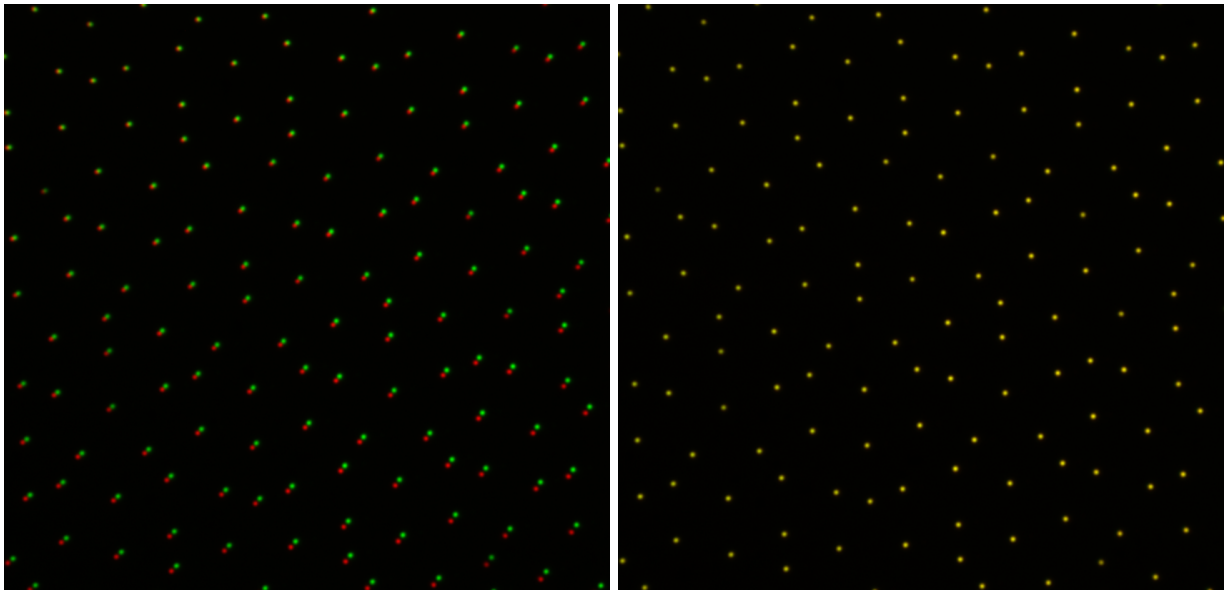
```
uniform sampler2D Texture0;
uniform sampler2D Texture1;
uniform float gain;
uniform float pregain;
void main()
{
vec4 texel = texture2D(Texture0, gl_TexCoord[0].st);
vec4 texel2 = texture2D(Texture1, gl_TexCoord[1].st);
vec4 vgain= vec4(gain,gain,gain,1.0);
vec4 vpregain= vec4(pregain,pregain,pregain,1.0);
gl_FragColor = vgain * (texel-(vpregain*texel2));
};
```

or light leakage) as well as a pre-multiplication frame (to account for variations of intensity accross the field). These frames are also passed as textures to the shader, which can then apply these steps before the subtraction process.

Using shaders, the entire drawing process is contained within the GPU. This is highly advantageous as the most taxing operation one can perform when working with GPU's is transferring data to or from the computer's main memory, particularly when working with uncompressed video. This ensures maximum efficiency and operating speed, all at minimal cost to the computer, allowing one to run other processes while also viewing or acquiring data.

4.3.5 *Framebuffers and 16bit operation*

Perhaps the most significant limitation using OpenGL for Scientific purposes is that, using an onscreen image buffer, image quality is limited to 8bits per colour channel - this makes sense, since barring professional artistic LCD panels, monitors are only capable of 8bit operation. This is a significant hurdle, since most scientific cameras (including ours) have 12 or 14bit ADCs and output at 16bit precision. Preserving this dynamic range, particularly before the subtraction process, is very important for further image analysis.



(a) Unregistered (b) Registered

Figure 36: Unregistered and registered calibration patterns overlaid in red/green.

Thankfully, OpenGL provides the facility to perform offscreen rendering into what is known as a framebuffer, essentially an offscreen image buffer which can be drawn to screen or saved directly to memory. Framebuffers can operate in several different bit depths, but among them are several 16bit per channel modes. The registration software is written to perform all operations offscreen into one of these framebuffers, only later drawing them to screen. When saving an image or image stack, the contents of the framebuffer are saved directly to disk, preserving the 16bit precision.

4.4 RESULTS

This algorithm is used in chapters 3 and 6, where (particularly in chapter 3) registration is seen to be accurate across the entire field of the camera (figure 36). Along with subtraction and flat-field correction, this is observed to function at the full frame rate of the cameras of 16 fps. Further profiling of the code using Xcode under Mac OSX shows that the main limiting factor on the side of the CPU is in uploading textures from system memory onto

the GPU. The GPU used in this experiment is a very modest GeForce G320M, built into the Mac Mini on which these experiments were performed.

Potentially, with high speed cameras and a fast interface, the algorithm could go very quickly. In order to test this, a single stored frame was uploaded to the GPU from memory repeatedly as fast as possible and registered: framerates over 200fps were observed. Again, the main bottleneck observed here is in the texture upload process from the system to the GPU.

If even faster framerates are required (for real time 3D imaging, for example), it is possible to eschew the texture upload process altogether. By leveraging the capability of modern motherboard interfaces, direct memory access (DMA) between an acquisition card and a GPU is now possible, allowing frames to be uploaded from the cameras straight onto the GPU memory. With a more powerful card, fixed transform registration could be possible at megahertz speeds.

4.5 CONCLUSION

In this chapter we have described the registration algorithm designed for real-time imaging from an Aperture Correlation Microscope. In this setup, images must be registered and subtracted from each other in order to yield a final, enhanced image, where differences between images are fixed over time and the same transform may be applied to all frames. A calibration routine is described which detects features within a projected pattern and pairs corresponding points on each camera. A grid of triangles is then constructed from these points on each field. The grid is then used as a canvas on which the images are drawn, taking advantage of a custom shader which subtracts them while performing flat field correction. The end result is a robust algorithm permitting real-time imaging at speeds of 16 frames per second on modest hardware, but potentially capable of much greater speeds on faster hardware.

5

REFLECTION CORRELATION MICROSCOPY

This section describes the construction of a reflection based spinning disk microscope, performed at the labs of Aurox ltd, as part of the CASE commitment of this project.

5.1 INTRODUCTION

Up until this point, we have mostly considered fluorescence microscopes as applied to biological imaging. However, in other fields such as materials science or semiconductor fabrication, samples are unsuited to fluorescence or transmitted light microscopy due to being opaque. In these applications, and where the use of optical microscopy permits, reflected light microscopes can provide the best solution for fast imaging of these samples.

In this chapter, an aperture correlation microscope constructed for the examination of these reflective samples is presented, where similar principles have been applied which allow one to create images with similar qualities as in the fluorescence setup. As previously, a disk etched with a line pattern is illuminated by an LED and projected into the sample plane, and reflected light is imaged back through the disk onto a camera.

Experimentally, there are a few important differences between this microscope and the one described in chapter 3. In this setup, the disk is placed perpendicular to the illumination and images are acquired by a single camera. Ultimately, the aim is to have a disk with two sectors, one etched with a pattern and one simply transparent. In this fashion, by synchronising the camera with the disk rotation, alternate widefield/structured illumination

frames are acquired; subtracting incoming frames from each-other without the need for registration yields sectioned images. Additionally, illumination and detection light are not separated here by wavelength, but by polarisation.

The reasoning behind having a flat disk is that the main application of this microscope is in semiconductor fabrication and assay, where having a flat field is important in order to be able to stitch together different fields of view. Additionally, this kind of setup is simpler to construct and more robust, especially given the industrial environment it would be applied in. UV illumination at $405nm$ results in higher resolution images than previous reflection correlation microscopes[21].

5.2 THEORY

5.2.1 *Reflection vs Fluorescence*

Although functionally, this microscope is very similar to the one in Chapter 3, there are a few important differences in this setup as compared to the previously seen one, both in terms of the detail of the experiment and also in terms of the theoretical performance.

Experimentally, the 2 main differences are that the disk is flat so that no return light reflected from the disk can be collected and imaged to a second camera, and that since this is a reflection microscope, polarisation is used to separate illumination from signal rather than differences in wavelength. The first entails that in order to recover enhanced images, conventional widefield frames must be subtracted from the structured ones: this is accomplished by removing a portion of the mask on the disk and imaging through a blank sector. The second means that illumination light is polarised linearly in one direction, while detection light must be polarised orthogonal to this: polarisers are used to filter light in this fashion, while a quarter wave plate placed near

the objective ensure that light polarisation returning from the microscope is orthogonal to that going in.

Imaging theory is also different in a reflection system, because illumination is not re-emitted by the sample and then imaged separately, but rather reflected from the sample's surface. In a fluorescence system, as seen in section 3.2.1, the optical transfer function that light experiences as a response to a thin sheet through focus, after a double pass through the objective is $\mathrm{OTF}(z)^2$. In a reflection system assuming only specular reflections (ie. the sample is a mirror), light is only reflected from the surface of the sample, and so does not experience the OTF of the objective a second time. Instead, it experiences the same OTF at twice the defocus, the distance light must travel from the objective to the sample and back again. Using this, and the same analysis as section 3.2.1, we can derive formulae for the axial response of this system.

5.2.2 *Axial Response*

As seen in section 3.2.1, the spatial frequencies returned from a fluorescence aperture correlation microscope and transmitted through the disk can be expressed as:

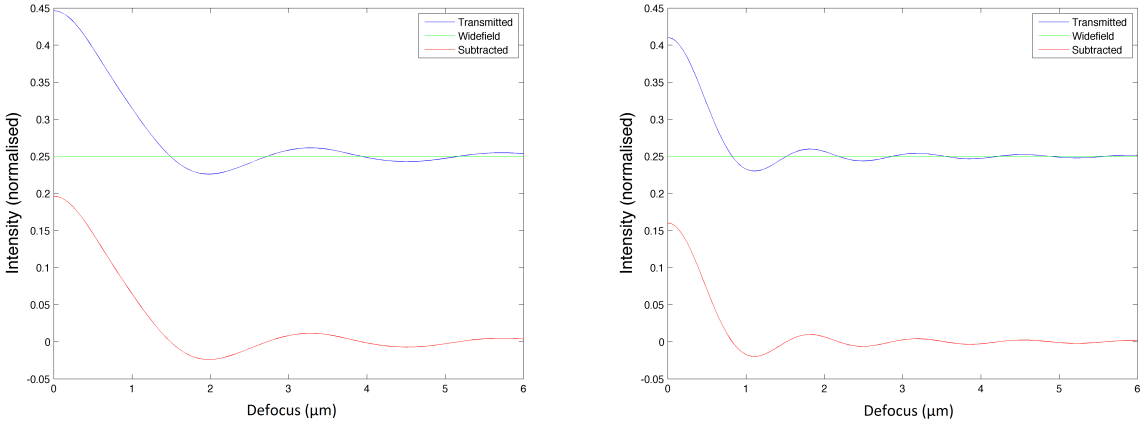
$$t(x,y,z) = h(x,y,z)\mathcal{F}^{-1}\left[OTF^*(u,v,z)F^*(u,v)F(u,v)\right] \tag{27}$$

However, assuming only specular reflections in this system, the collection PSF $h(x,y)$ no longer appears, while $OTF(u,v,z)$ is now replaced with $OTF(u,v,2z)$:

$$t(x,y,z) = \mathcal{F}^{-1}\left[OTF^*(u,v,2z)F^*(u,v)F(u,v)\right] \tag{28}$$

and similarly, integrating over radial coordinates we can derive the response to a mirror:

$$I_T = \int F(u,v)^2 OTF(2z)\,du\,dv \tag{29}$$



(a) 160μm disk pitch.

(b) 80μm disk pitch.

Figure 37: Plots of intensity vs defocus for different disk pitches.

In this system, a widefield image is subtracted from this rather than an image reflected from the back of the disk. The widefield image, having no sectioning property, is constant throughout the whole range of defocus.

These responses were modelled using Matlab, as well as the total intensity response $I = I_T - I_W$. Figure 37 shows these three modelled for disk pitches of both 160 and 80μm. Similarly to the fluorescent case, making the disk pitch smaller leads to a thinner axial response but degrades the signal from the microscope. Comparing these responses to the fluorescent ones, for the same pitch the axial response is greatly enhanced, since the pattern experiences the OTF at twice the defocus as in the fluorescent case. However, the side lobes are also more prominant here.

5.2.3 *Lateral Resolution*

Modelling the lateral resolution of this microscope is, however, not as straightforward as in the fluorescence case. Although the response to a thin sheet through focus is analogous to the fluorescent case with a different transfer function, the response to point like objects or steps is quite different. As an example, let us consider the case of the a step (figure 38):

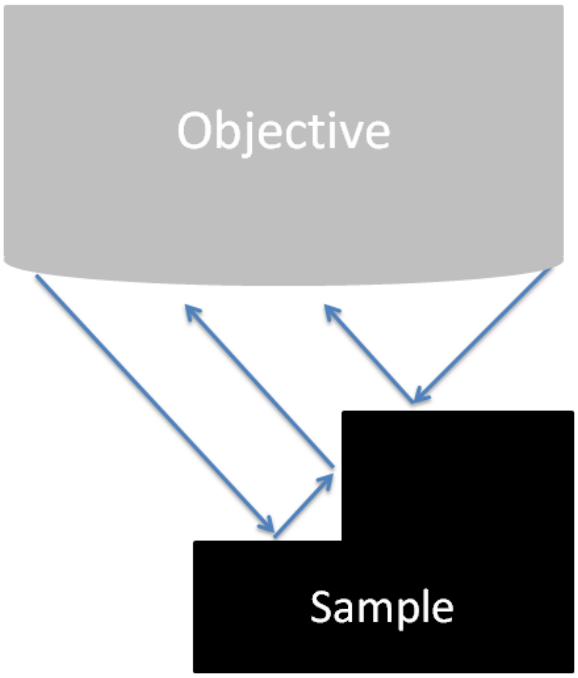


Figure 38: Diagram of incident light onto a step in a high NA reflection microscope.

In a fluorescence system, light incident on the sample would simply excite fluorescence which returns to the microscope; here the step causes complications with reflected light due to multiple scattering events. Reflections from the side of the step or from the bottom of the step then off the side, become significant. In addition, curved surfaces can act as lenses and result in re-imaging of the illumination pattern and resulting artefacts in the final image - although possible, modelling this effect would be very computationally intensive and likely require a ray tracing approach. In practice, this is also not a major issue, since the main attraction of this microscope is sectioning rather than resolution enhancement.

Another effect that can serve to add aberration to the images is diffraction, whereby small features in a sample can diffract incident light and cause large sidelobes to appear next to relatively small features.

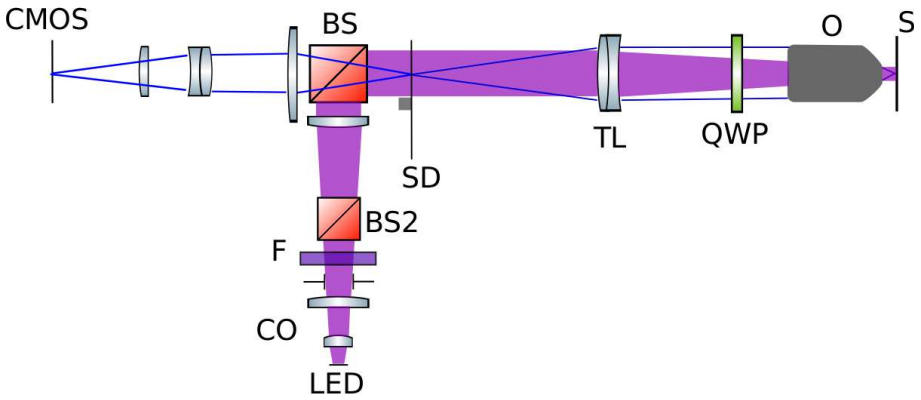


Figure 39: A schematic diagram of the reflection correlation microscope. The 405*nm* LED is collimated by a condenser assembly before being filtered by F and polarised through a beamsplitter BS2. It is then reflected through the disk by beamsplitter BS and enters the Objective O through the quarter waveplate QWP. Reflected light from the sample is rotated in polarisation by the double pass through QWP before passing through the disk and being imaged to the CMOS camera.

5.3 EXPERIMENT

5.3.1 *Imaging Setup*

A layout of the system is on figure 39. It is composed of the same imaging setup as previously in chapter 3, but optimised for operation at 405nm, the design wavelength of the microscope. In reflection mode, the illumination and imaging arms are split using a polarising beamsplitter. The illumination is polarised before hitting the beamsplitter by another polarising beamsplitter, which reflects illumination into the microscope. In place of a filter cube, a quarter waveplate is placed just behind the objective and used to ensure reflected light is rotated such that it becomes polarised at 90 degrees to the incident light. This light is then transmitted through the beamsplitter as well as a second polariser (to ensure minimal transmission of the unwanted polarisation) and imaged onto the camera.

5.3.1.1 *Illumination*

The illumination system consists of a UV LED (OCU-440 UE405-X-T) capable of producing 180mW of light at 400-405nm. A spectral analysis of the LED showed that it contains wavelengths from 350nm to 460nm, so a Semrock interference filter of 400/11 is used to narrow the bandwidth. This is necessary because the polarisers used are incapable of operation above 470nm, when they appear to act as a polariser perpendicular to the nominal axis. In the UV, the optics are also susceptible to a great deal of dispersion.

These polarisation optics are crucial components of the system, the reason being that if the illumination is not properly separated from the signal the camera quickly becomes saturated at longer exposures and the SNR of the system drops drastically. The UV polarisers chosen have an advertised extinction ratio of 10000:1 at the design wavelength, while the beamsplitter has a ratio of 1000:1.

The optical layout of the illumination system consists of a collector assembly formed by an aspheric 8*mm* condenser followed by a spherical 18*mm* lens (figure 40). A 60*mm* lens is placed after this in order to image the LED onto the the back aperture of the microscope objective (as this is a Kohler illumination setup). The magnification of the optics is set so that the LED fills the whole back aperture of the objective. An iris is also placed at the stop of the illumination system so that the size of the spot on the disk can be precisely controlled - although overfilling the disk will not adversely affect the imaging, it could cause additional reflection which would serve to degrade the SNR of the microscope. Being able to reduce the spot size also means that, using a small spot, the illumination optics can be aligned to the imaging optics more easily by centering the spot on the camera.

5.3.1.2 *Imaging*

The imaging system is a diffraction limited setup consisting of 5 elements in 4 groups, originally designed to image a tilted disk plane onto a tilted camera

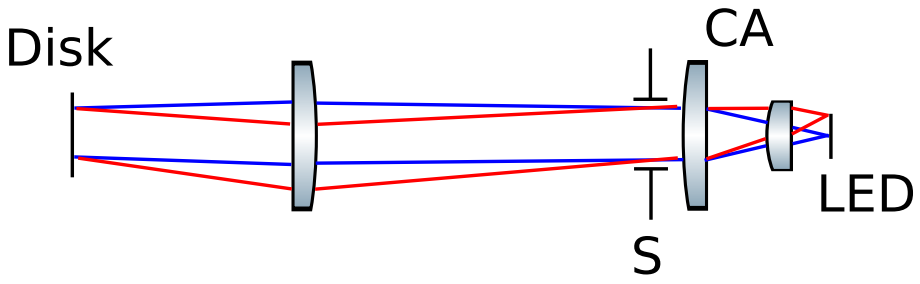


Figure 40: Optical layout of the illumination system. LED illumination is collimated by the collector assembly CA. The illumination stop S allows control of the illumination spot size at the sample plane.

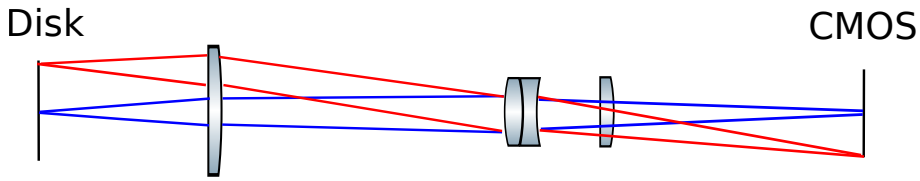


Figure 41: Optical layout of the Imaging system.

as in the setup in chapter 3 (figure 41)[106]. In order to tune the system for operation in the UV, the setup was optimised using Zemax and the 2 groups positioned close together (the prototyped optical components in the setup) were brought slightly closer together. Figure 42 shows the resulting Strehl ratio against the field at the design wavelength range of 390-420, which is in line with the illumination wavelength and filter.

The camera used in this setup is a Ximea MQ042MG-CM CMOS, which has a maximum resolution of 2048x2048, a pixel size of 5.5 x 5.5µm, as well as a high framerate of 90fps. The relatively large field size and framerate allow it to capture stacks rapidly, which ties in well with the application of this setup as a potential tool for performing assays on large semiconductor plates.

5.3.1.3 *Objectives*

The system was tested on a Zeiss Observer.Z1 microscope, but unfortunately at first no UV specific lenses were available to test with so 2 VIS objectives were used instead - a 20x 0.5 NA and a 63x 1.4 oil immersion objective. Both of these objectives are $\sim$ 10% transmissive at 405nm, resulting in a rather poor signal ($\sim$ 1%) and long exposure times had to be used. In later measurements,

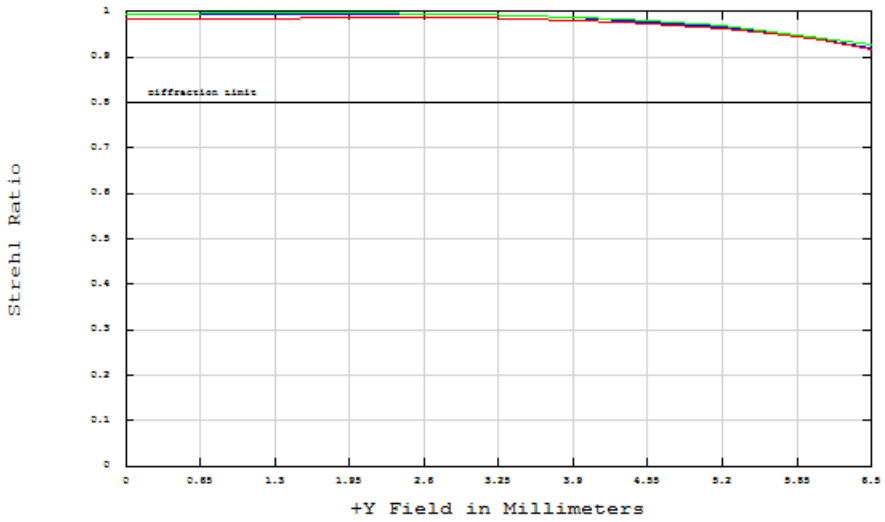


Figure 42: Strehl ratio of the imaging system, diffraction limited for the 3 design wavelengths of 390, 405 and 420.

Objective	Resolution at image plane	Nyquist sampling
20x 0.5NA	8.1µm	4.05µm
63x 1.4NA	9.1µm	4.55µm
50x 0.95NA	10.7µm	5.33µm

Table 2: Sampling rates for the 3 objectives used.

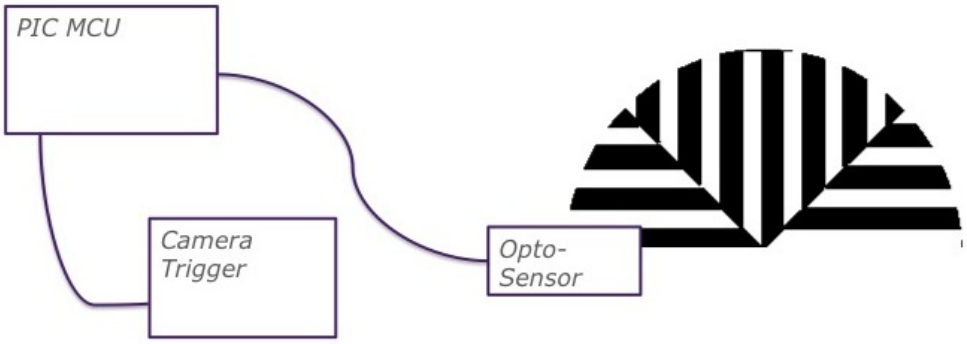


Figure 43: A diagram of the setup used to synchronise camera acquisition to disk rotation.

a Zeiss 50x 0.95NA EpiPlanApo objective suitable for UV imaging was used, with high transmissivity ($>$ 80%) at the design wavelength and thus much stronger signals were observed. From the objective specifications, we can also determine the required sampling rates from the camera. In table 2, we can see that with the 5.5µm pixel size from the camera used, the resulting images will be slightly undersampled. This would be an issue when observing very fine detail close to the lateral resolution limit of the microscope, but in practice we are most interested in the axial resolution enhancement achieved here.

5.3.2 *Acquisition synchronisation*

Because of the non-tilted disk used in this setup, the single disk used has separate regions for structured and widefield acquisition (potentially different pitches of lines could be etched onto different portions of the disk). This means that in order to acquire a structured illumination frame or a widefield frame, the acquisition must be synchronised to the rotation of the disk, which is at a constant 50Hz (or 3000rpm). The disk used in this experiment is the same configuration as that used in Chapter 3 (ie. an 80µm sector and 160µm sector), where one half of disk has had the etched pattern removed through an acid bath.

An optosensor was placed over the disk and plugged into the driver board of the microscope (figure 43). The gain circuit for the optosensor was set such that it triggered a logic pin on the driver board on a change of region on the disk; code was then written such a trigger signal could be sent from the board to the camera. A button on the logic board was then programmed which allowed one to set a delay between receiving the optosensor trigger and sending the trigger signal to the camera. By triggering on the appearance of the etched sector of the disk a structured frame could be taken, while pressing the button the board delayed the trigger output and allowed the camera to acquire a widefield image through the blank disk sector. Image stacks could then be acquired by taking a stack of structured frames followed by a stack of widefield ones. In the future, a more sophisticated disk design could have several different sectors for different pattern types, although any line etched sector must be imaged for at least 90 degrees of disk rotation to allow the lines to average over 90 degrees. Live imaging could also be accomplished quite easily by acquiring alternating structured and widefield frames and modifying the viewer software to perform the subtraction in real time from alternating input frames; a high speed camera is particularly relevant for this application.

5.4 RESULTS AND DISCUSSION

5.4.0.1 *Reflection Suppression*

As previously mentioned, perhaps the most important measurement in the system is quantifying the amount of disk reflection suppression. The most conceptually simple way to do this would be to compare the image intensity between placing a mirror at the focus or having no sample, but in practice this also takes into account reflection/poor transmission from the microscope optics. Instead, a quarter waveplate was placed just before the disk, and ro-

tated between positions which observe or filter the disk reflection. This was performed using both a camera and a spectrometer at the image plane.

The results of this test show that the suppression ratio (ie. the ratio of intensity between both waveplate positions) is about 1000:1, confirmed using both detection apparatus. This is sufficient for short exposures, but where long exposure times need to be used could cause issues. With this in mind, new disks were ordered which are coated with a layer of black chrome - an absorptive chrome plating often used in the construction of Photovoltaic (PV) cells[108, 107]. Experiments have shown these coatings to be less than 1% reflective at the design wavelength, while the glass used in the disk appears to be $\sim$ 8% reflective. With the coating, the disk has another order of magnitude of reflection suppression, becoming approximately 10000:1, again confirmed using both detection apparatus.

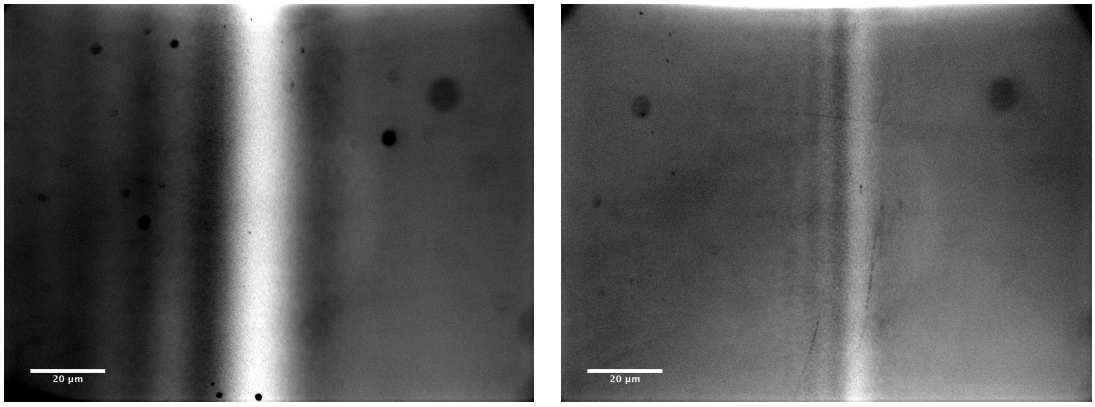
5.4.0.2 *Axial resolution*

The axial resolution of the microscope was tested using what is known as the mirror test, whereby a mirror is placed at the focus of the microscope at a small angle ($\sim$ 10 degrees). The resulting images show a bright central line at the focal plane, and smaller side lobes at regular intervals - these side lobes are a natural consequence of optical sectioning. Interestingly, the lobes are more visible to one side (closer to the objective) than the other - this is likely due to spherical aberration, which is asymmetric about the focal plane. The width of the central line corresponds to the axial resolution of the microscope, as taken using the 63x 1.4NA oil immersion objective.

Images were taken at 3 different focus positions, in order to acquire a transformation between the x and y pixel coordinates and the z coordinate, by recording the z translation of the microscope at each position and measuring the corresponding translation of the central line. Measurements were taken for the line at either end of the field as well as in the middle of the field. These measurements were repeated at 4 different grid pitches, using 2 disks: 160µm

Grid Pitch	Theory	Experiment
$160\mu m$	$0.9\mu m$	$0.91 \pm 0.03\mu m$
$80\mu m$	$0.45\mu m$	$0.44 \pm 0.03\mu m$
$40\mu m$	$0.28\mu m$	$0.31 \pm 0.04\mu m$
$20\mu m$	$0.18\mu m$	$0.23 \pm 0.04\mu m$

Table 3: Axial resolution as measured by the mirror test compared with simulation.



(a) $80\mu m$ pitch. (b) $20\mu m$ pitch.

Figure 44: Images acquired during the mirror test, for 2 different grid pitches. Left to right corresponds to $+z$. Black spots are from dust on the sample. 63x 1.4NA.

and 80µm, and 40µm and 20µm. Finally, the width of the central line was extracted, scaled depending on the transformation calculated previously, and compared with predictions from a Matlab simulation code based on equation 29.

The results of the test are seen in Table 3, where it can be seen that they line up very well with predictions from the software, although at small grid pitches there is a small mismatch. As seen on figure 44, the SNR of this measurement is quite low as a result of the low transmissivity objectives and long exposure times used, which could be the source of this error.

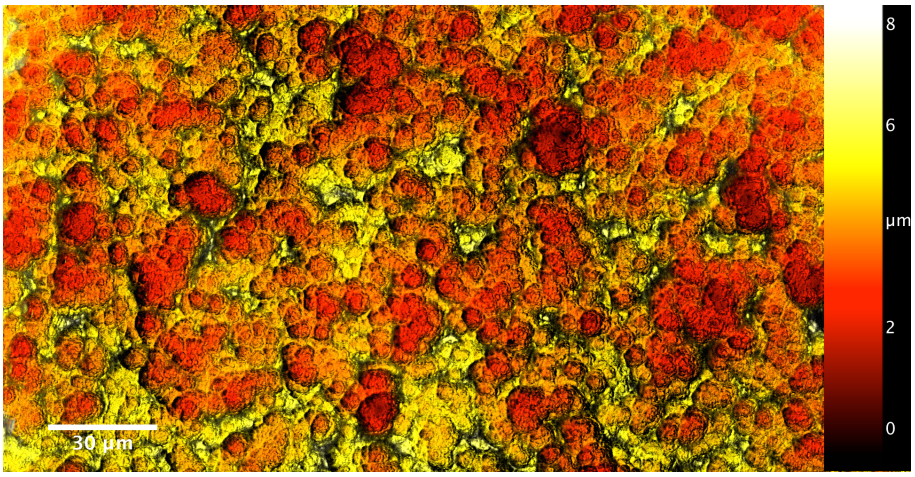


Figure 45: Maximum intensity projection of the fractal black anti-reflection coating taken on the 80µm disk sector. 50x 0.95NA

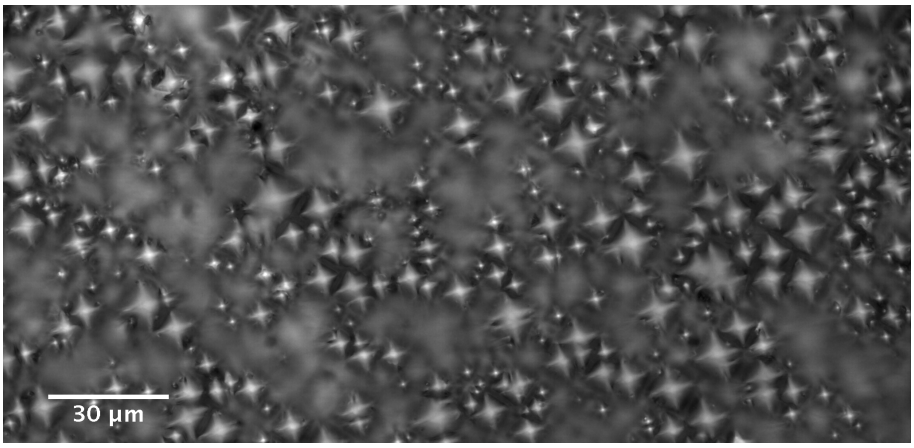
5.4.0.3 *Image Stacks*

The final experiment performed with this setup was to take several image stacks and construct 3D models of the surfaces examined. The 3 types of sample used are a PV cell, a transistor chip, and an anti-reflection coating. These stacks were acquired using the 50x 0.95NA Zeiss objective, which as compared to the previous experiment allowed for much faster exposure times. This is clearly evidenced in the 3D maximum intensity projection of a broad-band anti-reflection coating with 2% reflectance across the sample (fractal black [119]) in figure 45.

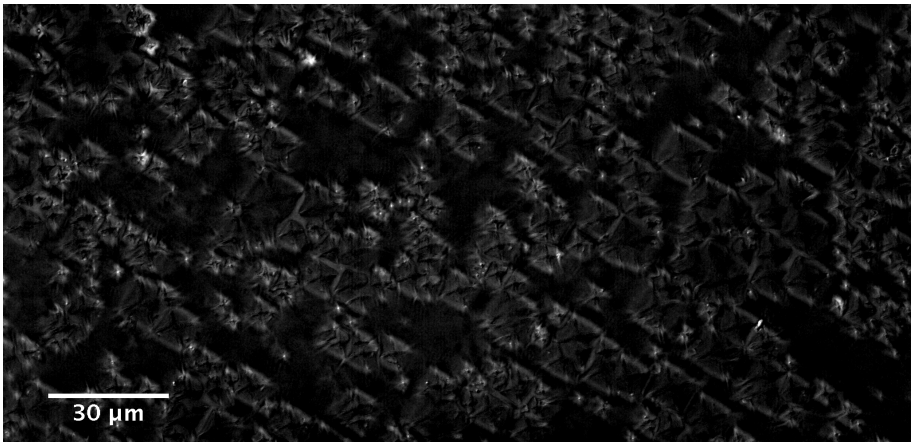
In the PV cell sample (figure 46), the structure of the cell is clearly visible: it is formed of a cluster of pyramid shapes. These shapes are present in order to improve light collection efficiency of the cell, the angle of the pyramids having been chosen to maximise the number of bounces incident photons make on the surface of the cell [120]. This stack is composed of 330 images, each 2048x2048 pixels (cropped down to a region of interest of 1024x2048), an entire stack taking roughly 20 seconds to acquire (two stacks are acquired: widefield and structured).

In figure 47, images of the transistor sample are shown. Perhaps the most interesting aspect of these stacks is that we can observe here the ability of the

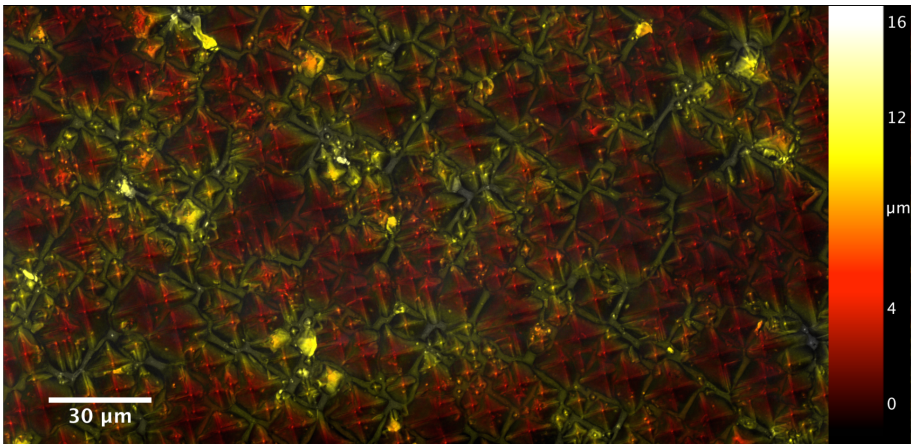
microscope to image into certain types of sample. Semiconductor samples such as this one are often coated in layer of silicon dioxide film which serves to protect the surface of the chip from damage [121]. In many other materiel configurations such as stylus or electron microscopes, resolving into a layer such as this is impossible, however using a sectioning optical technique we can clearly resolve 2 layers on this sample (figure 48). It would appear from the graph that this oxide layer is approximately 2µm in thickness - this is well within the range of films used in semiconductor fabrication ($1 - 10\mu m$). The sharpness of the response is also clearly different on either side of the graph: this can be explained considering that silicon dioxide has a refractive index of 1.46. Imaging beyond this film will be affected by a change in axial magnification as a result of the mismatch between the film refractive index and air, since the axial magnification is expressed in terms of the lateral magnification as $\frac{M^2}{n}$. 3D reconstructions of both image stacks can be found in figure 49.



(a) Widefield

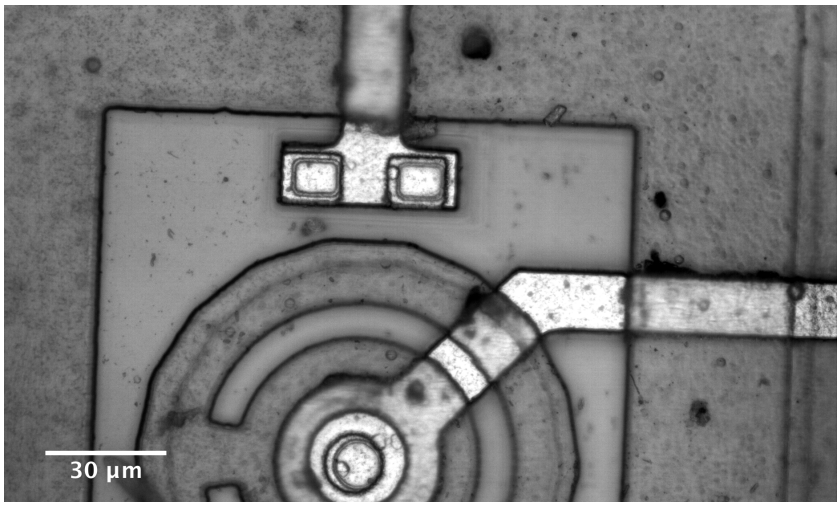


(b) Sectioned

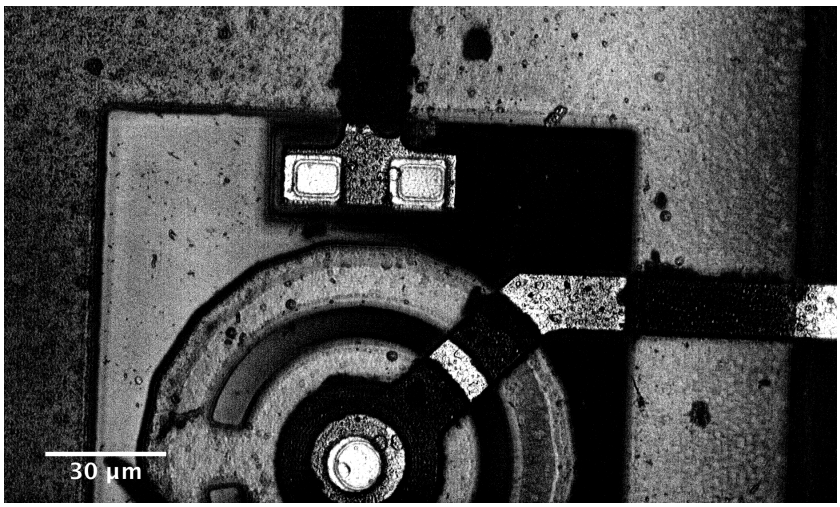


(c) Maximum intensity projection.

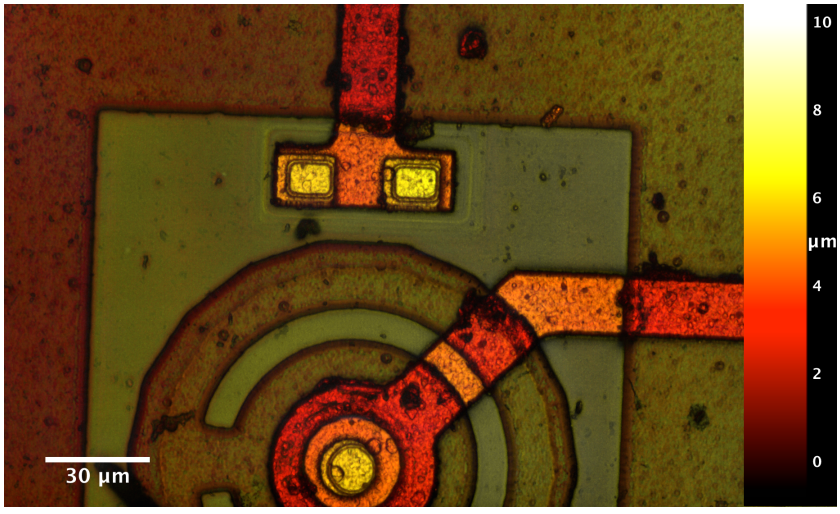
Figure 46: Sample images from a stack taken of a PV cell with the 80µm disk sector. 50x 0.95NA



(a) Widefield



(b) Sectioned



(c) Maximum intensity projection.

Figure 47: Sample images from a stack taken of a transistor chip with the 80µm disk sector. 50x 0.95NA

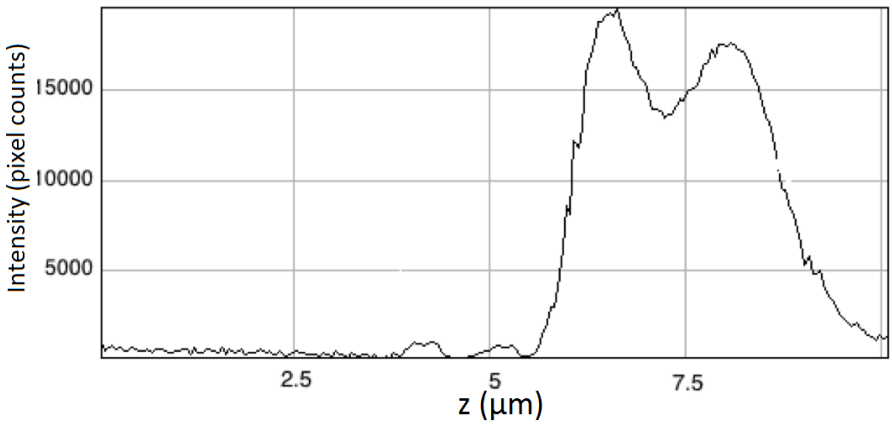
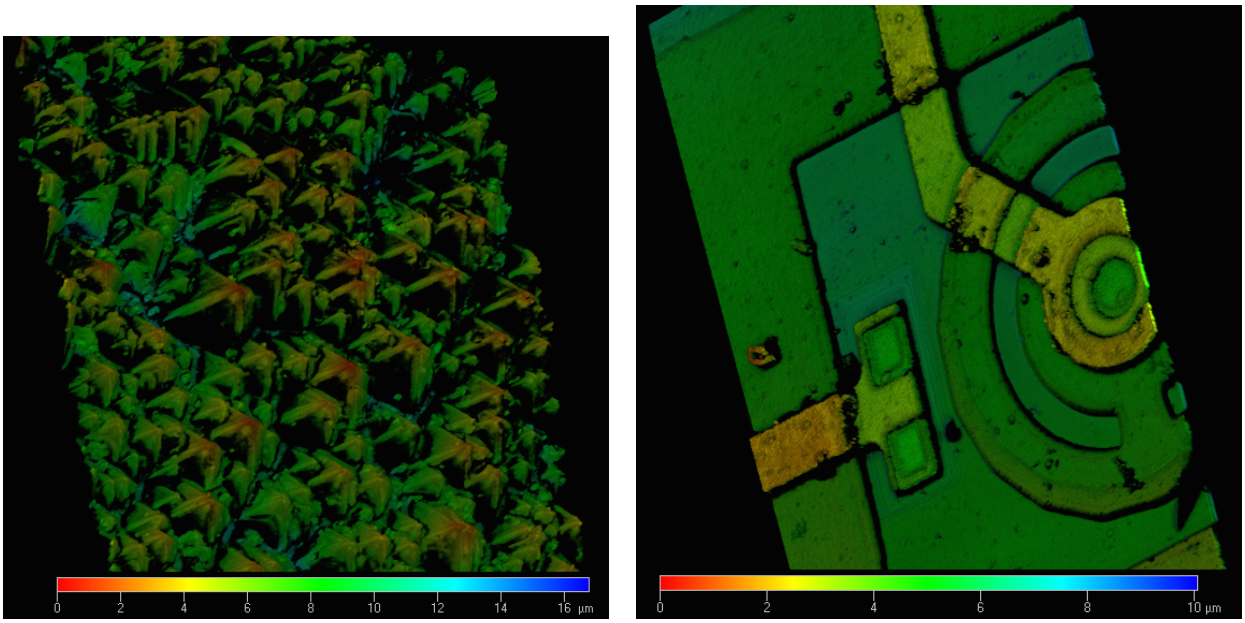


Figure 48: Z projection of a region on the transistor sample, illustrating the ability to depth resolve coatings.



(a) (b)

Figure 49: PV cell (a) and transistor chip (b) 3D reconstructions.

5.5 CONCLUSION

In this chapter we have introduced an aperture correlation microscope being used in reflection rather that in fluorescence. While reflection correlation microscopes have been built before [21], this microscope can observe finer detail

than previous aperture correlation systems through illumination in the UV. A method for synchronising camera acquisition to the rotation of the spinning disk allows for widefield and aperture correlation images to be taken from the same setup, so that such a microscope has applications in place of a scanning electron microscope or stylus microscope where fast imaging with high contrast is necessary. The operating theory of the microscope was briefly presented, before describing the experimental setup and equipment choices. Finally, results are presented as measurements of the axial resolution and several sets of image renders of different samples.

6

SUPER-RESOLUTION APERTURE CORRELATION MICROSCOPY

6.1 INTRODUCTION

The techniques I have described up until this point have been mostly conceived as methods to provide optical sectioning for fast, wide-field imaging. In this section, we introduce a novel type of microscope based on the previous approaches, but attempting to provide enhanced lateral resolution of twice the diffraction limit and optical sectioning as well as fast, highly light efficient wide-field imaging. Other techniques purporting to provide this kind of resolution enhancement (ISM [90, 86]), are typically not wide-field techniques, or rely on a fast scanning setup (multifocal ISM [93]). These approaches, requiring scanning steps or long computation time, can be unsuitable for imaging moving samples. By contrast, our aperture correlation based approach is single-shot, recovering a sectioned image after a simple image subtraction which can be done in real-time.

Our technique came about after a patent application filed by Olympus [122] suggesting devices appearing strongly influenced by aperture correlation. Amongst the many devices proposed in the patent, there were suggestions of using coherent illumination at the same time as increasing the mark:space ratio of the pattern, and that this would somehow improve the lateral resolution of the resulting microscope. As we will see later, this is supported by theory we have developed for our invention. At the time, we were investigating the possibility of using carefully tailored spinning disk masks to improve the signal from a standard aperture correlation microscope and possibly get

some limited (mostly axial) resolution enhancement over a standard aperture correlation microscope.

By combining laser illumination and our methodology for creating new disk patterns through a holography based approach, a new idea for providing super-resolution in an aperture correlation microscope was put together. When using coherent illumination near the edge of the microscope pupil, one would generally expect to be able to get resolution enhancement of up to 1.5 times better than a widefield microscope, since the spatial frequencies present in the mask used to generate the structured illumination would be placed correspondingly to the edge of the pupil. Because fluorescence responds to the intensity of the illumination however, terms appear in the return fluorescence which are twice the frequency of that corresponding to the edge of the pupil. If we were to introduce these new frequencies into the mask, correlated to the ones used to generate the illumination pattern, we could use these to enhance return fluorescence.

We present in this chapter the operating theory of this microscope, as well as the aperture mask design strategy we have used to create the new masks. A version of this microscope constructed in the lab is then presented, along with some results validating this approach.

6.2 THEORY

In this section coherent and incoherent imaging is introduced in the context of the aperture correlation microscope, before a discussion on the differences between both regimes, particularly with regard to the maximum resolvable frequency in either illumination type. The novel use of correlating aperture mask spatial frequencies, as applied to this setup, is then introduced and some new mask designs are analytically examined for their expected characteristics.

Here we recall the theory from Chapter 3, whereby the transmitted and reflected PSFs can be defined as:

$$t(x,y) = h(x,y)\mathcal{F}^{-1}\left[G^*(u,v)F(u,v)\right] \tag{30}$$

$$r(x,y) = h(x,y)G^*(0,0) - h(x,y)\mathcal{F}^{-1}\left[G^*(u,v)F(u,v)\right] \tag{31}$$

Recalling the collection PSF $h(x,y)$, the illumination $g(x,y)$, the mask $f(x,y)$ and their fourier transforms $G(u,v)$ and $F(u,v)$. Previously, we used the expression for the illumination at the sample plane given by the use of the OTF; if we were to use coherent illumination, however, $g(x,y)$ becomes:

$$g(x,y) = \left|\mathcal{F}^{-1}\left[P(u,v) \times F(u,v)\right]\right|^2 \tag{32}$$

Since the illumination at the pupil plane is the fourier transform of the mask; at the sample plane this then becomes the fourier transform of the mask times the pupil function of the objective, inverse fourier transformed. The final subtracted image can be written as:

$$w(x,y) = t(x,y) - r(x,y) = 2h(x,y)\mathcal{F}^{-1}\left[G^*(u,v)F(u,v)\right] - h(x,y)dc\left[g(x,y)\right] \tag{33}$$

6.2.1 *Mask Frequencies and Resolution*

For both types of illumination (coherent or incoherent), the resultant pattern in the sample plane depends on the Fourier transform of the aperture mask, in this case the spinning disk. A line mask like that used in chapter 3, when Fourier transformed, results in 2 strong peaks either side of zero, corresponding to the fundamental frequency of the grid. Higher frequencies are also generated with rapidly declining power. We could think of other kinds of

masks too: squares or other more sophisticated arrangements of peaks in frequency space.

Let us consider the frequency content of the final image by Fourier transforming equation 23:

$$W(u,v) = OTF(u,v) \otimes \Big(OTF(u,v) F^2(u,v) \Big) - \mathcal{F}\left[h(x,y) dc[f(x,y)] \right] \quad (34)$$

Where the first term contains information supplementary to a conventional imaging system. We see that ultimately, the frequency content of the final image is determined by the convolution of the $OTF(u,v)$ with the square of the mask's Fourier transform modulated by the same OTF. In effect, what this means is that a conventional transfer function is in some sense replicated several times, centred over every peak in the mask's Fourier transform. We might then expect that controlling the appearance of these peaks in Fourier space may allow us to better fill the region of support of the objective.

6.2.2 *Frequency Limits in Incoherent and Coherent Imaging*

In the incoherent case, the collection PSF $h(x,y)$ and the $OTF(u,v)$ are both limited to a maximum spatial frequency content of $2\nu_0$. As the final response multiplies the collection PSF $h(x,y)$ and the inverse Fourier transform of the $OTF(u,v)$, in frequency space the convolution of these two means that the maximum spatial frequency throughput of the system is $4\nu_0$, however this would entail a mask with frequency components at the cut off of $2\nu_0$, resulting in effectively zero signal. Choosing a mask with a more realistic frequency of ν_0 means that the effective cut-off is around $3\nu_0$, or roughly the same as confocal microscopy. Although a mask like a grid can have more than one spatial frequency, in particular at integer multiples of the fundamental, these generally have little effect due to the square in $F(u,v)$ which appears in equation 23.



Figure 50: Frequency components in a line mask, with A, B and C being the zeroth, first and a second orders respectively.

When imaging coherently, $h(x, y)$ is still limited in the same way, but now the $OTF(u, v)$ does not appear in the equation. Instead, $G(u, v)$ is limited to a maximum spatial frequency content of 2, since the pupil $P(u, v)$ has a maximum extent of 1. Since $G(u, v)$ is derived from $f(x, y)$ we might expect that only frequency components smaller than ν_0 can contribute to $G(u, v)$. However, since these calculations are done in amplitude, squaring to intensity means that frequencies up to $2\nu_0$ do appear in the sample plane and can be greater than in the incoherent case. If $f(x, y)$ only had spatial frequencies smaller than ν_0 this would imply a maximum frequency limit of $3\nu_0$ as in the incoherent case.

6.2.3 *Our novel approach*

As we have just considered, using a mask with a frequency at ν_0 with coherent illumination, we can expect a maximum frequency resolution of $3\nu_0$. However, if we consider a mask $f(x, y)$ with frequencies at both ν_0 and $2\nu_0$, we could in fact achieve a resolution of up to $4\nu_0$. A frequency of ν_0, after squaring to intensity, would lead to frequencies up to $2\nu_0$. If the mask contains frequencies at $2\nu_0$ then after detection we could expect these to be relatively enhanced rather than nulled, filling the region of support better than confocal microscopy. In order for maximal enhancement at higher spatial frequencies, we could weight these second orders more than the first ones; we would also require the orders in the mask and also in the illumination to be real and positive.

As an example, let us consider a line mask with an arrangement of spatial frequencies as in figure 50. Assuming only the zeroth and first orders get past the system pupil and reach the illumination plane, we can write $g(x, y)$ as:

$$g(x, y) = |A + 2B \cos kx|^2 \tag{35}$$

which if we expand:

$$g(x, y) = A^2 + 2B^2 + 4AB \cos kx + 2B^2 \cos 2kx \tag{36}$$

where we now see the appearance of the second order, and the potential to correlate this with the second order in the mask, C. We also see the appearance of extra terms in the zero order as well as the first order recreated as a cross-term of A and B. Although this is a useful insight, this doesn't tell us anything about the 3D transfer function of the microscope, and this result could be misleading having missed out on this information. If we wish to calculate the full 3D transfer function, we can use the fact that:

$$k_0^2 = k_x^2 + k_y^2 + k_z^2 \tag{37}$$

and the first orders having the lateral spatial frequency $k = k_x$ we can then write their axial spatial frequency:

$$k_z = \sqrt{k_0^2 - k^2} \tag{38}$$

Assuming again that only the zeroth and first order pass through the pupil of the microscope, we write:

$$g(x, y, z) = \left| Ae^{ik_0 z} + Be^{ik_z z} \left(e^{ikx} + e^{-ikx} \right) \right|^2 \tag{39}$$

Expanding this out as previously:

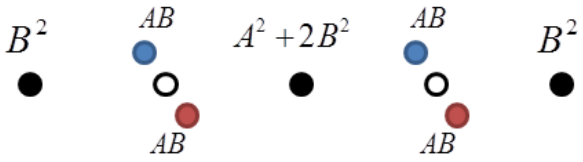


Figure 51: Frequency components in the illumination plane, after squaring from amplitude to intensity. The red and blue dots represent frequencies present at $k_z \neq 0$.

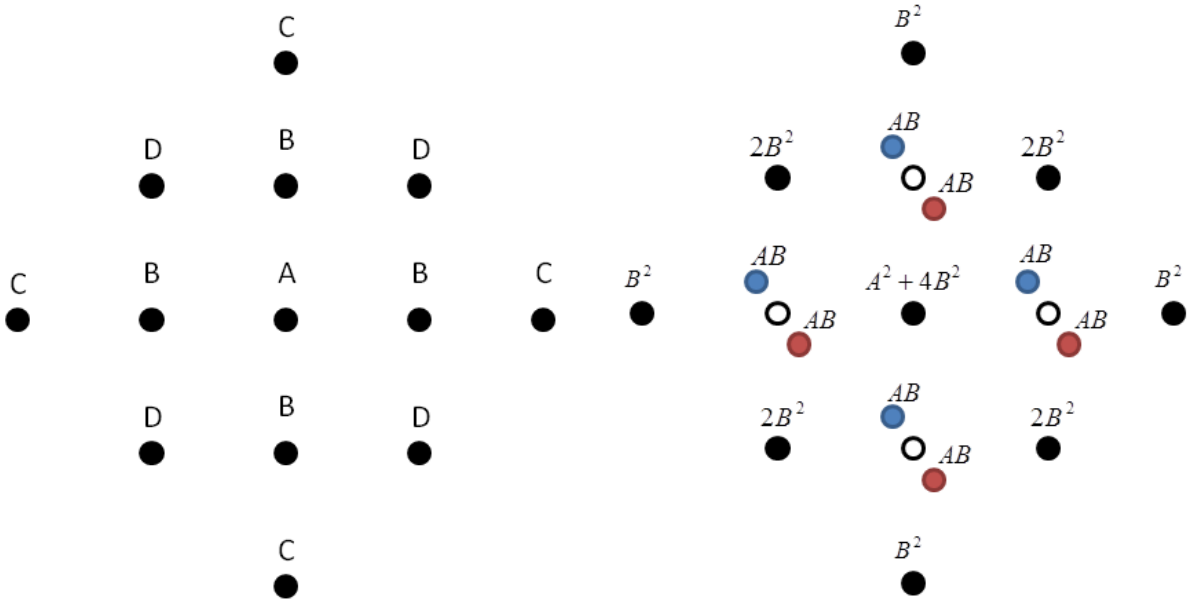
$$\begin{aligned} g(x,y,z) &= A^2 + 2B^2 + ABe^{i(k_0 z - k_z z)}\left(e^{ikx} + e^{-ikx}\right) \\ &\quad + ABe^{-i(k_0 z - k_z z)}\left(e^{ikx} + e^{-ikx}\right) + B^2\left(e^{2ikx} + e^{-2ikx}\right) \end{aligned}$$

The zeroth order and second order terms appear the same as before, however we can see now the first order only appears at $k_z = k_0 - \sqrt{k_0^2 - k^2}$ and $k_z = \sqrt{k_0^2 - k^2} - k_0$. In figure 51 the generated orders and their positions are shown. In the case of the frequencies at $k_z \neq 0$, we postulate that the detection mask, existing only at the detector plane, has the same frequency components for all values of axial spatial frequency. Working out the full 3D transfer function can now be done by multiplying this result with the mask frequencies and then convolving the result with the incoherent OTF.

There are now 2 ways of (relatively) enhancing the signal in the higher spatial frequencies available: either put more power into the higher order C, or reduce the power in the zeroth order (A). Reducing the power in A by constructing a non 1:1 mask would be undesirable, since it would reduce the light efficiency of the microscope. Another way of achieving this in practice is to attenuate the power in the zeroth order before the illumination plane, by placing a point mask in the objective. In this fashion, we can make the illumination mask depend on an attenuated zeroth order A' rather than A. It cannot be completely attenuated as a loss of all power in A' would also imply a loss of optical sectioning, since the AB modes would become zero.

The previously mentioned Olympus patent appears to make make use of this same effect to enhance higher spatial frequency content in their resulting images. They suggest a device similar in layout to an aperture correlation microscope, but with coherent illumination employed instead of the usual incoherent illumination. While the masks that they use are very similar to the straight line masks we employ in chapters 3 and 5, the first orders in the fourier transform of these masks are placed at the edge of the microscope pupil as we have have described here. The key difference to the masks used by normal aperture correlation microscopes is that the mark:space ratio is reduced so that the transmissive lines on the disk are thinner than the reflective lines. This is, in fact, a very simple way to generate second orders in the spatial frequency content of the mask, although it does reduce the light budget of the microscope. Since the square wave function which defines normal masks is odd, one would normally only generate odd diffractive orders, but reducing the mark-space ratio means that the function is no longer odd and so we would expect even orders to appear in its fourier transform. Olympus claims resolution enhancement on the order to SIM microscopy, or up to twice the conventional limit.

In the next sections we will examine the use of other arrangements of mask orders in frequency space, and eventually discuss the optimisation process through which we can generate masks with an equal mark:space ratio while tailoring the power diffracted into each spatial frequency component. This is perhaps the most important development here over the proposed Olympus systems: by generating masks in this way, we can not only maximise the light budget but also experiment with different arrangements of spatial frequencies.



(a) Mask components.

(b) Illumination components.

Figure 52: Frequency components in a quad mask, with A, B and C being the zeroth, first and a second orders respectively. D arises from cross-terms between B orders.

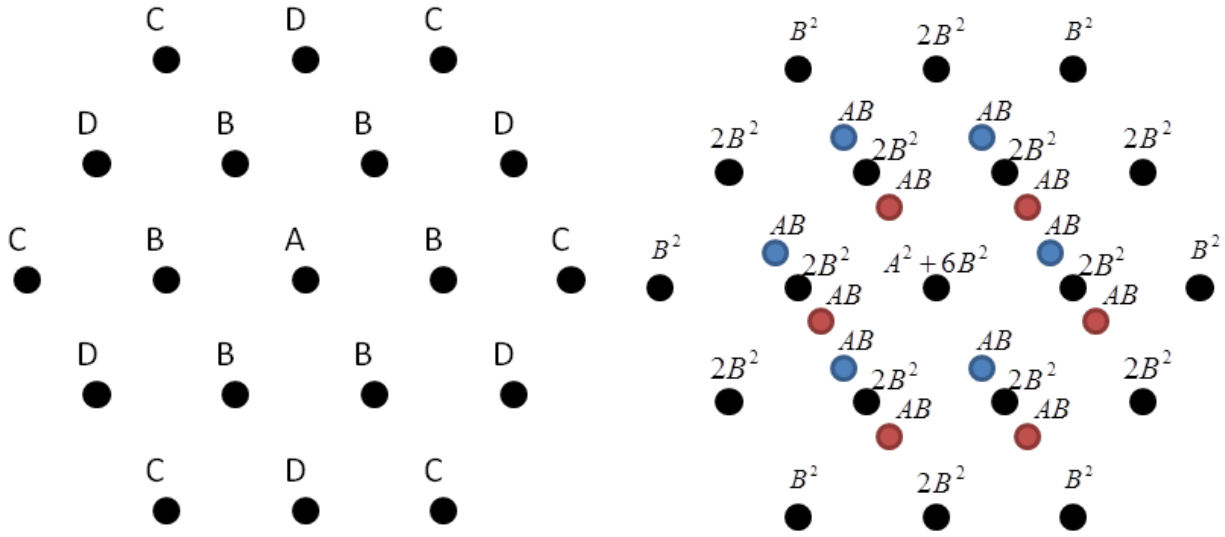
6.2.4 *Line, Quad, and Hex masks*

The line mask we have considered up until this point seems to have quite a caveat: there is no power in the illumination at the first order, at a $k_z = 0$. This is likely to end up as a hole in the system transfer function, which would only get more apparent as A' is attenuated to enhance the high spatial frequency content. But does this extend to other geometries or arrangements of frequencies in Fourier space?

If we consider the case of a quad mask, similar to the line mask but containing an arrangement of first orders in 4 points equidistant around the zeroth order, the same analysis can be performed with:

$$g(x,y,z) = \left| Ae^{ik_0 z} + Be^{ik_z z}\left(e^{ikx} + e^{-ikx} + e^{iky} + e^{-iky}\right)\right|^2 \tag{40}$$

If we factor this out in the same way as previously we get:



(a) Mask Components (b) Illumination Components

Figure 53: Frequency components in a hex mask, with A, B and C being the zeroth, first and a second orders respectively. D arises from cross-terms between B orders.

$$
\begin{aligned}
g(x,y,z) \;=\; & A^2 + 4B^2 + ABe^{i(k_0 z - k_z z)}\left(e^{ikx} + e^{-ikx} + e^{iky} + e^{-iky}\right) \\
& + ABe^{-i(k_0 z - k_z z)}\left(e^{ikx} + e^{-ikx} + e^{iky} + e^{-iky}\right) \\
& + B^2\left(e^{2ikx} + e^{-2ikx} + e^{2iky} + e^{-2iky}\right) \\
& + 2B^2\left(e^{ik(x+y)} + e^{-ik(x+y)} + e^{ik(x-y)} + e^{-ik(x-y)}\right)
\end{aligned}
$$

This gives rise to second orders and also cross-terms, which appear at $e^{ik(x+y)}$, as well as the same first orders at $k_z = k_0 - \sqrt{k_0^2 - k^2}$ and $k_z = \sqrt{k_0^2 - k^2} - k_0$. However, the first orders at $k_z = 0$ are still not present in this configuration, leading to similar potential issues in the final 3D transfer function. A figure illustrating these orders and their powers is available in figure 52.

Let us then consider the case of a hex mask, whereby the first orders appear in 6 points equally spaced around the zeroth order, and perform the same analysis:

$$g(x,y,z) = \left| Ae^{ik_0 z} + Be^{ik_z z} \begin{pmatrix} e^{ikx} + e^{-ikx} \\ e^{i\left(\frac{kx+ky\sqrt{3}}{2}\right)} + e^{-i\left(\frac{kx+ky\sqrt{3}}{2}\right)} \\ e^{i\left(\frac{kx-ky\sqrt{3}}{2}\right)} + e^{-i\left(\frac{kx-ky\sqrt{3}}{2}\right)} \end{pmatrix} \right|^2 \tag{41}$$

And again factoring this out as previously:

$$\begin{aligned} g(x,y,z) &= A^2 + 6B^2 + ABe^{i(k_0 z - k_z z)} \begin{pmatrix} e^{ikx} + e^{-ikx} \\ e^{i\left(\frac{kx+ky\sqrt{3}}{2}\right)} + e^{-i\left(\frac{kx+ky\sqrt{3}}{2}\right)} \\ e^{i\left(\frac{kx-ky\sqrt{3}}{2}\right)} + e^{-i\left(\frac{kx-ky\sqrt{3}}{2}\right)} \end{pmatrix} \\ &+ ABe^{-i(k_0 z - k_z z)} \begin{pmatrix} e^{ikx} + e^{-ikx} \\ e^{i\left(\frac{kx+ky\sqrt{3}}{2}\right)} + e^{-i\left(\frac{kx+ky\sqrt{3}}{2}\right)} \\ e^{i\left(\frac{kx-ky\sqrt{3}}{2}\right)} + e^{-i\left(\frac{kx-ky\sqrt{3}}{2}\right)} \end{pmatrix} \\ &+ B^2 \begin{pmatrix} e^{2ikx} + e^{-2ikx} \\ e^{2i\left(\frac{kx+ky\sqrt{3}}{2}\right)} + e^{-2i\left(\frac{kx+ky\sqrt{3}}{2}\right)} \\ e^{2i\left(\frac{kx-ky\sqrt{3}}{2}\right)} + e^{-2i\left(\frac{kx-ky\sqrt{3}}{2}\right)} \end{pmatrix} \\ &+ 2B^2 \begin{pmatrix} e^{ikx} + e^{-ikx} \\ e^{i\left(\frac{kx+ky\sqrt{3}}{2}\right)} + e^{-i\left(\frac{kx+ky\sqrt{3}}{2}\right)} \\ e^{i\left(\frac{kx-ky\sqrt{3}}{2}\right)} + e^{-i\left(\frac{kx-ky\sqrt{3}}{2}\right)} \end{pmatrix} \\ &+ 2B^2 \begin{pmatrix} e^{iky\sqrt{3}} + e^{-iky\sqrt{3}} \\ e^{i\left(\frac{3kx+ky\sqrt{3}}{2}\right)} + e^{-i\left(\frac{3kx+ky\sqrt{3}}{2}\right)} \\ e^{i\left(\frac{3kx-ky\sqrt{3}}{2}\right)} + e^{-i\left(\frac{3kx-ky\sqrt{3}}{2}\right)} \end{pmatrix} \end{aligned}$$

In this expansion, we see the same terms as in the quad mask case with cross-terms appearing with an additional term which generates first orders with intensity $2B^2$ (see figure 53 (b)). This suggests that a hex mask may still exhibit some optical sectioning with all the power removed in the zeroth order through a pupil mask - but perhaps more importantly, would have better signal than the other masks when high attenuation (but not total) is used. Additionally, a hex mask would also only need 60° of rotation in order to average correctly, as opposed to 180° in the line mask or 90° in the quad mask.

Another microscopy technique which can achieve high lateral resolution by enhancing high spatial frequency content relative to low spatial frequency content is through the use of annular pupil masks. By constructing illumination consisting of one or several rings at the edge of the pupil, the Airy disk usually seen in the focal plane is replaced with a Bessel beam. The central spot of this beam is smaller than the usually seen airy disk, at the expense of much more intense side lobes (the same as the central spot) and a larger axial extent. Using this illumination scheme in a point scanning confocal system can yield images with enhanced lateral spatial frequency content relative to normal PSCM systems. The price paid for this is that the final images also contain sidelobes which need to be deconvolved, and the light efficiency of such systems is also quite poor (around $\sim 1\%$, although engineering the pupil with an SLM can lead to light efficiencies of over 60%) [123, 124].

6.3 MASK DESIGN

As we have seen, by tailoring the spatial frequencies present in the mask, the transfer function of the system can be enhanced at high spatial frequencies. In this case, an amplitude mask is necessary which in turn creates (positive) peaks in amplitude at specific spatial frequency components: this restriction means that one cannot simply create a pattern of points in frequency space

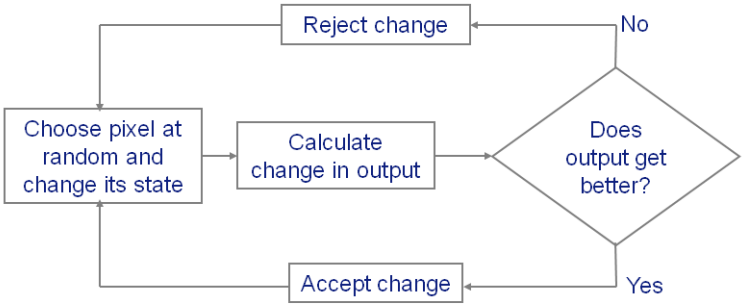


Figure 54: A flow chart of the hologram optimisation process.

and Fourier transform this into real space to design a mask, since this would result in a mask with a combination of amplitude and phase modulation.

In order to achieve this, existing code originally designed for creating binary masks in holography applications was adapted for use in this scenario. The original code begins by initialising an array as a random sequence of bits and taking as input a file specifying the desired frequency components in the mask. It then selects a random pixel and flips its value, calculating the resulting change in the Fourier transform in the process. In the simplest mode of operation, if the change has resulted in a closer fit to the desired pattern, it is saved and the process is repeated. After sampling over the whole array several times, it converges towards a hologram containing the distinct desired frequency components (see figure 54).

This mode of operation is able to create peaks of high intensity in Fourier space, but is unable to create peaks which have a desired relative intensity between them. In order to do this, a costimiser mode is also present: rather than simply check the Fourier transform of the mask at every cycle, a cost function is calculated on this basis. This cost function allows one to specify different (relative) intensities between the desired Fourier components, and have these taken into account when choosing to accept or reject a bit flip in the mask. This works by attempting to minimise the cost function, which was tailored to target specific intensities rather than simply maximising them.

In order to maximise the amplitude, the cost function was rewritten such that contributions to the real part of the desired image were the only ones that could diminish the cost of a bit-flip, while phase components always add cost. In this fashion, amplitude is maximised while phase is minimised at the desired frequency components. The code was also, to a large extent, rewritten in order to for it to function alongside Matlab, allowing for quick testing of a wide range of mask parameters. In this process the user interface was removed and several aspects of the code streamlined.

6.4 MODELLING

The operating theory that has been established here was modelled for various different system parameters. Modelling was performed by calculating the PSF of the system over a large range of defocus values, building up a 3D PSF over time. In the interest of speed, this calculation was performed in a multithreaded fashion, separating different intervals in defocus out to calculate on different CPU threads. This PSF was then put through a 3D fast Fourier transform, allowing an investigation of the transfer function of the system, which is more interesting from the point of view of system performance.

Modelling was performed with a variety of different variables in order to investigate the expected resolution and signal from the system. These variables include the weighting assigned second orders and cross-terms, the disk pattern used (line, quad or hex) and A', the amount of the zeroth order removed via a pupil mask.

Ultimately, it was found that the weighting of the second orders and cross-terms was restricted insisting on 50% transmissive masks. This is achieved by adding the zeroth order to the optimisation with a cost of 0.5, since the zeroth order encodes the average value of the resultant hologram. In effect, a second order weighting of 2 was the highest achievable, so the models presented

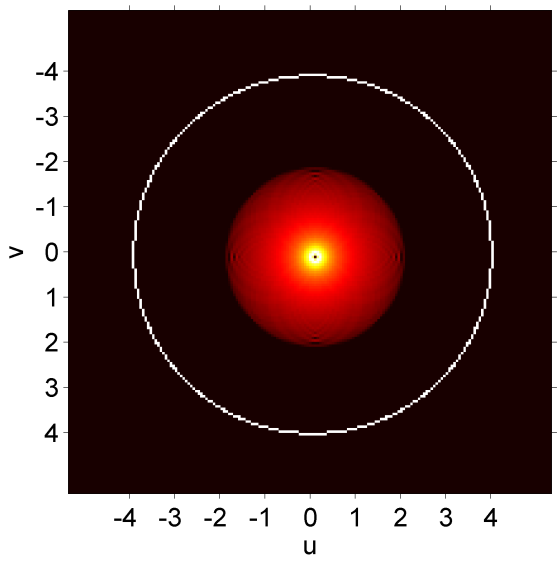
here are all with a second order and cross-term weighting of 2, while first orders have a weighting of 1.

Models were also made of conventional widefield, idealised confocal, and confocal with a 1 airy unit pinhole (figure 55), as a comparison to our system. These are all presented surrounded by the region of support of the microscope in white, which can be shown to take the form [125, 126]:

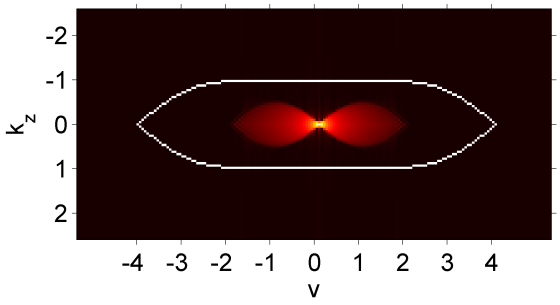
$$|k_z| = \begin{cases} 1 & \text{if } 0 \leq l \leq 2 \\ l - \frac{l^2}{4} & \text{if } 2 \leq l \leq 4 \end{cases} \tag{42}$$

With $l = \sqrt{u^2 + v^2}$. The conventional and confocal transfer functions were covered in chapter 1. Confocal with an airy unit pinhole is simulated here as example of a more realistic transfer function one might achieve from confocal microscopy, as signal from the microscope drops quickly for smaller pinholes than this, quickly getting dominated by noise.

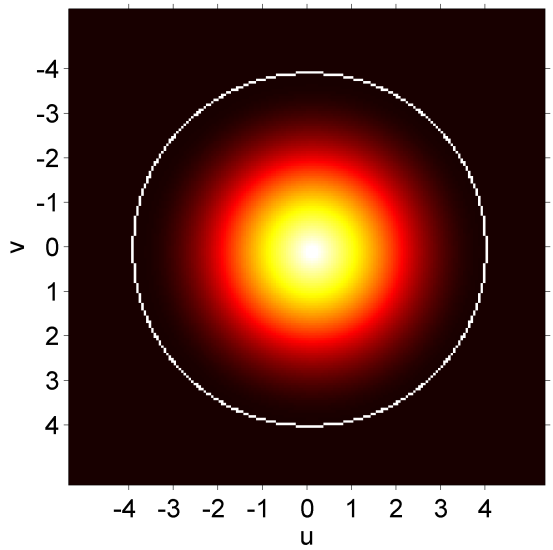
On some of the figures presented in the next sections, streaking or lines can be seen extending outside the region of support. This is due to aliasing, the effect of performing a fast Fourier transform on data which is bounded by a finite box, in this case a rectangle. The resulting Fourier transform ends up as a convolution of of the bounding box's Fourier transform and the data's Fourier transform, which in the case of a rectangular box is a sinc function. It is possible to address this issue by performing windowing before transforming data, whereby the data is multiplied with another boxing function which has a friendlier Fourier transform. In a later section, a Gaussian window is used, which has the property that its Fourier transform is also a Gaussian function.



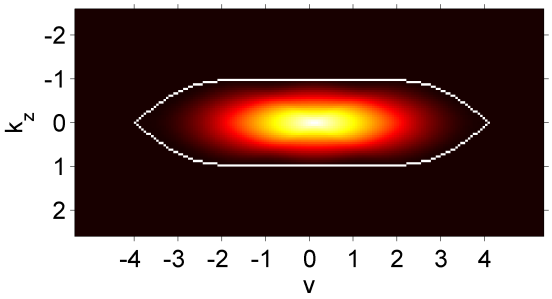
(a) Conventional



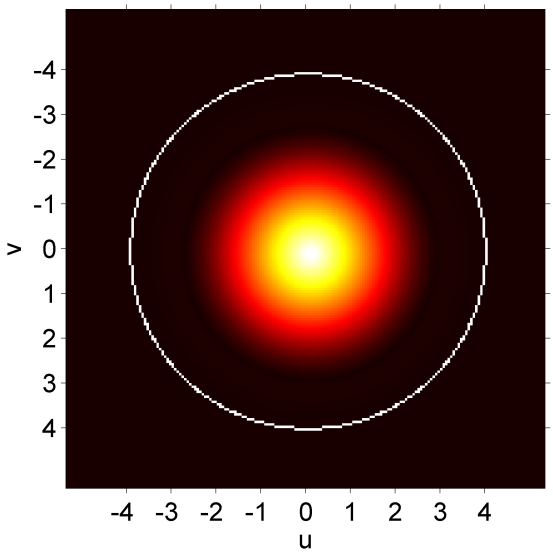
(b) Conventional



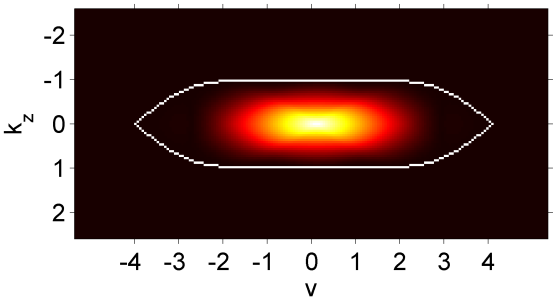
(c) Confocal



(d) Confocal



(e) Confocal Airy



(f) Confocal Airy

Figure 55: Transfer functions in u, v and k_z, v for conventional, confocal, and airy pinhole confocal arrangements.

6.4.1 *Resolution*

The 3D transfer functions generated are presented here as projections along the u, v and u, k_z axes. The colour coding used reflects the quartic root of the transfer functions (after normalisation), as viewing them on a linear scale would not reveal enough detail to appreciate the extent of the functions, while a log scale brings out too much noise in the final image. Here rather than talk about A' directly we will concern ourselves with a damping factor ζ, such that $A' = A - \zeta A$. This ζ factor represents the amount of the zeroth order that is removed at the pupil plane, and relates more directly to the experimental apparatus, as a pupil mask would be described in the same terms.

Figures 56, 57 and 58 (panels on the left) show the transfer functions plotted along the u, v axes for all the disk types (line, quad and hex) at 3 different values of ζ (0, 0.7 and 1). These values of ζ were chosen as they illustrate the extremes as well as an example of behaviour for intermediate zeroth order removal. Panels on the right show rotated versions which show how an averaged transfer function would look while spinning the disk.

The u, v renders of the line pattern illustrate quite well the convolution between the OTF and the mask frequencies: a conventional transfer function is replicated centered on the second order of the mask, as stipulated earlier in subsection 6.2.3. The zeroth order replicates a transfer function as well - filtering this out by increasing the ζ parameter leads to a resulting decrease in power in this order as we would expect, until the total transfer function looks like 2 conventional transfer functions separated by $4\nu_0$. This increase also appears to extend the lateral reach of the transfer function, relatively speaking, although results in a hole in the centre of the transfer function.

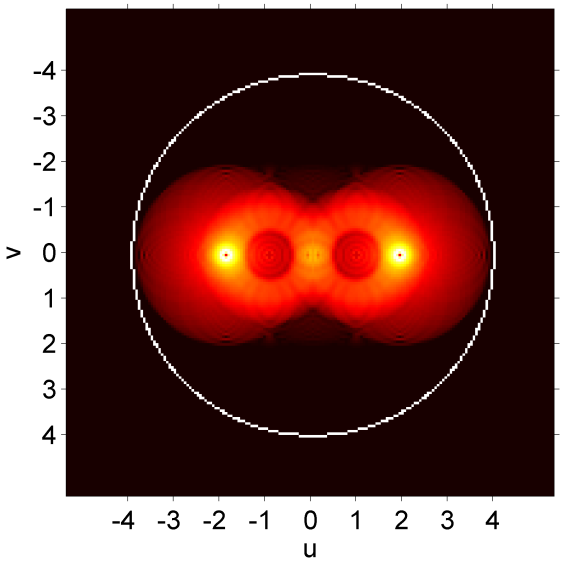
The u, k_z renders show how the orders appear in 3D, which matches with section 6.2.3, showing the orders generated outside of $k_z = 0$ and their associated replicated conventional transfer functions. At a ζ of 0, these axial modes look far more powerful than the second order modes, but increasing ζ to 0.7

they look equally powered, associated with a relative increase in the lateral extent of the transfer function. The rotated form of this shows the region of support being almost entirely filled by the transfer function in the axial direction. Removing all the zeroth order completely attenuates the axial modes, resulting in a transfer function which now again does not fill the the 'missing cone' needed for optical sectioning, but does extend far laterally.

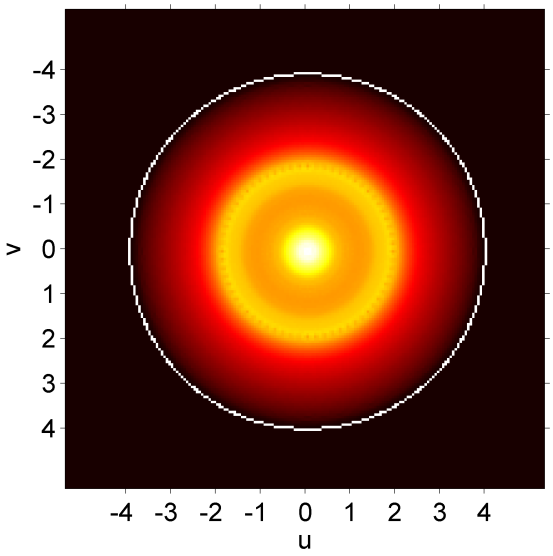
With the quad mask (figure 57), the results of the modelling look very similar in the u, v plane. The cross-terms, however, generate a conventional transfer function which overlaps with the zeroth order, as they have a lateral resolution of $\sqrt{2}v_0$. This means that removing all the power in the zeroth order by increasing ζ does not completely remove this microscope's ability to section large objects, but it does reduce the overall extent of the transfer function axially to a thin central band.

We see very similar results with the hex mask - in this instance we see first orders at $k_z = 0$ generated as well, which appear to increase the signal in the more central regions of the transfer function. Removing the zeroth order completely has a similar effect as in the quad mask, reducing the axial extent and extending the lateral extent of the transfer function.

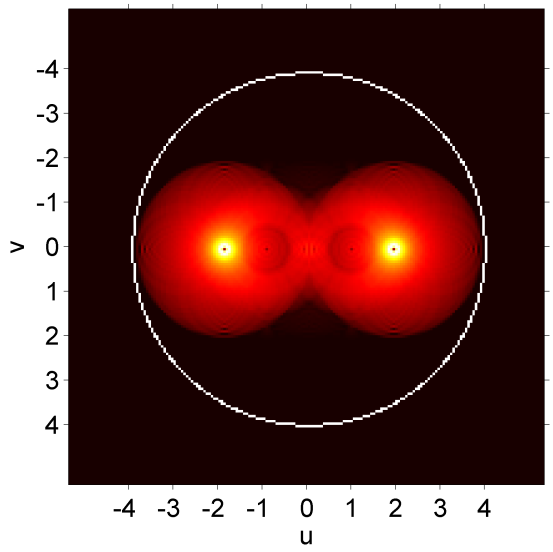
To summarise, it appears as though a general principle we observe in all these masks is that, as we approach $\zeta = 1$, a tradeoff is made between axial and lateral resolution. It appears from the figures discussed that the ideal range for good enhancement of resolution in both directions is in the intermediate range.



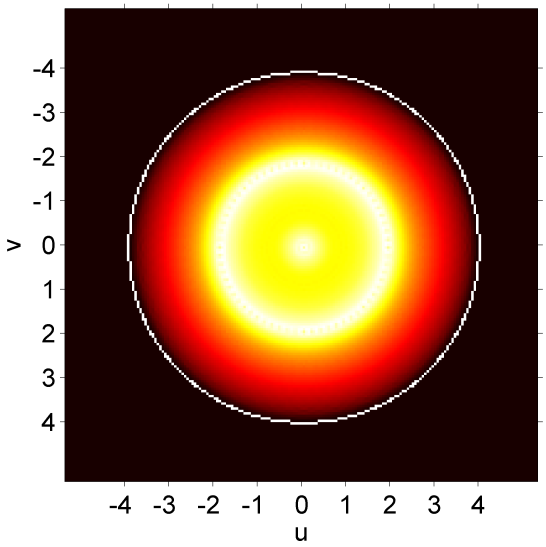
(a) $\zeta = 0$



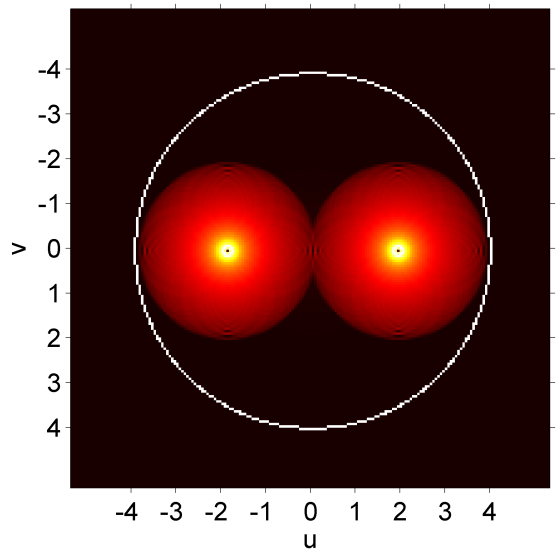
(b) $\zeta = 0$, rotated



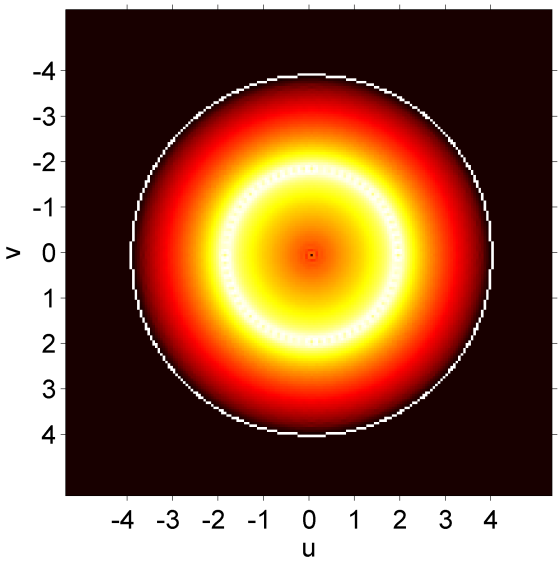
(c) $\zeta = 0.7$



(d) $\zeta = 0.7$, rotated

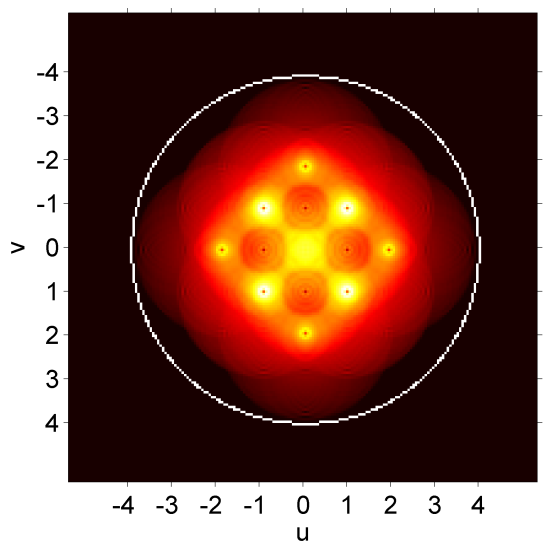


(e) $\zeta = 1$

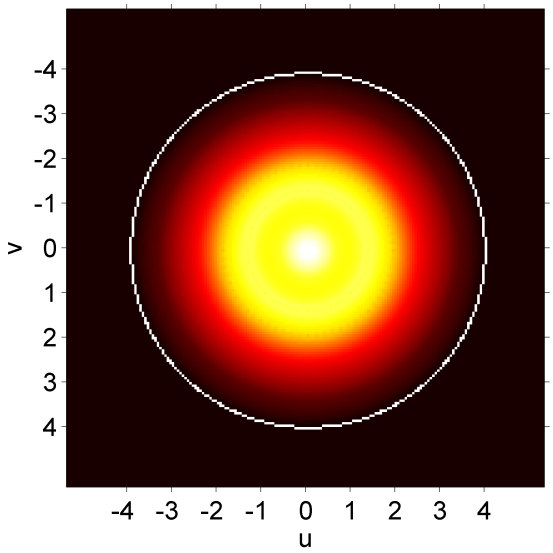


(f) $\zeta = 1$, rotated

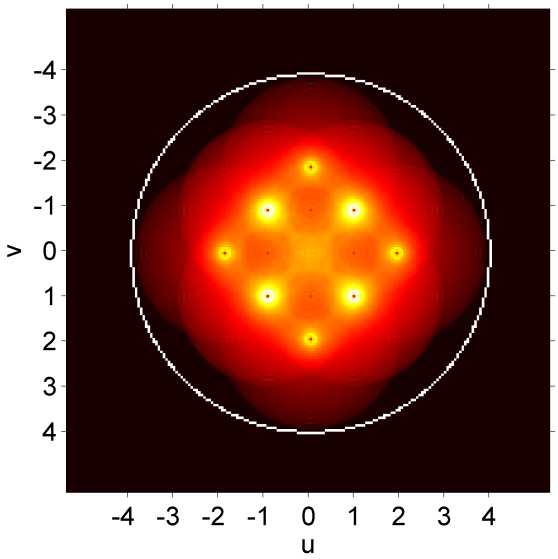
Figure 56: The 2D OTF in focus for the line mask, for different values of ζ.



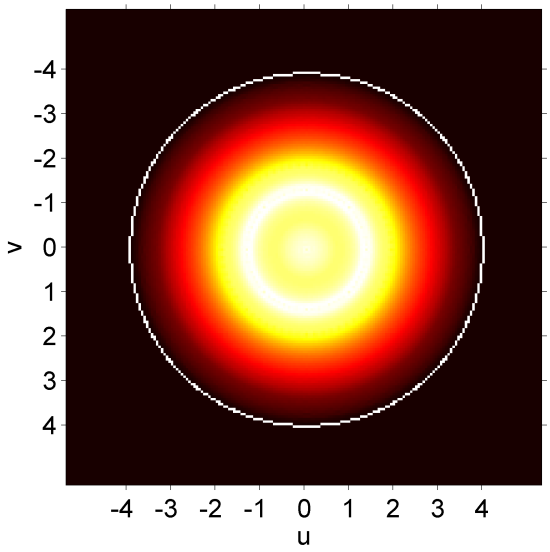
(a) $\zeta = 0$



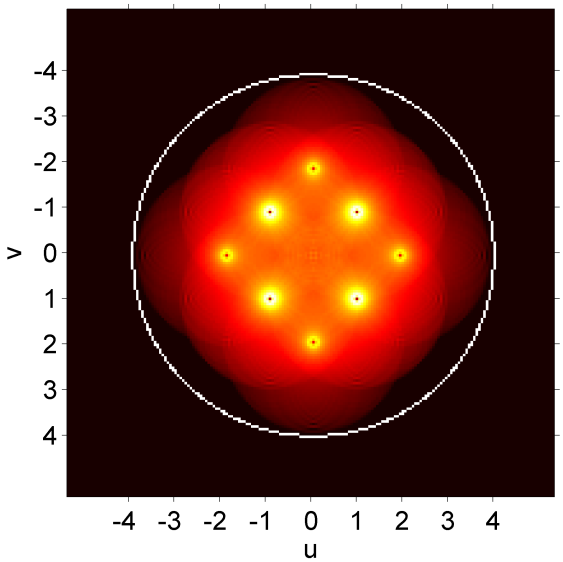
(b) $\zeta = 0$, rotated



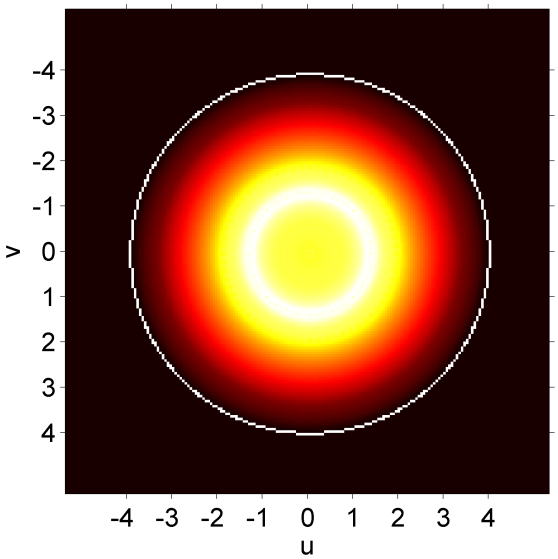
(c) $\zeta = 0.7$



(d) $\zeta = 0.7$, rotated

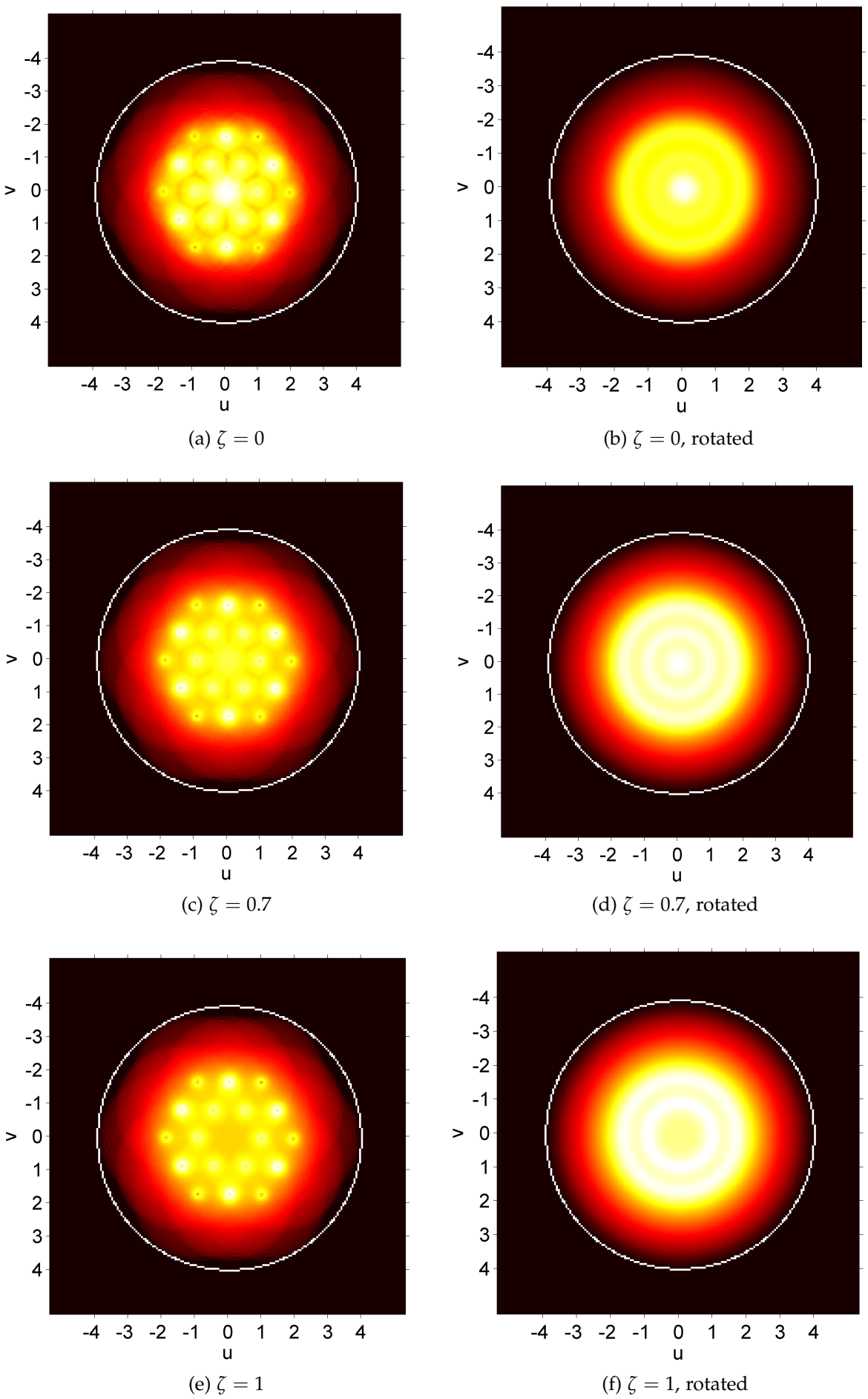


(e) $\zeta = 1$



(f) $\zeta = 1$, rotated

Figure 57: The 2D OTF in focus for the quad mask, for different values of ζ



(a) $\zeta = 0$

(b) $\zeta = 0$, rotated

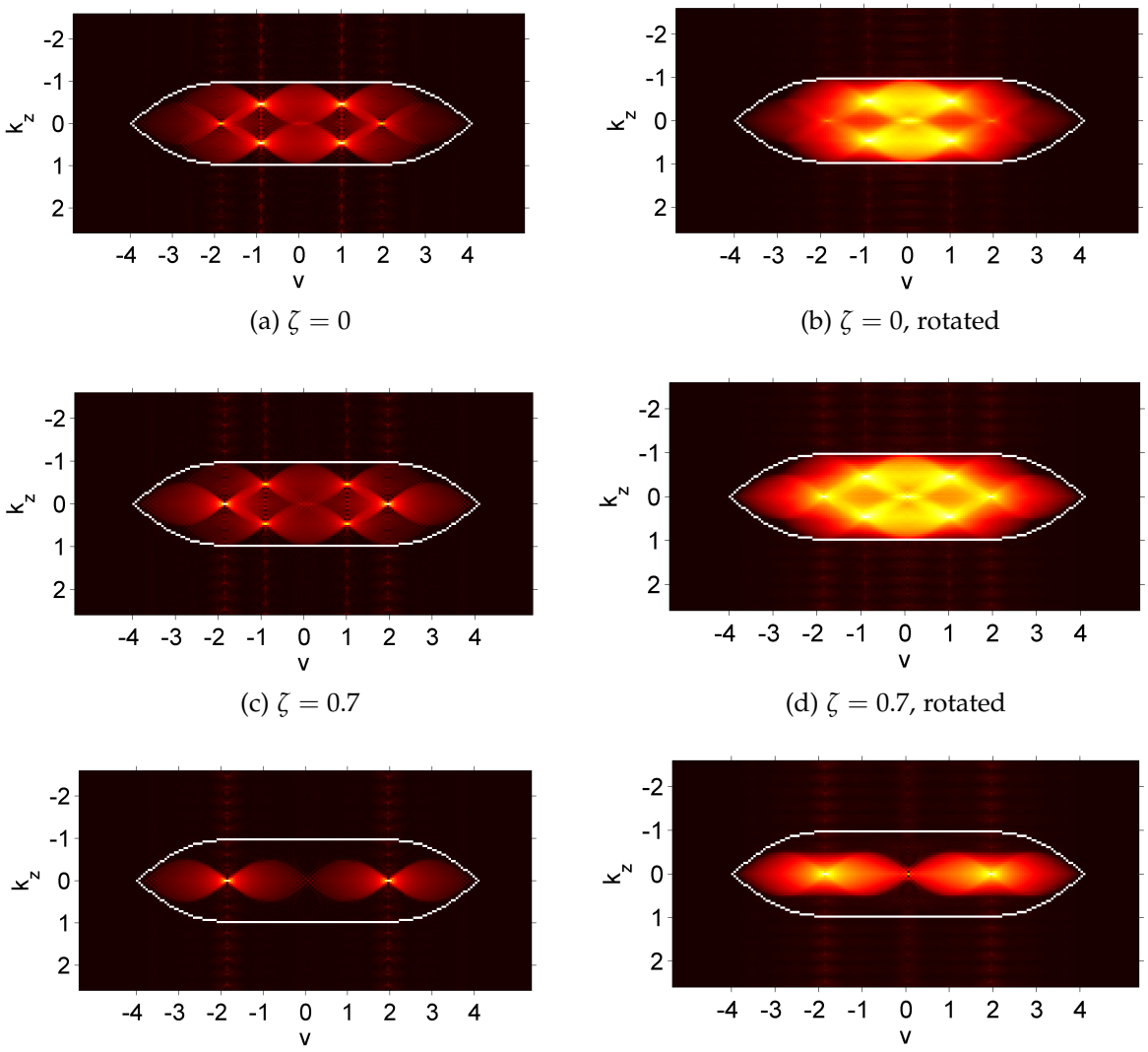
(c) $\zeta = 0.7$

(d) $\zeta = 0.7$, rotated

(e) $\zeta = 1$

(f) $\zeta = 1$, rotated

Figure 58: The 2D OTF in focus for the hex mask, for different values of ζ



(a) $\zeta = 0$

(b) $\zeta = 0$, rotated

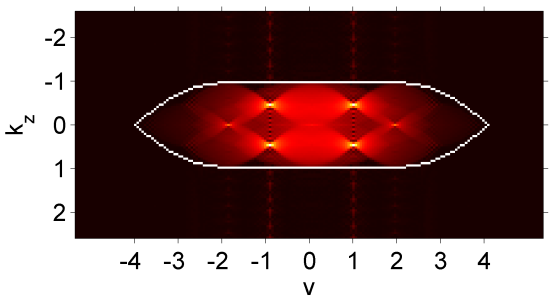
(c) $\zeta = 0.7$

(d) $\zeta = 0.7$, rotated

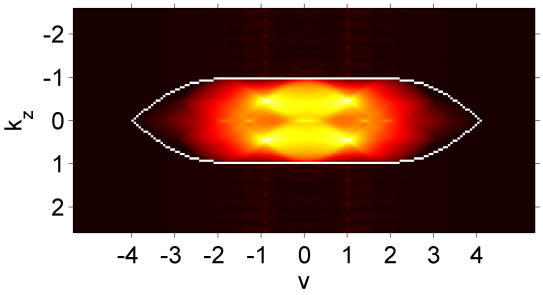
(e) $\zeta = 1$

(f) $\zeta = 1$, rotated

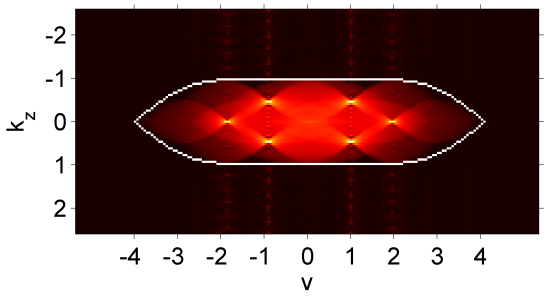
Figure 59: The 3D OTF in focus for the line mask, for different values of ζ



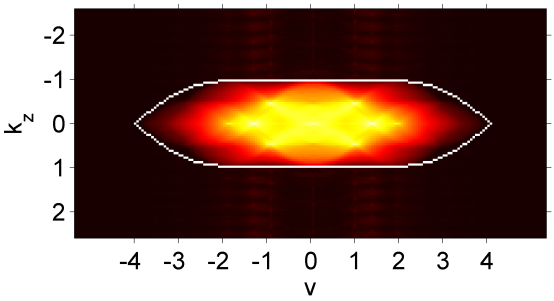
(a) $\zeta = 0$



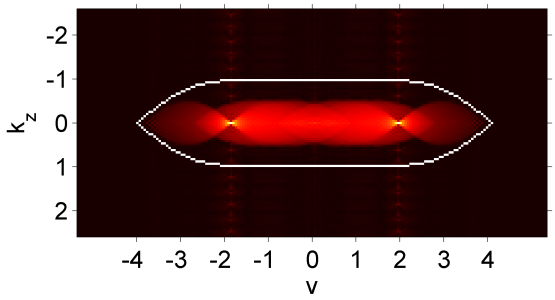
(b) $\zeta = 0$, rotated



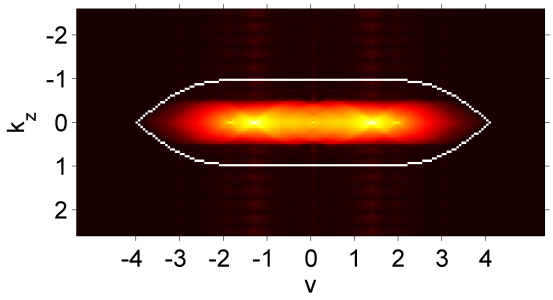
(c) $\zeta = 0.7$



(d) $\zeta = 0.7$, rotated

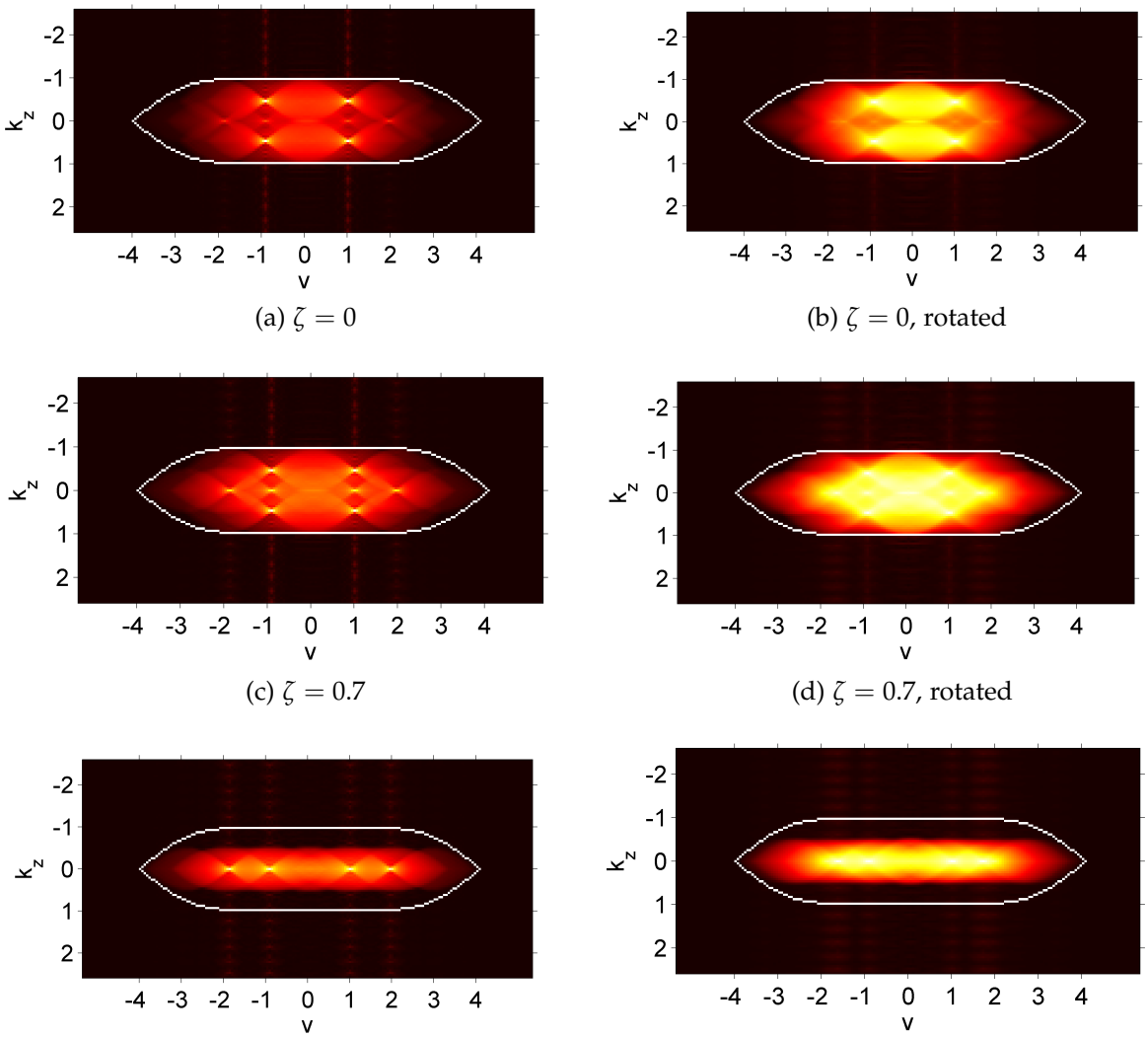


(e) $\zeta = 1$



(f) $\zeta = 1$, rotated

Figure 60: The 3D OTF in focus for the quad mask, for different values of ζ



(a) $\zeta = 0$

(b) $\zeta = 0$, rotated

(c) $\zeta = 0.7$

(d) $\zeta = 0.7$, rotated

(e) $\zeta = 1$

(f) $\zeta = 1$, rotated

Figure 61: The 3D OTF in focus for the hex mask, for different values of ζ

6.4.2 *Signal*

In order to investigate the impact of the ζ parameter, a simulation was run varying the amount of zeroth order removed and calculating a 3D PSF at each cycle. The PSF is then integrated over x and y at focus and divided by the conventional background detected at the cameras. This yields a measure of the relative intensity of the signal in focus compared to out-of-focus contributions, which we can interpret as the signal of the microscope.

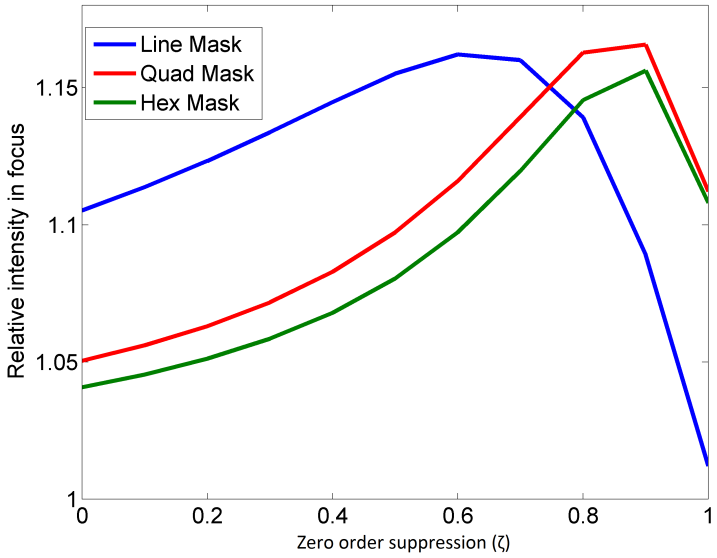


Figure 62: A plot of the detected signal (relative intensity in focus over out of focus) versus the zero order suppression term ζ.

In figure 62, a plot of the relative intensity in focus versus the zeroth order suppression parameter ζ is presented. We can see that as the zeroth order is removed, the signal initially increases (most likely as a result of increased illumination pattern contrast) however drops quickly at very high values of ζ. Interestingly, the signal is also relatively increased for the hex and quad patterns as opposed to the line patterns, as well as the cut-off for removal of the zeroth order. This is because, as seen in the generated transfer functions previously, there is no first order generated in the autocorrelation of the aperture mask for the line pattern. Although this is also true of the quad pattern, the presence of the cross-terms means that the region of the transfer function around the first order is still covered, since these are at a distance of $\sqrt{2}$ from the origin. From these plots, we can see that, as previously, an ideal value of ζ is found at intermediate values, from 0.6 in the line mask to 0.9 in the quad and hex patterns.

6.5 EXPERIMENT

6.5.1 *Experimental Setup*

Figure 63 presents the experimental setup of this microscope. Although based on the same experimental setup as the aperture correlation microscope in chapter 3, this experiment has several major differences to the first: firstly, it uses a coherent illumination source, along with which comes a spatial filtering and beam expansion setup, as well as polarisation control. On the microscope side, the disk is no longer simply placed at the output plane of the microscope but behind a 6F relay system designed to add another factor of 2 to the magnification of the objective by extending the effective tube lens focal length. This additional magnification serves to fit the disk mask's first orders at the edge of the objective's pupil: in order to aid in manufacturing, the disk was designed with half the required spatial frequency. The 6F system also allows for limited focal length adjustment, allowing the position of the first orders at the pupil to be slightly tweaked, aiding in alignment. Finally, by placing a mask at the pupil of this system, the zeroth diffractive order from the spinning disk can be blocked.

6.5.2 *New Spinning Disk*

A new spinning disk was fabricated with 3 separate mask areas at different radii, using the mask design software from section 6.3. Models were originally designed for a 40x 0.75 NA objective, where the first orders sit at $0.95\nu_0$ - corresponding to a pattern pitch of 30µm. Although the disk could have been designed at the intended spatial frequency, this would have relied on a very small manufacturing pitch of $\sim$ 1µm; not having any knowledge of the equipment used for manufacturing, it was decided to create the disk with half this frequency and then rely on an additional magnification step.

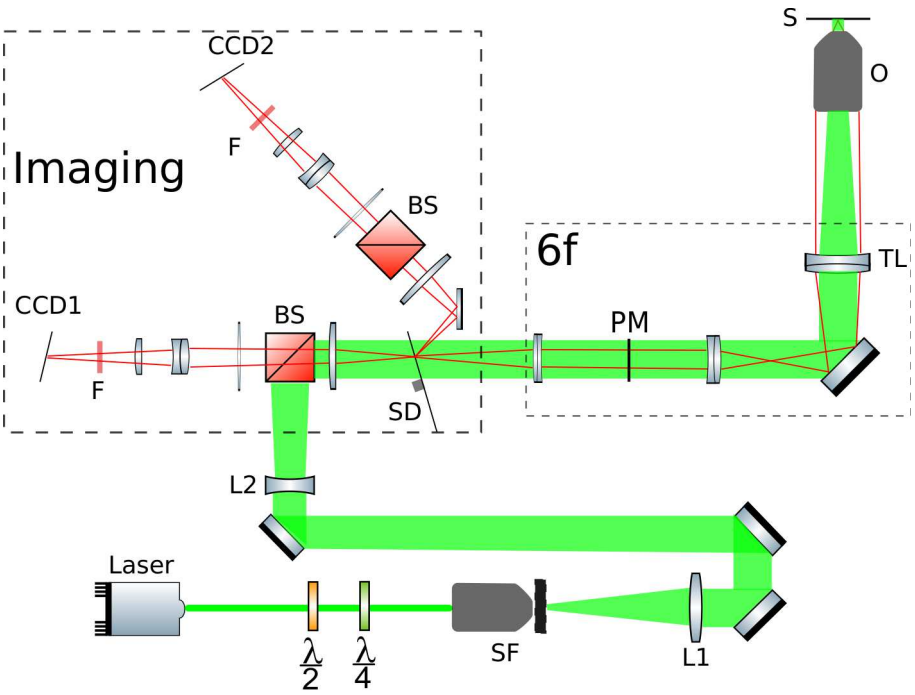
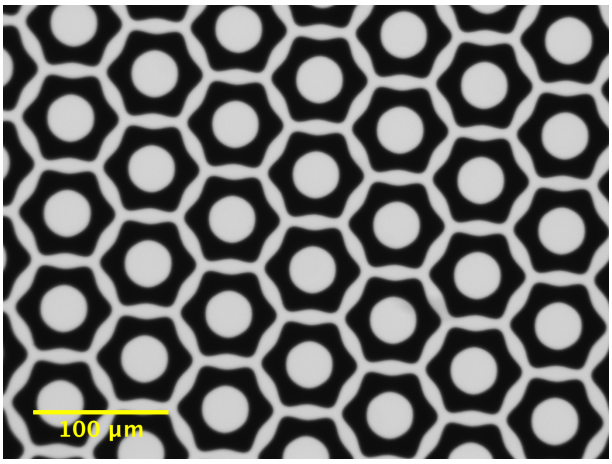
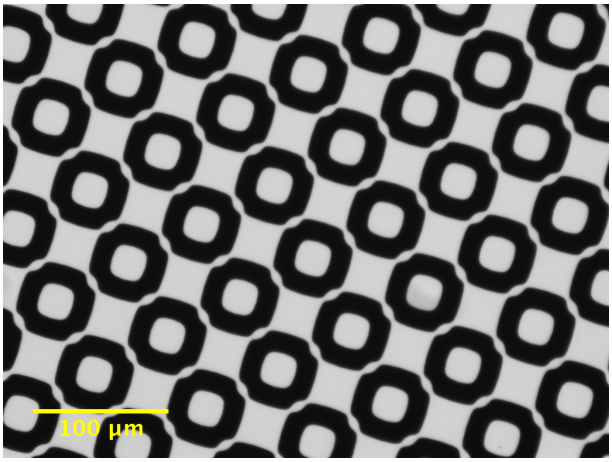


Figure 63: Experimental setup of the super-resolving aperture correlation microscope.

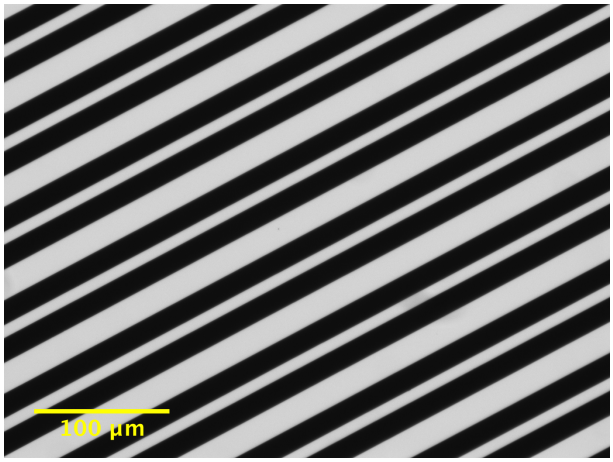
Laser illumination at 532nm is polarisation controlled by a $\frac{\lambda}{4}$ and $\frac{\lambda}{2}$ plate. It then enters the spatial filter SF, where it is focused through a pinhole and collimated by L1. L2 counterbalances the effect of the first element of the imaging system after the beamsplitter BS, such that the beam is collimated at the spinning disk SD. It then enters the 6f system, where it passes through the pupil mask and is demagnified by a factor of 2 before entering the microscope objective. Excited fluorescence returns through the 6f system to the disk SD, where signal is imaged to the cameras CCD1 and CCD2.



(a) Hex mask



(b) Quad mask



(c) Line mask

Figure 64: Images of the new spinning disk prototype taken with a 20x objective.

In order to fabricate the new disks, the unit tiling cell of the patterns was identified, and then traced as a vectorised format: this was then incorporated into a handwritten postscript file where the tiling and scaling was set appropriately. Finally, after several months, the disks were successfully created.

In figure 64, images of the new disk taken under a 20x objective in transmission are shown. Measuring the pitch of the patterns reveals that the scaling is correct, with a pattern pitch of 60µm present in all disk sectors. In order to mount the disk onto a motor, care was taken to ensure the flattest possible mount to reduce any wobble during rotation. This was done by mounting the disk with a small amount of epoxy and spinning the motor at $3000rpm$ for several minutes as the glue dried.

6.5.3 *Illumination*

The illumination in this system is provided by a DPSS laser operating at 532nm. A set of polarisation optics is used to then control the polarisation of the illumination. At the shutter of the laser, a polarising beamsplitter was placed to provide linearly polarised output (the output of the laser was measured to be highly elliptical). A sheet quarter waveplate and half waveplate are placed near the output of the laser so that arbitrary polarisations can be created, although generally circularly polarised light was used for several reasons. The polarisation of the illumination at the input pupil of the microscope objective is known to affect the contrast of the resulting pattern. Using linear polarisation with a spinning disk would result in a rotation dependent contrast which could cause artefacts or anomalies in the resultant images. Circular polarisation has also been shown to improve contrast in high NA imaging applications. Circular polarisation was achieved here by placing a left-handed circular polariser at the input pupil of the microscope objective and rotating the waveplates to null the output. Removing the circular polariser then ensures that light at the pupil is right-hand circularly polarised.

Polarised illumination then enters a spatial filter, composed of a 20x microscope objective and a 10µm pinhole at the focus of the objective. The pinhole size was chosen to be slightly smaller than the expected airy disk of the objective, such that high order lateral modes of the laser are filtered through this process. Diverging light from the pinhole is then collimated by a lens such that a $\sim 20mm$ beam diameter is achieved.

The beam is then steered by two mirrors, which allow control over the direction of the beam as it hits the dichroic (550nm cut-off) in the imaging system and eventually its position at the objective pupil. Because a lens appears in the imaging system after the dichroic, a lens is placed before this in order to compensate and retain a collimated illumination beam at the plane of the spinning disk. This lens is chosen such that the illumination on the di-

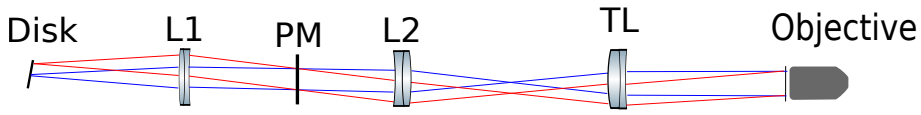
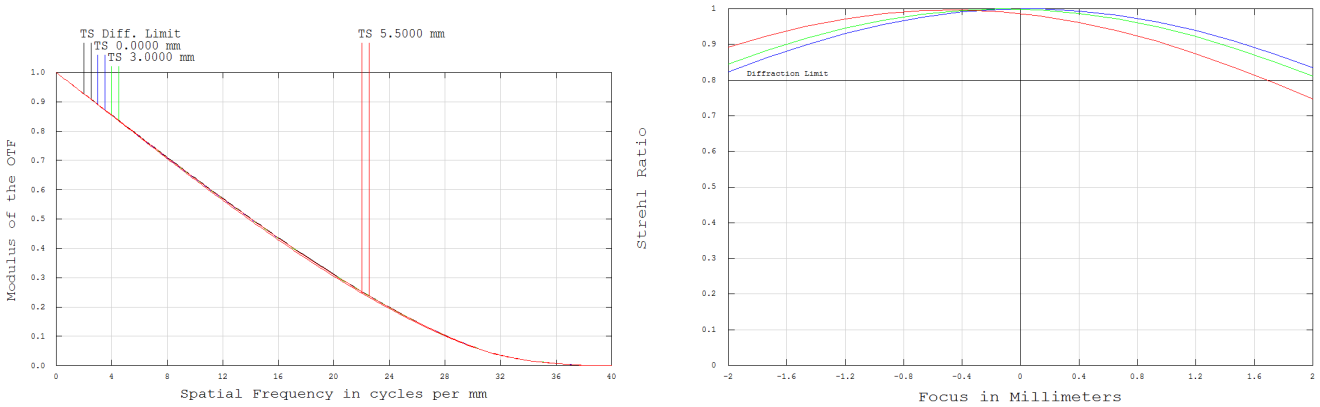


Figure 65: A layout of the 6f optical relay from the disk to the microscope objective, showing the location of the pupil mask (PM).



(a) MTF

(b) Strehl ratio against defocus

Figure 66: Plots of the 6f optical relay's MTF and Strehl ratio.

chroic is at the stop of this lens, in order to also compensate for the dichroic's poor flatness and resultant aberrations in the beam. Typically, laser powers of $20 - 30mW$ were used throughout imaging.

6.5.4 *Imaging*

The imaging system used from the spinning disk to the cameras is identical to that in chapter 3, and given the negligible difference in wavelengths and use of the same cameras in this setup it can be assumed to have the same characteristics as in figure 21. The calibration projection arm is not shown in the diagram for clarity, but exists in the same fashion as in Chapter 3.

The 6f optical relay from the disk to the microscope objective is a new design created to change the effective focal length of the tube lens in the microscope, a $180mm$ doublet, to $\sim 360mm$. This is necessary in order to double the magnification of the system, positioning the first orders of the aperture mask at the edges of the objective's pupil. It additionally has the

advantage that the pupil of this relay can then be used to mask the zeroth order of the aperture mask, rather than attempting to mask the objective pupil, which is essentially on its first element.

The relay is constructed from $400mm$ and $200mm$ doublet elements, with the last element being the $180mm$ tube lens inside the Olympus microscope. A layout of the system is shown in figure 65, while plots of the system performance are on figure 66. From the MTF, we can see that the system appears diffraction limited at the design wavelengths and fields. From the plot of Strehl ratio against defocus, we can see that the system has a very long depth of focus and remains diffraction limited within almost $\pm 2mm$ of the focal plane. The final effective focal length of the relay after optimisation is $340mm$, resulting in an additional magnification factor of $\frac{340}{180} = 1.9$.

At the pupil of the 6f system, the removal of the zeroth order from the aperture mask can be performed. Although ideally, this would be done by vacuum depositing an absorptive coating on glass and tweaking the deposition time to achieve a particular extinction coefficient, this would have taken more time than was remaining on this project. Instead, a wire was placed at the pupil: ensuring it is in focus and centred, the zeroth order can be completely removed. Unfortunately, this means that results could only be obtained for values of $\zeta = 0$ or 1.

6.6 RESULTS AND DISCUSSION

This microscope setup was tested by imaging $0.2\mu m$ Invitrogen Fluocell spheres, which nominally excite at $540nm$ and emit at $560nm$, matching the illumination and detection wavelengths well. Indeed, a strong fluorescent signal was observed from these beads throughout imaging. A significant problem imaging in this setup is that, due to ongoing issues with alignment of the calibration system, full-field registration is not currently functioning. The likely cause is that this registration algorithm is sensitive to differences in the loc-

ation of the calibration and imaging pupils: a mismatch in these means that, although the calibration pattern is properly registered, images from the microscope are not. Attempts have been made to fix this issue by replacing the calibration projection lens, but as yet full-field registration is not available. Thankfully, despite these issues, a central region of the field of approximately 100x100 pixels is registered well enough for subtraction and subsequent analysis.

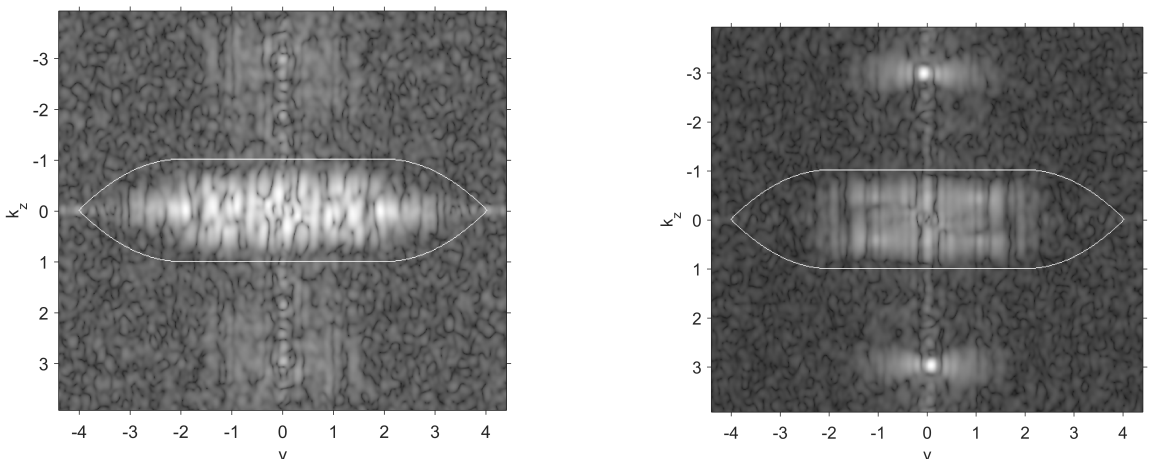
Data was acquired by taking image stacks of the beads on both cameras, and importing registered transmitted and reflected camera frames. These are then cropped down to the well-registered region of interest at the center of the field. Transfer functions of the system are plotted by 3 dimensionally Fourier transforming the central region of the field of view, where approximately $10 - 15$ beads are present, which gives enough signal to fill the transfer function relatively well. In order to combat aliasing effects, which arise due to the finite size of the field, a gaussian window is applied to the stacks beforehand in x, y and z. Because the Fourier transform of a Gaussian function is another Gaussian (rather than a sinc function, as with the original square window), this reduces the appearance of artefacts along the axes of the resulting transfer functions, at the cost of also reducing the signal. In the interest of maintaining enough signal to observe the transfer functions, the windowing is not always taken to its full extent, and some residual aliasing can be observed in some of the generated figures as lines along $v = 0$ and $k_z = 0$.

In figure 67 (b) of the line mask disk, the transfer function of an image stack taken without masking the zeroth order is shown, with the region of support shown in white. Comparing this image to the models shown in figure 59, we can see that there is generally a good agreement to the theory, although the signal at high lateral spatial frequencies past the conventional limit of $2\nu_0$ is not resolvable. The side lobes present at $k_z = \pm 3$ are likely the result of speckle, due to to dust present in the path of the zeroth order on the tube lens or objective pupil.

Figure 67 (a) shows the transfer function of an image stack from the same disk taken while completely blocking the zeroth order, again with the region of support shown in white. Comparing this image to the models in figure 59, there is good agreement on the lateral extent of the function, where we clearly have the ability to resolve up to $3\nu_0$. Less clear is why the system appears to fill the 'missing cone' and exhibit optical sectioning, at odds with the previous models. The most compelling explanation for this is that not all of the zeroth order was removed at the pupil mask, resulting in residual first order terms in the transfer function. Further work is necessary to determine to what extent this is true; replacing the pupil masking system with a more robust system based on a vacuum deposited agent would likely solve this issue, as well as allow for testing at a wider range of values of the removal factor.

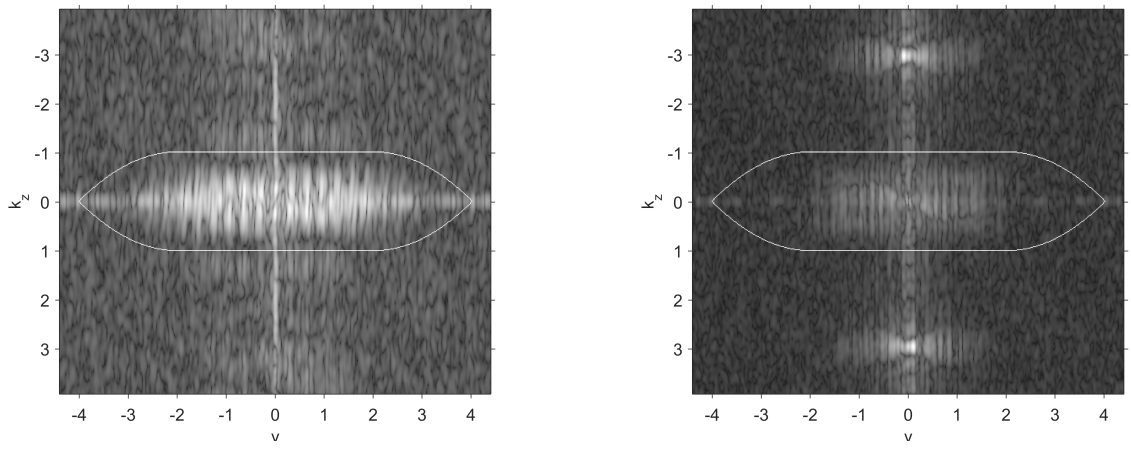
Figures 68 (a) and 68 (b) show the resulting transfer functions using the hex mask with and without pupil masking respectively. As suggested by the modelling of the signal from the microscope in section 6.4.2, the signal from this setup without any pupil masking appears lower than in the line mask case. Otherwise, these transfer functions look very similar to the previous case as we might expect. Here too, removing the zeroth order completely results in the same, wider transfer function that we might have expected for only intermediate values of pupil masking.

A central 100x100 field of beads using the line mask with $\zeta = 1$ is shown in figure 69. Subfigure (a) shows a conventional image, obtained by summing the transmitted and reflected frame (after scaling to the same intensity). In subfigure (b), the subtracted, super-resolved beads can be seen, where by observing the size of the beads resolution improvement has clearly taken place. Some of the beads appear to be completely subtracted - this is because they are out of focus at this plane in the stack.



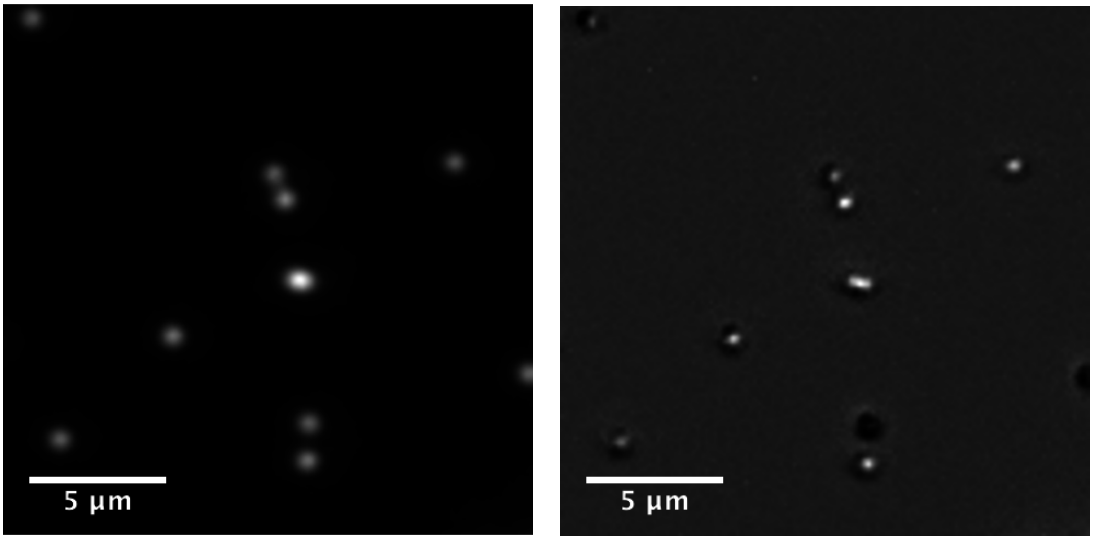
(a) (b)

Figure 67: Optical transfer functions of the microscope with the line mask, with (a) and without (b) masking the zeroth order in the pupil. The region of support is shown in white.



(a) (b)

Figure 68: Optical transfer function of the microscope with the hex mask, with (a) and without (b) masking the zeroth order in the pupil. The region of support is shown in white.



(a) (b)

Figure 69: Field of beads, conventional (a) and super-resolved (b), using the line mask with $\zeta = 1$.

6.7 FUTURE WORK

Clearly, there are some issues to be addressed in this experimental setup which could lead to a more complete investigation into the system's performance in the future. Fixing the calibration system so that full field registration works would be very helpful, improving the signal available for analysis later on. Where here only $10 - 15$ beads can be fourier transformed at once, typically over a hundred or more can be present in a full field of view. It would also allow imaging of extended biological samples, giving an opportunity to test the system with deeper and more scattering samples, as well as being a good way to demonstrate is validity in the field. A better pupil masking system based on vacuum deposition onto glass would also be particularly useful, allowing a fuller investigation into the implication of removing the zeroth order at the pupil plane. Similarly, a better laser source without strong temporal noise would be beneficial to testing this setup completely. The effect of partial coherence of the zeroth order could also be an interesting avenue

of research, as this could address the side-lobes present in the $\zeta = 0$ data by making it less susceptible to dust.

A related approach to using amplitude masks as we have here would be to use a binary phase mask instead. A phase mask could increase the light budget even further in this type of microscope, allowing all of the illumination light through the disk (twice as much for our 50/50 masks), without affecting the illumination contrast.

6.8 CONCLUSION

We have described in this chapter a new type of super-resolving aperture correlation microscope, which functions by using coherent illumination at the edge of the objective pupil while introducing extra spatial frequencies into the spinning aperture mask. The operating theory of this microscope was described, and simulated performance for a range of different parameters and mask types was explored. A method for designing new disk masks based on holographic techniques was also introduced, used to produce masks with extra spatial frequency content at twice the illumination frequency. Results from a prototype of this microscope were then presented, giving some promising results for the future, where a factor of 1.5 lateral resolution improvement was observed. Finally, some avenues towards future improvement of the system were described, in particular an idea to use a phase rather than amplitude aperture mask.

7

CONCLUSIONS AND FUTURE WORK

CONCLUSIONS This thesis set out to further the development of Aperture Correlation Microscopy, focusing in part on devices with industrial applications along with Aurox, a company which specialises in constructing these devices. These are constructed both to provide axial sectioning for contrast enhancement, and also with the aim of providing lateral super-resolution. In chapter 2, the process of acquiring optical sectioning is introduced, along with several different approaches to resolution improvement and super resolution. In so doing we show how aperture correlation takes its place as a real-time, motion artefact-free, light-efficient sectioning class of microscopy techniques.

A two-camera aperture correlation microscope was designed in chapter 3. The theory of operation of this microscope was presented, explaining how structured illumination and detection through the same mask could lead to a microscope able to resolve axially through a simple image subtraction step. An experimental version of this microscope was then introduced, justifying equipment choices and imaging systems used along the way. By using this system to image microscopheres as well as fluorescent thin sheets, its capability to resolve axially was showcased - while at the same time finding that the results matched reasonably closely to the theory. Image stacks of pollen grains were then used to show how the enhanced contrast from the microscope could be used to observe fine details and build 3 dimensional models of samples. The main advance represented by this system is in field size, previous versions of this microscope using a single camera [79, 20].

In chapter 4, a real-time image registration algorithm used to power the previous chapter's image processing was described. Since incoming frames

from a two-camera aperture correlation microscope come from slightly different imaging setups, they must be aligned before the subtraction process can yield a confocal image. The graphics processing unit, ubiquitous in modern computers, was leveraged for the purpose of aligning and subtracting frames, after calculating the necessary transform through the projection of a calibration image onto the spinning disk. This results in a registration algorithm working on data in real-time (16 frames per second) but capable of speeds of over 200 frames per second.

An aperture correlation microscope designed for reflective samples was presented in chapter 5, constructed in collaboration with Aurox ltd. as part of the CASE contribution of this project. The microscope was designed to be used to survey large fields, for which there are applications in semiconductor fabrication and testing, while also using UV illumination at $405nm$, representing an advance for this type of microscopy [21]. Differences between the operating theory of reflection as compared to fluorescence correlation microscopes are reviewed, before summarising the equipment used in this prototype. A method for synchronising camera acquisition to the rotation of the aperture mask was created, allowing widefield and structured illumination frames to be captured rapidly through the same disk. By investigating a mirror sample, the axial resolution of the microscope was tested and found to match well to theory. Finally, image stacks of a PV cell and transistor are presented as an illustration of the application of this system. This microscope is currently being produced commercially and will be announced soon.

Finally, chapter 6 introduces a novel super-resolving fluorescence aperture correlation microscope, invented after considering how to improve aperture mask patterns through tailored spatial frequency content. By using coherent illumination and tailored aperture mask patterns, we present theory which suggests lateral resolution enhancement of a factor of 2 is possible in this configuration, particularly when using a disk mask with an arrangement of spatial frequencies with 6-fold rotational symmetry. Through the masking of

the zeroth diffractive order from the disk, the signal at high lateral spatial frequency is shown to be enhanced relative to lower spatial frequencies; this results in an enhanced image filling the confocal region of support better than confocal microscopy, while retaining the advantages of a wide-field real-time microscope. The microscope is constructed and preliminary testing shows a resolution enhancement of 1.5 over conventional microscopy, despite issues with registration calibration and alignment.

FUTURE WORK This body of work suggests several future avenues for further development of this microscopy technique, which we review here. Firstly, the current super-resolving microscope could be improved significantly by identifying the source of the registration calibration issues present in the system and fixing these. Being able to register images accurately over a larger area would permit not only a wider field of view but also the ability to more precisely investigate the optical transfer function of the system, by fourier transforming an area containing not just a few beads but several tens of beads. Also, replacing the laser with a less noisy variant would yield images with more consistent illumination power. This should result in the ability to take image stacks of biological samples showcasing noticeably improved resolution and signal versus widefield or even confocal microscopy.

Extensions to the current system could include incorporating vacuum deposited masks for removal of the zeroth diffracted order from the spinning disk. This would permit, through the manufacture of several different masks with different transmissivity, a full experimental investigation into the effect of removing this zeroth order, eventually targeting the predicted optimal characteristics from our models.

The effect of polarisation on the contrast of the illumination pattern and thus performance of the microscope, particularly at high NA, would also prove useful with regards to optimising the performance of the microscope. It has been shown that for particular orientations of structured illumination,

one can calculate the optimal linear polarisation direction - rather than using circular polarisation as is often done. This could point towards improvements such as a spinning polariser matched to the rotation of the spinning disk, ensuring optimal polarisation of the first diffracted orders throughout disk rotation.

Finally, using partially coherent illumination could be another way of tailoring the performance of the microscope, making it less susceptible to dust on optical elements as well as potentially improving its axial sectionining characteristics by reducing the axial extent of the illumination pattern.

Ultimately, perhaps the most promising avenue for future development would be the design and construction of a binary phase mask based approach to super resolving aperture correlation microscopy. By optimising for phase rather than amplitude, the current code used to generate binary amplitude masks can be used to generate these as well. With this type of mask, the amount of light put into the zeroth order can be tailored to a greater extent, allowing for more power to be put into higher order modes. As such, a phase mask approach would further improve the light budget of the system, at the cost of no longer being able to collect light reflected from the disk. Instead, return fluorescence passing through the disk would be separated into two identical imaging paths, with a separate phase mask placed at each imaging pupil. These secondary phase masks would then be able to separate widefield information from super-resolving information, allowing a subtraction process to then recover a final image, as before. Preliminary modelling suggests that such a system could exhibit better resolution through the enhancement of illumination pattern contrast and signal.

To conclude, this thesis has furthered the development of high-speed microscopy through the construction of 2 aperture correlation microscopes and associated image processing algorithms. These designs, coupled with investigations into the use of novel aperture mask patterns led to the invention of a new super-resolving microscope with potentially very useful characteristics.

With some improvements to the system, this approach could become a viable commercial microscope with several applications in biological research.

Part I

APPENDIX

A

OPTICAL TRANSFER FUNCTION MODELLING

A couple of different implementations of the OTF were attempted in building the new Matlab code. Stokseth's approximation to the OTF assumes a low NA and aberration-free optics, and is a computationally cheap way of calculating the OTF with defocus. It is typically assumed that the defocus in Stokseth's approximation can be given as the normalised axial coordinate u. However, the original paper specifies that the defocus coordinate is actually the optical path length of the focusing beam, which is related to the defocus z by[35]:

$$w = -r - z\cos\alpha + (r^2 + 2rz + z^2\cos^2\alpha)^{\frac{1}{2}} \tag{43}$$

Where r is the front focal distance of the microscope, and α is the angle from the focal plane to the edge of the principal plane (ie. $\alpha = \arcsin(NA/n)$). Although r is not often given by microscope objective manufacturers, it can be determined if the tube lens focal distance is known, since the magnification of the microscope $M = \frac{r_{tube}}{r}$. Generally, in the case of Olympus microscopes, the tube lens focal length is 180mm.

This was the first approximation removed by the new code - it has very little computational cost, as it is simply a rescaling of the defocus. It also encapsulates an important concept - although it is often assumed, the OTF is not identical at positive or negative defocus (although this effect is only truly apparent at very high NA).

Finally, a full simulation of the diffraction OTF was also performed, summing several terms in the full equation[35, 34]:

$$T = \frac{4}{\pi a}\cos\left(\frac{1}{2}as\right) * \left\{\beta J_1(a) + \sum_{n=1}^{\infty}(-1)^{n+1}\frac{\sin 2n\beta}{2n}\left[J_{2n-1}(a) - J_{2n+1}(a)\right]\right\} \tag{44}$$

$$-\frac{4}{\pi a}\sin\left(\frac{1}{2}as\right)\sum_{n=0}^{\infty}(-1)^{n+1}\frac{\sin(2n+1)\beta}{2n+1} * \left[J_{2n}(a) - J_{2(n+1)}(a)\right] \tag{45}$$

With:

$$a = \frac{4\pi}{\lambda}ws \tag{46}$$

$$\beta = \arccos(s/2) \tag{47}$$

This is, however, extremely computationally intensive - in order to get a decent match to Stokseth's approximation, many terms need to be used and axial response curves begin to take several minutes to compute.

Figure 70 shows a plot of the OTF at 0, small and large defocus values for both Stokseth's approximation and the exact expression. The biggest difference between the 2 can be seen at the small defocus value of $1\mu m$, on the order of the wavelength of the light, especially around the normalised frequency of 1. At focus or at large defocus ($10\mu m$), the difference between these is quite small.

Finally, testing showed that the effect on the final response curves is not very pronounced. The recommended procedure is therefore to use Stokseth's equation generally, switching the exact expression when final graphs are to be calculated.

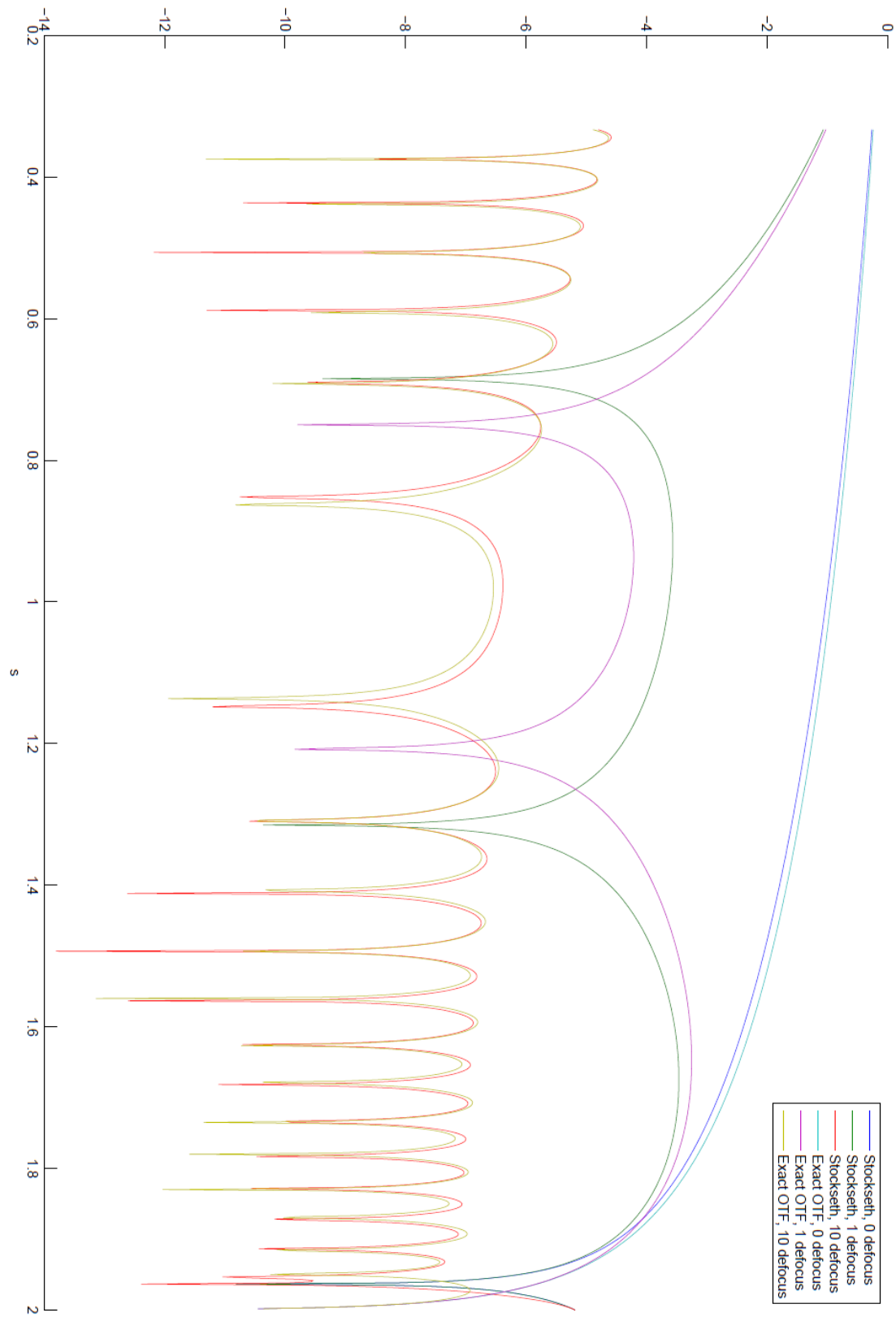


Figure 70: The OTF plotted using both the Stokseth approximation and the exact OTF.

B

COPYRIGHT PERMISSIONS

Appendix: summary of permission for third party copyright works

Please read the e-theses advice and guidance web pages, especially the section on clearing third party copyright works and complete the table below for all third party copyright works not covered by the fair dealing exception of criticism and review.

Where you have ticked:

- Permission to reuse - make sure you include proof of permission in this appendix
- Permission requested - make sure you include a copy of the request letter or email
- Orphan work - you include evidence that you have tried to locate the author

Page Number	Type of work: text, figure, map, etc.	Source work	Copyright holder & year	Work out of copyright	Permission to re-use	Permission requested	permission refused	Orphan work
Page 27	figure	Gustafsson et. al. "Three-dimensional resolution doubling in wide-field fluorescence microscopy by structured illumination	Elsevier 2007		✓			
Page 30	Figure	Rego et al. "Nonlinear structured-illumination microscopy with a photoswitchable protein reveals cellular structures at 50nm resolution"	PNAS 2011		✓			
Page 28	2 Images	http://www.zeiss.co.uk/microscopy/en_gb/products/confocal-microscopes/lsm-880.html	Zeiss			✓		

B.0.1 *Email sent to Zeiss*

To whom it may concern,

I am completing my PhD thesis at Imperial College London entitled 'Aperture Correlation Microscopy'.

I seek your permission to reprint, in my thesis two images from your website:

http://www.zeiss.co.uk/content/microscopy/great-britain/website/en_gb/desktop/products/microscopes/lsm-880/jcr%3acontent/mainpar/inpagetabs/tab-13407858017/corpimageml_42bf/image/lsm880-confocal-drosophila-retina-672.jpg

http://www.zeiss.co.uk/content/microscopy/great-britain/website/en_gb/desktop/products/microscopes/lsm-880/jcr%3acontent/mainpar/inpagetabs/tab-13407858017/corpimageml_3f19/image/lsm880-drosophila-retina-672.jpg

I would like to include the extract in the printed examination copy of my thesis and also the electronic version which will be added to Spiral, Imperial's online repository http://spiral.imperial.ac.uk/ and made available to the public under a Creative Commons Attribution-NonCommercial-NoDerivs licence.

If you are happy to grant me all the permissions requested, please let me know at your earliest convenience

Yours sincerely,

Lionel Fafchamps

B.0.2 *Email received from PNAS*

Hello,

Permission is granted for your use of Figure 6 as described in your message. Please cite the PNAS article in full when re-using the material. Because this material published after 2008, a copyright note is not needed. Let us know if you have any questions.

Best regards,

Elizabeth Griffith for Diane Sullenberger

Executive Editor PNAS

B.0.3 *Elsevier RightsLink Confirmation*

This is a License Agreement between Lionel Fafchamps ("You") and Elsevier ("Elsevier") provided by Copyright Clearance Center ("CCC"). The license consists of your order details, the terms and conditions provided by Elsevier, and the payment terms and conditions. All payments must be made in full to CCC. For payment instructions, please see information listed at the bottom of this form.

Supplier

Elsevier Limited The Boulevard,Langford Lane Kidlington,Oxford,OX5 1GB,UK

Registered Company Number

1982084

Customer name

Lionel Fafchamps

Customer address

62 Brook Road

Ilford, IG2 7EY

License number

3539330537095

License date

Dec 31, 2014

Licensed content publisher

Elsevier

Licensed content publication

Biophysical Journal

Licensed content title

Three-Dimensional Resolution Doubling in Wide-Field Fluorescence Microscopy by Structured Illumination

Licensed content author

Mats G.L. Gustafsson,Lin Shao,Peter M. Carlton,C. J. Rachel Wang,Inna N. Golubovskaya,W. Zacheus Cande,David A. Agard,John W. Sedat

Licensed content date

15 June 2008

Licensed content volume number

94

Licensed content issue number

12

Number of pages

14

Start Page

4957

End Page

4970

Type of Use

reuse in a thesis/dissertation

Portion

figures/tables/illustrations

Number of figures/tables/illustrations

1

Format

both print and electronic

Are you the author of this Elsevier article?

No

Will you be translating?

No

Original figure numbers

figure 6

Title of your thesis/dissertation

Aperture Correlation Microscopy

Expected completion date

Mar 2015

Estimated size (number of pages)

160

BIBLIOGRAPHY

[1] 2002. George W. Bush, at the dedication of his portrait, Austin, Texas. (Cited on page xi.)

[2] URL http://commons.wikimedia.org/wiki/File:Lsfm_methods.svg. Online; Accessed December 2014. (Cited on pages xvii and 22.)

[3] M. G. L. Gustafsson, L. Shao, P. M. Carlton, R. C. J. Wang, I. N. Golubovskaya, W. Z. Cande, D. A. Agard, and J. W. Sedat. Three-dimensional resolution doubling in wide-field fluorescence microscopy by structured illumination. *Biophysical Journal*, 94:4957–4970, 2007. (Cited on pages xviii and 29.)

[4] URL http://www.zeiss.co.uk/microscopy/en_gb/products/confocal-microscopes/lsm-880.html. Online; Accessed December 2014. (Cited on pages xviii and 30.)

[5] E. H. Rego, L. Shao, J. J. Macklin, L. Winoto, G. A. Johansson, N. Kamps-Hughes, M. W. Davidson, and M. G. L. Gustafsson. Nonlinear structured-illumination microscopy with a photoswitchable protein reveals cellular structures at 50-nm resolution. *Proc. Natl. Acad. Sci. USA*, 109:135–143, 2011. (Cited on pages xviii, 32, and 33.)

[6] URL http://commons.wikimedia.org/wiki/File:2color-STED-example.png. Online; Accessed December 2014. (Cited on pages xviii and 34.)

[7] T. Wilson. Confocal microscopy. *Academic Press, San Diego*, 1990. (Cited on pages 1 and 13.)

[8] H. Siedentopf and R. Zsigmondy. Uber sichtbarmachung und größenbestimmung ultramikoskopischer teilchen, mit besonderer anwendung auf goldrubingläser. *Annalen der Physik*, 315:1–39, 1902. (Cited on pages 1 and 22.)

[9] M. Minsky. Microscopy apparatus, December 19 1961. US Patent 3,013,467. (Cited on page 2.)

[10] J.B. Pawley. *Handbook of biological confocal microscopy*. Springer Verlag, 2006. (Cited on page 2.)

[11] Paul Davidovits and M. David Egger. Scanning laser microscope. *Nature*, 223:831, 1969. (Cited on page 2.)

[12] P. Davidovits and M. D. Egger. Scanning laser microscope for biological investigations. *Applied Optics*, 10:1615–1619, 1971. (Cited on page 2.)

[13] M. Petráň, M. Hadravský, M.D. Egger, and R. Galambos. Tandem-scanning reflected-light microscope. *JOSA*, 58(5):661–664, 1968. (Cited on pages 2 and 17.)

[14] D.M. Maurice. A scanning slit optical microscope. *Investigative Ophthalmology & Visual Science*, 13(12):1033, 1974. (Cited on page 2.)

[15] T. Wilson and SJ Hewlett. Imaging in scanning microscopes with slit-shaped detectors. *Journal of microscopy*, 160(Pt 2):115, 1990. (Cited on page 2.)

[16] J. Huisken, J. Swoger, F. Del Bene, J. Wittbrodt, and E.H.K. Stelzer. Optical sectioning deep inside live embryos by selective plane illumination microscopy. *Science*, 305(5686):1007, 2004. (Cited on pages 2 and 23.)

[17] F. Helmchen and W. Denk. Deep tissue two-photon microscopy. *Nature methods*, 2(12):932–940, 2005. (Cited on pages 2 and 19.)

[18] MAA Neil, R. Juskaitis, and T. Wilson. Method of obtaining optical sectioning by using structured light in a conventional microscope. *Optics Letters*, 22(24):1905–1907, 1997. ISSN 1539-4794. (Cited on pages 3, 24, and 25.)

[19] V. Poher, HX Zhang, GT Kennedy, C. Griffin, S. Oddos, E. Gu, DS Elson, M. Girkin, PMW French, MD Dawson, et al. Optical sectioning microscopes with no moving parts using a micro-stripe array light emitting diode. *Optics Express*, 15(18):11196–11206, 2007. (Cited on pages 3 and 25.)

[20] MAA Neil, T. Wilson, and R. Juskaitis. A light efficient optically sectioning microscope. *Journal of Microscopy*, 189(2):114–117, 1998. ISSN 0022-2720. (Cited on pages 3, 26, 39, and 135.)

[21] R. Juskaitis, T. Wilson, MAA Neil, and M. Kozubek. Efficient real-time confocal microscopy with white light sources. *Nature*, 383(6603):804–805, 1996. ISSN 0028-0836. (Cited on pages 3, 17, 26, 39, 80, 96, and 136.)

[22] J. R. Lakowicz. *Principles of Fluorescence Spectroscopy*. Springer, 3rd edition, 2006. (Cited on page 7.)

[23] G. G. Stokes. On the change of refrangibility of light. *Philosophical transaction of the Royal Society of London*, 463(142), 1852. (Cited on page 7.)

[24] N. J. Turro. *Modern Molecular Photochemistry*. University Science Books, 1991. (Cited on page 8.)

[25] F. Jahnig. Structural order of llipid and proteins in membranes: evaluation of fluorescence anisotropy data. *Proc. Natl. Acad. Sci. USA*, 76: 6361–6365, 1979. (Cited on page 9.)

[26] D. Axelrod. Carbocyanine dye orientation in red cell membrane studied by microscopic fluorescence polarization. *Biophys. J.*, 76:557–573, 1979. (Cited on page 9.)

[27] S. J. Strickler and R. A. Berg. Relationship between absorption intensity and fluorescence lifetime of molecules. *J. Chem. Phys.*, 37:814–822, 1962. (Cited on page 9.)

[28] K. Dowling, M. Dayel, M. Lever, P. French, J. Hares, and A. K. L. Dymoke-Bradshow. Fluorescence lifetime imaging with picosecond resolution for biomedical applications. *Optics Letters*, 23:810–812, 1998. (Cited on page 9.)

[29] R. Sanders, A. Draaijer, H. C. Gerritsen, P. M. Houpt, and Y. K. Levine. Quantitative ph imaging in cells using confocal fluorescence lifetime imaging microscopy. *Analytical Biochemistry*, 227:302–308, 1995. (Cited on page 9.)

[30] P. Dedecker, F. C. DeSchryver, and J. Hofkens. Fluorescent proteins: Shine on, you crazy diamond. *J Am. Chem. Soc.*, 135:2387–2402, 2013. (Cited on page 9.)

[31] J. Siegel, K. Suhling, S. Leveque-Fort, S. Webb, D. Davis, D. Phillips, Y. Sabharwal, and P. French. Wide-field time-resolved fluorescence anisotropy imaging (tr-faim): Imaging the rotational mobility of a fluorophore. *Review of Scientific Instruments*, 74:182–192, 2003. (Cited on page 9.)

[32] J. R. Lakowicz, H. Szmacinski, K. Nowaczyk, and M. L. Johnson. Fluorescence lifetime imaging of free and protein-bound nadh. *Proc Natl Acad Sci USA*, 89:1271–1275, 1992. (Cited on page 9.)

[33] A. Thompson. In vivo measurements of diffuse reflectance and time-resolved autofluorescence emission spectra of basal cell carcinomas. *Journal of Biophotonics*, 5, 2012. (Cited on page 9.)

[34] H. H. Hopkins. The frequency response of a defocused optical system. *Proc. R. Soc.*, 231:91–103, 1955. (Cited on pages 10 and 143.)

[35] P.A. Stockseth. Properties of a defocused optical system. *JOSA*, 59(10): 1314–1321, 1969. (Cited on pages 10, 44, and 143.)

[36] CJR Sheppard and M. Gu. Approximation to the three-dimensional optical transfer function. *JOSA A*, 8(4):692–694, 1991. (Cited on page 12.)

[37] Jerome Mertz. *Introduction to Optical Microscopy*. Roberts and Company, 2010. (Cited on pages 14 and 15.)

[38] C. J. R. Sheppard and X. Q. Mao. Confocal microscopes with slit apertures. *J. Mod. Opt.*, 35:1169–1185, 1988. (Cited on page 16.)

[39] S. Kimura and C. Munakata. Three-dimensional optical transfer function for the fluorescent scanning optical microscope with a slit. *Appl. Opt.*, 29:1004–1007, 1990. (Cited on page 16.)

[40] D. R. Sandison and W. W. Webb. Background rejection and signal-to-noise optimisation in the confocal and alternative fluorescence microscopes. *Appl. Opt.*, 33:603, 1994. (Cited on page 16.)

[41] K. B. Im, S. Han, H. Park, D. Kim, and B. M. Kim. Simple high-speed confocal line-scanning microscope. *Optics Express*, 13:5151–5156, 2005. (Cited on page 16.)

[42] R. Wolleschensky, B. Zimmermann, and M. Kempe. High-speed confocal fluorescence imaging with a novel line scanning microscope. *Journal of Biomedical Optics*, 11:064011–064014, 2006. (Cited on page 16.)

[43] V. Poher, G. Kennedy, H. B. Manning, D. M. Owen, H. X. Zhang, E. Gu, M. Dawson, P. French, and M. A. A. Neil. Improved sectioning in a slit scanning confocal microscope. *Optics Letters*, 33:1813–1815, 2008. (Cited on page 17.)

[44] URL http://www.yokogawa.com/scanner/product/csu/csuw1_1_e.htm. Online; Accessed December 2014. (Cited on page 17.)

[45] S. J. Hewlett, D. T. Fewer, and E. M. McCabe. Influence of source coherence and aperture distribution on the imaging properties in direct-view microscopy. *J. Opt. Soc. Am.*, 14:1066–1075, 1997. (Cited on page 17.)

[46] D. T. Fewer, S. J. Hewlett, E. M. McCabe, and J. Hegarty. Direct-view microscopy: Experimental investigation of the dependence of the optical sectioning characteristics on pinhole-array configuration. *J Microsc*, 187:54–61, 1997. (Cited on page 17.)

[47] W. W. Webb W. Denk, D. Strickler. Two-photon laser scanning fluorescence microscopy. *Science*, 248, 1990. (Cited on page 18.)

[48] W. Denk. Two-photon excitation in functional biological imaging. *J. Biomed. Opt.*, 1, 1996. (Cited on page 19.)

[49] A. E. Siegman. *Lasers*. University Science Books, 1986. (Cited on page 19.)

[50] P. W. Milonni and J. H. Eberly. *Lasers*. Wiley, 1988. (Cited on page 19.)

[51] S. W. Hell, M.J. Booth, S. Wilms, C. M. Schnetter, A. K. Kirsch, D. Arndt-Jovin, and T.M. Jovin. Two-photon near- and far-field fluorescence microscopy with continuous-wave excitation. *Optics Letters*, 23(15):1238–1240, 1998. (Cited on page 19.)

[52] W. R. Zipfel, R. M. Williams, and W.W. Webb. Nonlinear magic: multiphoton microscopy in the biosciences. *Nat. Biotech.*, 21, 2003. (Cited on page 19.)

[53] K. Svoboda. Principles of two-photon excitation microscopy and its applications to neuroscience. *Neuron*, 50, 2006. (Cited on page 19.)

[54] R. W. Boyd. *Nonlinear Optics*. Academic Press, 2003. (Cited on page 20.)

[55] I. Freund and M. Deutsch. Second harmonic microscopy of biological tissue. *Opt. Lett.*, 11, 1986. (Cited on page 20.)

[56] P. Stoller, P.M. Celliers, K. M. Reiser, and A.M. Rubenchik. Quantitative second harmonic generation microscopy in collagen. *Appl. Opt.*, 42, 2003. (Cited on page 20.)

[57] R. M. Williams, W. R. Zipfel, and W.W. Webb. Interpreting second harmonic generation images of collagen i fibrils. *Biophys. J.*, 88, 2005. (Cited on page 20.)

[58] P. J. Campagnola, W. Mohler, and A. E. Millard. Three-dimensional high resolution second harmonic imaging of endogenous structural proteins in biological tissues. *Biophys. J.*, 81, 2002. (Cited on page 20.)

[59] J. A. Squire, M. Muller, G. J. Brakenhoff, and K. R. Wilson. Third-harmonic generation microscopy. *Opt. Express*, 3, 1998. (Cited on page 21.)

[60] M. Muller and A. Zumbusch. Coherent anti-stokes raman scattering microscopy. *Chem. Phys. Chem.*, 8, 2007. (Cited on page 21.)

[61] M. Muller and J. M. Schins. Imaging the thermodynamics state of lipid membranes with multiplex cars microscopy. *J. Phys. Chem. B*, 106, 2002. (Cited on page 21.)

[62] Philipp J. Keller and Ernst H. K. Stelzer. Lichtscheiben-mikroskopie in der molekularen zellbiophysik. *Laborwelt*, 5:18–21, 2006. (Cited on page 22.)

[63] U. Krzic, S. Gunther, L. Hufnagel, D. von Gegerfelt, H. Karlsson, E. Illy, and J. Hel. Lichtscheiben-fluoreszenzmikroskopie (spim) und laser-anregung in orange zur abbildung lebender organismen. *BioPhotonik*, 1:42–44, 2011. (Cited on page 22.)

[64] A. H. Voie, D. H. Burns, and F. A. Spelman. Orthogonal-plane fluorescence optical sectioning: Three-dimensional imaging of macroscopic

biological specimens. *Journal of Microscopy*, 170:229–236, 1993. (Cited on page 23.)

[65] K. Greger, J. Swoger, and E. H. Stelzer. Basic building units and properties of a fluorescence single plane illumination microscope. *The Review of Scientific Instruments*, 2:78, 2007. (Cited on page 23.)

[66] J. Huisken and Didier Y. R. Stainier. Even fluorescence excitation by multidirectional selective plane illumination microscopy (mspim). *Optics Letters*, 32:2608–10, 2012. (Cited on page 23.)

[67] U. Krzic, S. Gunther, T. E. Saunders, S. J. Streichan, and L. Hufnagel. Multiview light-sheet microscope for rapid in toto imaging. *Nature Methods*, 9:730–733, 2012. (Cited on page 23.)

[68] Raju Tomer, Khaled Khairy, Fernando Amat, and P. J. Keller. Quantitative high-speed imaging of entire developing embryos with simultaneous multiview light-sheet microscopy. *Nature Methods*, 9:755–763, 2012. (Cited on page 23.)

[69] Zeno Lavagnino, Francesca Cella Zanacchi, Emiliano Ronzitti, and Alberto Diasporo. Two-photon excitation selective plane illumination microscopy (2pe-spim) of hihigh scattering samples: Characterization and application. *Optics Express*, 21:5998–6008, 2013. (Cited on page 23.)

[70] P. J. Keller, A. D. Schmidt, and E. H. K. Wittbrodt, J.and Stelzer. Reconstruction of zebrafish early embryonic development by scanned light sheet microscopy. *Science*, 322:1065–1069, 2008. (Cited on page 24.)

[71] Chris Dunsby. Optically sectioned imaging by oblique plane microscopy. *Optics Express*, 16:20306–20316, 2008. (Cited on page 24.)

[72] E.J. Botcherby, R. Juskaitis, M.J. Booth, and T. Wilson. Aberration-free optical refocusing in high numerical aperture microscopy. *Optics letters*, 32(14), 2007. ISSN 1539-4794. (Cited on page 24.)

[73] EJ Botcherby, R. Juskaitis, MJ Booth, and T. Wilson. An optical technique for remote focusing in microscopy. *Optics Communications*, 281(4): 880–887, 2008. ISSN 0030-4018. (Cited on page 24.)

[74] S. Kumar, D. Wilding, M. B. Sikkel, A. R. Lyon, K. T. MacLeod, and C. Dunsby. High-speed 2d and 3d fluorescence microscopy of cardiac myocytes. *Optics Express*, 19:13839–13847, 2011. (Cited on page 24.)

[75] B. Bailey, D. Farkas, D. Taylor, and F. Lanni. Enhancement of axial resolution in fluorescence microscopy by standing-wave excitation. *Nature*, 366:44–48, 1993. (Cited on page 24.)

[76] URL http://zeiss-campus.magnet.fsu.edu/tutorials/opticalsectioning/apotome/indexflash.html. Online; Accessed December 2014. (Cited on page 25.)

[77] Z. Gong, H. Zhang, E. Gu, C. Griffin, M. Dawson, V. Poher, G. Kennedy, P. French, and M. A. A. Neil. Matrix-addressable micropixellated ingan light-emitting diodes with uniform emission and increased light output. *Electron Devices*, 54:2650–2658, 2007. (Cited on page 25.)

[78] Z. Gong, E. Gu, S. R. Jin, D. Massoubre, B. Guilhabert, H. Zhang, M. Dawson, V. Poher, G. Kennedy, P. French, and M. A. A. Neil. Efficient flip-chip ingan micro-pixellated light-emitting diode aarray: promising candidates for micro-displays and colour conversion. *Journal of Physics D*, 41:094002, 2008. (Cited on page 25.)

[79] T. Wilson, R. Juškaitis, MAA Neil, and M. Kozubek. Confocal microscopy by aperture correlation. *Optics letters*, 21(23):1879–1981, 1996. ISSN 1539-4794. (Cited on pages 26, 39, and 135.)

[80] Hanley, Verveer, Gemkow, and Arndt-Jovin. An optical sectioning programmable array microscope implemented with a digital micromirror device. *Journal of Microscopy*, 196:317–331, 1999. (Cited on page 27.)

[81] Q. S. Hanley, P. J. Verveer, and T. Jovin. Optical sectioning fluorescence spectroscopy in a programmable array microscope. *Applied Spectroscopy*, 52:783–789, 1998. (Cited on page 27.)

[82] R. Heintzmann, Q. S. Hanley, D. Arndt-Jovin, and T. Jovin. A dual path programmable array microscope (pam): simultaneous acquisition of confjugate and non-conjugate images. *Journal of Microscopy*, 204:119–135, 2001. (Cited on pages 27 and 39.)

[83] Q. S. Hanley, K. A. Lidke, R. Heintzmann, D. Arndt-Jovin, and T. Jovin. Fluorescence lifetime imaging in an optically sectioning programmable array microscope. *Cytometry Part A*, 67A:112–118, 2005. (Cited on page 27.)

[84] MAA Neil, R. Jukaitis, and T. Wilson. Real time 3d fluorescence microscopy by two beam interference illumination. *Optics communications*, 153(1-3):1–4, 1998. (Cited on page 27.)

[85] MAA Neil, A. Squire, R. Jusikaitis, PIH Bastiaens, and T. Wilson. Wide-field optically sectioning fluorescence microscopy with laser illumination. *Journal of Microscopy*, 197(Pt 1):1ą4, 2000. (Cited on page 27.)

[86] M. G. L. Gustafsson. Surpassing the lateral resolution limit by a factor of two using structured illumination microscopy. *Journal of Microscopy*, 198:82–87, 2000. (Cited on pages 28 and 99.)

[87] URL http://api.gehealthcare.com/api/deltavision-omx.asp. Online; Accessed December 2014. (Cited on page 28.)

[88] M. Beck, M. Aschwanden, and A. Stemmer. Sub-100-nanometre resolution in total internal reflection fluorescence microscopy. *Journal of Microscopy*, 232:99–105, 2008. (Cited on page 28.)

[89] C. Sheppard. Super-resolution in confocal imaging. *Optik*, 80:53, 1988. (Cited on page 29.)

[90] C. B. Muller and J. Enderlein. Image scanning microscopy. *Phys. Rev. Lett.*, 104:198101, 2010. (Cited on pages 30 and 99.)

[91] C. Sheppard, S. B. Mehta, and R. Heintzmann. Superresolution by image scanning microscopy using pixel reassignment. *Optics Letters*, 38: 2889–2892, 2013. (Cited on page 30.)

[92] A. G. York, S. H. Parekh, D. D. Nogare, R. S. Fischer, K. Temprine, M. Mione, A. B. Chitnis, C. A. Combs, and H. Shroff. Resolution doubling in live multicellular organisms via multifocal structured illumination microscopy. *Nature Methods*, 9:749, 2012. (Cited on page 31.)

[93] A. G. York, P. Chandris, D. D. Nogare, J. Head, P. Wawrzusin, R. S. Fischer, A. B. Chitnis, and H. Shroff. Instant super-resolution imaging in live cells and embryos via analog image processing. *Nature Methods*, 10:1122, 2013. (Cited on pages 31 and 99.)

[94] R. Heintzmann, T. Jovin, and C. Cremer. Saturated patterned excitation microscopy - a concept for optical resolution improvement. *J. Opt. Soc. Am. A*, 19:1599–1609, 2002. (Cited on page 32.)

[95] M. G. L. Gustafsson. Nonlinear structured illumination microscopy: Wide-field fluorescence imaging with theoretically unlimited resolution. *Proc. Natl. Acad. Sci. USA*, 102:4957–4970, 2005. (Cited on page 33.)

[96] S. W. Hell and J. Wichmann. Breaking the diffraction resolution limit by stimulated emission: stimulated emission depletion fluorescence microscopy. *Opt. Lett.*, 19:780–782, 1994. (Cited on page 34.)

[97] S. W. Hell. Toward fluorescence nanoscopy. *Nat. Biotech.*, 21:1347–1355, 2003. (Cited on page 35.)

[98] M. Dyba and S. W. Hell. Focal spots of size 1/23 open up far-field fluorescence microscopy at 33nm axial resolution. *Phys. Rev. Lett.*, 88: 163901, 2002. (Cited on page 35.)

[99] K. Willig, Kellner. R. R., R. Medda, B. Hein, S. Jakobs, and S. W. Hell. Nanoscale resolution in gfp-based microscopy. *Nature Methods*, 3:721–723, 2006. (Cited on page 35.)

[100] B. Hein, K. Willig, and S. W. Hell. Stimulated emission depletion (sted) nanoscopy of a fluorescent protein-labeled organelle inside a living cell. *Proc. Natl. Acad. Sci. USA*, 105:14271–14276, 2008. (Cited on page 35.)

[101] Jürgen Kleine-Vehn, Krzysztof Wabnik, Alexandre Martinière, Łukasz Łangowski, Katrin Willig, Satoshi Naramoto, Johannes Leitner, Hirokazu Tanaka, Stefan Jakobs, Stéphanie Robert, Christian Luschnig, Willy Govaerts, Stefan W Hell, John Runions, and Jiří Friml. Recycling, clustering, and endocytosis jointly maintain pin auxin carrier polarity at the plasma membrane. *Molecular Systems Biology*, 7(1), 2011. ISSN 1744-4292. doi: 10.1038/msb.2011.72. (Cited on page 35.)

[102] A. Chmyrov, J. Keller, T. Grotjohann, M. Ratz, E. d'Este, S. Jakobs, C. Eggeling, and S. W. Hell. Nanoscopy with more than 100,000 'doughnuts'. *Nature Methods*, 10:737–740, 2013. (Cited on page 35.)

[103] E. Betzig, G. H. Patterson, R. Sougrat, O. W. Lindwasser, S. Olenych, J. S. Bonifacino, M. W. Davidson, and J. Lippincott-Schwartz. Imaging intracellular fluorescent proteins at nanometer resolution. *Science*, 313:1642–1645, 2006. (Cited on page 36.)

[104] S. T. Hess, T. P. Girirajan, and M. D. Mason. Ultra-high resolution imaging by photoactivation localization microscopy. *Biophys. J.*, 91:4258–4272, 2006. (Cited on page 36.)

[105] J. M. Rust, M. Bates, and X. Zhuang. Subdiffraction limit imaging by stochastic optical reconstruction microscopy (storm). *Nature Methods*, 3:793–795, 2006. (Cited on page 36.)

[106] Mantas Zarauskas. Prototype optical system for aperture correlation microscopy device. Master's thesis, Imperial College London, 2010. (Cited on pages 49 and 86.)

[107] M. Aguilar, E. Barrera, M. Palomar-Pardave, L. Huerta, and S. Muhl. Characterization of black and white chromium electrodeposition films: surface and optical properties. *Journal of Non-Crystalline Solids*, 329:31–38, 2003. (Cited on pages 52 and 90.)

[108] *Characterization of black chrome films prepared by electroplating technique*, May 2011. World Renewable Energy Congress. (Cited on pages 52 and 90.)

[109] URL http://www.carolina.com/. Online; Accessed December 2014. (Cited on page 53.)

[110] URL http://www.qt.io/. Online; Accessed March 2015. (Cited on page 53.)

[111] M. Sonka and J. M. Fitzpatrick. *Handbook of medical imaging (Volume 2, Medical image processing and analysis)*. SPIE, 2000. (Cited on page 64.)

[112] Noppadol Chumchob and Ke Chen. A robust affine image registration method. *International Journal of Numerical Analysis and Modeling*, 6(2): 311–334, 2009. (Cited on page 64.)

[113] George Wolberg and Siavash Zokai. Image registration for perspective deformation recovery. *Proc. SPIE, Automatic Target Recognition X*, 2000. (Cited on page 64.)

[114] B.S. Reddy and B.N. Chatterji. An fft-based technique for translation, rotation, and scale-invariant image registration. *IEEE Transactions on Image Processing*, 5:1266–1271, 1996. (Cited on page 65.)

[115] B. Zitova and J. Flusser. Image registration methods: a survey. *Image and Vision Computing*, 21:977–1000, 2003. (Cited on page 66.)

[116] E.H.W. Meijering, K.J. Zuiderveld, and M.A. Viergever. Image reconstruction by convolution with symmetrical piecewise nth-order polynomial kernels. *IEEE Transactions of Image Processing*, 8:192–201, 1999. (Cited on page 66.)

[117] T.M. Lehmann, C. Gonner, and K. Spitzer. Survey: interpolation method in medical image processing. *IEEE Transactions on Medical Imaging*, 18: 1049–1075, 1999. (Cited on page 66.)

[118] T. Thevenaz, T. Blu, and M. Unser. Interpolation revisited. *IEEE Transactions on Medical Imaging*, 19:739–758, 2000. (Cited on page 66.)

[119] URL `http://www.acktar.com/category/FractalBlack`. Online; Accessed December 2014. (Cited on page 92.)

[120] W. L. Bailey, M. G. Coleman, C. B. Harris, and I.A. Lesk. Texture etching of silicon: method, 1979. US Patent 4137123. (Cited on page 92.)

[121] V. E. Jr. Hauser and A.K. Sinha. Reacting silane and ammonia, 1979. Us Patent 4142004. (Cited on page 93.)

[122] Shinichi Hayashi. Sample observation device for generating super resolution image, 2014. European Patent 2437095, Applicant: Olympus Medical System Corporation. (Cited on page 99.)

[123] CJR Sheppard and A Choudhury. Annular pupils, radial polarization, and superresolution. *Applied Optics*, 43:4322–4327, 2004. (Cited on page 110.)

[124] A. P. Konijnenberg, L. Wei, N. Kumar, L. Couto Correa Pinto Filho, L. Cisotto, S. F. Pereira, and H. P. Urbach. Demonstration of an optimised focal field with long focal depth and high transmission obtained with the extended nijboer-zernike theory. *Optics Express*, 22:311–324, 2014. (Cited on page 110.)

[125] M. Gu. *Principles of Three-dimensional imaging in confocal microscopes*. World Scientific, 1996. (Cited on page 113.)

[126] C. W. Smith, E. J. Botcherby, and T. Wilson. Resolution of oblique-plane images in sectioning microscopy. *Optics Express*, 19(3):2662, 2011. (Cited on page 113.)